AD-A230 701

University of Pensylvania
Philadelphia, PA 19104-6390

DTIC FILE COPY

SMART SENSING AND RECOGNITION BASED
ON MODELS OF NEURAL NETWORKS

Final Report

Prepared for:
The U.S. Army Research Office
P.O. Box 12211
Research Triangle Park, N.C. 27709-2711

by

N.H. Farhat
Principal Investigator

Under ARO Grant No:
DAAL03-87-K-0108

November 1990

DTIC
ELECTE
JAN 15 1991
S
B
D

Report No. EO-MO 90-1

REPORT DOCUMENTATION PAGE

1a. REPORT SECURITY CLASSIFICATION	1b. RESTRICTIVE MARKINGS
Unclassified	

2a. SECURITY CLASSIFICATION AUTHORITY	3. DISTRIBUTION / AVAILABILITY OF REPORT
2b. DECLASSIFICATION / DOWNGRADING SCHEDULE	Approved for public release; distribution unlimited.

4. PERFORMING ORGANIZATION REPORT NUMBER(S)	5. MONITORING ORGANIZATION REPORT NUMBER(S)
	ARO 24898.9-EL

6a. NAME OF PERFORMING ORGANIZATION	6b. OFFICE SYMBOL (If applicable)	7a. NAME OF MONITORING ORGANIZATION
University of Pennsylvania		U. S. Army Research Office

6c. ADDRESS (City, State, and ZIP Code)	7b. ADDRESS (City, State, and ZIP Code)
Philadelphia, PA 19104-6390	P. O. Box 12211 Research Triangle Park, NC 27709-2211

8a. NAME OF FUNDING / SPONSORING ORGANIZATION	8b. OFFICE SYMBOL (If applicable)	9. PROCUREMENT INSTRUMENT IDENTIFICATION NUMBER
U. S. Army Research Office		DAAL03-87-K-0108

8c. ADDRESS (City, State, and ZIP Code)	10. SOURCE OF FUNDING NUMBERS			
	PROGRAM ELEMENT NO	PROJECT NO.	TASK NO.	WORK UNIT ACCESSION NO
P. O. Box 12211 Research Triangle Park, NC 27709-2211				

11. TITLE (Include Security Classification)

SMART SENSING AND RECOGNITION BASED ON MODELS OF NEURAL NETWORKS

12. PERSONAL AUTHOR(S) Nabil H. Farhat, Principal Investigator

13a. TYPE OF REPORT	13b. TIME COVERED	14. DATE OF REPORT (Year, Month, Day)	15. PAGE COUNT
FINAL	FROM 09/17/87 TO 09/16/90	1990, November, 15	121

16. SUPPLEMENTARY NOTATION The view, opinions and/or findings contained in this report are those of the author(s) and should not be construed as an official Department of the Army position, policy, or decision, unless so designated by other documentation.

17. COSATI CODES			18. SUBJECT TERMS (Continue on reverse if necessary and identify by block number)
FIELD	GROUP	SUB-GROUP	Automated target recognition, neural networks, photonic implementations, nonlinear dynamical signal processing

19. ABSTRACT (Continue on reverse if necessary and identify by block number)

Radar target identification is an important problem to which much attention has been given in the past solution efforts relied predominately on linear signal processing techniques. There are two traditional approaches. In the one, high resolution images are formed to be examined and identified by human observers. In the second, target signatures (feature vectors) are formed for automated machine identification. The first approach is usually quite costly and has several practical limitations stemming from the high cost and large size of microwave imaging apertures. The second approach is yet to provide a reliable recognition scheme.

20. DISTRIBUTION / AVAILABILITY OF ABSTRACT	21. ABSTRACT SECURITY CLASSIFICATION
☐ UNCLASSIFIED/UNLIMITED ☐ SAME AS RPT ☐ DTIC USERS	Unclassified

22a. NAME OF RESPONSIBLE INDIVIDUAL	22b. TELEPHONE (Include Area Code)	22c. OFFICE SYMBOL

DD FORM 1473, 84 MAR   83 APR edition may be used until exhausted   SECURITY CLASSIFICATION OF THIS PAGE
All other editions are obsolete

UNCLASSIFIED

Motivated by the observation that the above approaches are primarily linear and that biological systems, which process information in a highly nonlinear, collective, and frequently iterative manner, are very adept at carrying out recognition, classification, association , and optimization tasks, we elected to investigate the capabilities of collective nonlinear processing in target identification. This report describes our research findings in this area. Our approach was also influenced by the observation that biological pattern recognition systems, e.g. in the cortex, did not develop in isolation but in synergism with sensory organs and their feature forming networks. This means that development of artificial pattern and target recognition systems may benefit from considering the data acquisition, representation, identification, and cognition aspects of the. problem simultaneously. This unified approach to the problem of neuromorphic automated target ιcognition (ATR), has produced, as described in this report the following findings: (a) The differential range-profile of an isolated target (e.g. aerospace targets) provides an excellent feature vector for use with adaptive learning networks, (b) Near perfect and robust classification of test targets is demonstrated in a multilayer error backpropagation networks using realistic range-profile data generated in our anechoic chamber microwave scattering measurement facility, (c) Despite this excellent performance, such networks lack cognitive ability. This means when the network is presented with a feature vector that does not belong to any one of the targets used in training it, it can classify it as one of the targets it learned. The network has no inherent ability to tell, on its own (i.e. without the help of auxilliary gear acting as novelty detector) that the test feature vector belongs to a novel target. Lack of cognition is a serious limitation of networks meant to operate in complex uncontrolled environment. (d) Most neural networks for pattern recognition being dealt with today lack cognitive ability. Preliminary findings of our research motivate us to make the following hypothesis in this regard: **To be cognitive, a neural network must be nonlinear and dynamical and able to manifest bifurcation.** This means it should be able to carry out computations with more than one type of attractor in its phase-space and to be able to switch between them depending on whether the sensory input is familiar or novel. Our future research will be aimed at validating this hypothesis. Demonstrating its practicality in an engineering sense can have far reaching implications. For example, it could enable a combat aircraft, not only detect with its radar another at 200 nautical miles, as is common today, but also to identify it cognitively without having to form an image.

Accession For

NTIS GRA&I	☑
DTIC TAB	☐
Unannounced	☐
Justification	

By

Distribution/

Availability Codes

Dist | Avail and/or Special

A-1

REPORT OF INVENTIONS AND SUBCONTRACTS
(Pursuant to "Patent Rights" Contract Clause) (See Instructions on Reverse Side)

1. NAME AND ADDRESS OF CONTRACTOR *(Include Zip Code)*

University of Pennsylvania
Philadelphia, PA 19104-6390

2. CONTRACT NUMBER

DAAL03-87-K-0108 P02

3. TYPE OF REPORT *(Check One)*

☐ a. INTERIM ☑ b. FINAL

SECTION I - INVENTIONS *("Subject Inventions")*

4. INVENTION DATA *(Listed below are all inventions required to be reported) (If "None," so state)*

(i) NAME OF INVENTOR(S)	(ii) TITLE OF INVENTION	(iii) CONTRACTOR DISCLOSURE IDENTIFICATION NUMBER OR PATENT APPLICATION SERIAL NUMBER	(iv) CONTRACTOR ELECTS TO FILE U.S. PATENT APPLICATION		(v) CONFIRMATORY LICENSE OR ASSIGNMENT FORWARDED TO CONTRACTING OFFICER	
			YES	NO	YES	NO
N. Farhat	Super-resolution	UP-143	X			X
N. Farhat	Self-Programming Neural Computer	UPN-78	X			X

SECTION II - SUBCONTRACTS *(Containing a "Patent Rights" Clause)*

5. SUBCONTRACT DATA *(Listed is information required but not previously reported (or Subcontracts) (If "None," so state)*

(i) NAME AND ADDRESS OF SUBCONTRACTOR *(Include Zip Code)*	(ii) SUBCONTRACT NUMBER	(iii) SUBCONTRACT PATENT RIGHTS CLAUSE	(iv) WORK TO BE PERFORMED UNDER SUBCONTRACT	(v) SUBCONTRACT DATES	
				AWARD	COMPLETION

SECTION III - CERTIFICATION

CONTRACTOR CERTIFIES THAT PROMPT IDENTIFICATION AND TIMELY DISCLOSURE OF SUBJECT INVENTIONS PROCEDURES HAVE BEEN FOLLOWED

DATE	NAME AND TITLE OF AUTHORIZED OFFICIAL *(Print or Type)*	SIGNATURE
11/19/90	BERENICE N. SAXON ASSISTANT DIRECTOR	*Berenice Saxon*

The views, opinions, and/or findings contained in this report are those of the author(s) and should not be construed as an official Department of the Army position, policy, or decision, unless so designated by other documentation.

CONTENTS

        I.   Image Interpretation and Prediction in
               Microwave Diversity Imaging

        II.   Range Profiles and Images of a Loaded Straight
               Wire

        III.   A New Iterative Algorithm for Exploration of
               Data Available in Multiple Restricted Regions
               with Application to Radar Imaging

        IV.   Microwave Diversity Imaging and Automated
               Target Identification Based on Models of
               Neural Networks

        V.   Echo Inversion and Target Shape Estimation by
               Neuromorphic Processing

        VI.   Learning Networks for Extrapolation and Radar
               Target Identification

        VII. Phase Space Engineering for Neurodynamic Target
               Identification

        VIII. Optoelectronic Neural Networks and Learning
               Machines

1. STATEMENT OF THE PROBLEM STUDIED

Radar targets and other microwave scattering objects can be identified by either forming images with sufficient resolution to be recognized by the human observer or by forming representations (signatures or feature vectors) of the target and using them in automated machine recognition. Tomographic Microwave diversity imaging techniques that combine angular (aspect), spectral (wavelength), and polarization degrees of freedom can produce images of the 3-D distribution of scattering centers of a target with near optical resolution. Despite this capability there are practical circumstances when the size and/or cost of the physical aperture needed to furnish the required angular degrees of freedom is too high, or when the time delay involved in synthesizing such an aperture through relative motion between the radar system and the object being imaged (as for example, in SAR and ISAR) is not acceptable. One is faced then with the problem of having to identify the target from a limited amount of information that is insufficient to produce an identifiable image.

A number of approaches have been studied and explored in the past to circumvent this problem [1]-[4]. Generally these have met with limited success. They include super-resolution by analytic continuation and singularity expansion methods. The reason for the limited success of these approaches is that they are primarily linear.

Humans, and other animals, recognize objects in their environment with great ease. This is essential for their survival. They do this also with robustness, i.e. even when objects are partially obscured or when the data they convey to sensory organs are corrupted by noise and the signal levels involved vary over very wide dynamic range. Moreover the recognition task is easily achieved even when the object is not isolated but exists in the prsence of clutter (background). These functional capabilities are attributed to the collective nonlinear, nature of signal processing in the central nervous system. Biological neural nets and their models furnish accordingly an intriguing paradigm that is worth emulating in artificial man made systems. Such systems can be of great utility in patern recognition, solution of optimization problems and inverse scattering problems and in associative storage and recall of information (associative memory).

The goal of research described in this report is study of the neural approach to signal processing and assessment of its utility in target recognition and image understanding. In particular robust target recognition from sketchy (partial and/or noisy) information is of primary interest. The approach adopted in our investigation is to study several interrelated facets of the problem. These include: (a) Microwave data acquisition and image understanding, (b) data representation which involves formation of signature vectors or feature vectors that can help achieve robust distortion invariant recognition. By distortion invariance we mean recognizing the target irrespective of aspect, distance, or location within the field of

view (rotation, size, and shift invariance in the pattern recognition literature). By robust we mean recognition from sketchy information over a wide dynamic-range of signal levels and interrogating feature vectors, (c) assess and demonstrate the capabilities of neural computation in the solution of selected inverse scattering problems (image reconstruction and object recognition), (d) study of analog hardware implementation of neural networks and learning machines employing photonic (optoelectronic, electron-optical, electro-optical) technology.

Extensive efforts in data acquisition and microwave image understanding and image reconstruction employing diversity information and range-profile representations (see Appendices I to V) were carried out to evaluate and establish the viability of range-profiles as signature or feature vectors suitable for use not only in microwave image reconstruction, but also as will be seen below, in automated neuromorphic target classification and cognition.

We elected to study neuromorphic radar target recognition of aerospace targets because such targets are isolated and clutter is minimal. This makes the problem less difficult than, for example, object recognition by the visual system in natural scenes where isolating the object from background comprises a complex task apparently carried out by the eye-brain system routinely through a mechanism of attention focusing whose exact details are not fully known. We believe, progress with the aerospace target recognition problem can be helpful in the problem of 3-D object recognition in natural scenes. Another reason for our choice of the radar target recognition of aerospace targets is the ability to generate realistic scattering data and signatures of scale-models of targets of interest in our anechoic chamber microwave scattering facility. The facility provides semi-automated measurement of the frequency response of test objects over any frequency (spectral) window in the (2-26.5)GHz frequency range for any target aspect and any desired state of polarization of the transmitter and the receiver. (See Appendix IV for detail.) The range-profile representation alluded to earlier is the real-part of the Fourier transfrom of the measured frequency response of the target after removal of the range-phase. A target is characterized by either its frequency response (measured frequency response corrected for range-phase due to propagation between the phase center of the transmitting/receiving antenna and the scattering phase-center of the target) for all aspect angles of interest or by the corresponding range-profiles. In our work we refer to the range-profiles variably as echo, signature vector or feature vector. When sufficiently wide spectral windows are used, in data acquisition, the echo or range-profile echo from the target is an approximation of the impulse response of the target produced by impulsive plane wave illumination.

2. SUMMARY OF THE MOST IMPORTANT RESULTS

Our initial efforts in assessing the capabilities of neurocomputing in microwave scatterer identification made use of a fully connected neural network operating as heteroassociative memory. (See Appendix IV.) The connection weights between neuron in the network were computed off-line and set in the network. The network consisting of 32x32 binary neurons was implemented in software. The network was formed from sinogram representations of three test targets: scale models of a B-52, AWAC, and Space Shuttle. The sinogram representation is basically a binarized cartesian plot of range-profiles versus aspect angle for a fixed elevation angle of the target. When tested with partial versions of a sinogram, the network was able to classify the target to which the data belonged correctly. Partial data, down to a fraction of nearly 10% of the full sinogram representation was found able to produce correct classification of the three targets. This network demonstrated clearly the distinctive features of neural processing i.e. collective, and nonlinear, signal processing as compared to conventional signal processing: the functions of data storage, processing, and object labeling are performed by the same elements of the network. This is unlike conventional signal processing where these functions are normally carried out by separate elements of the system. This means that, when the network is mplemented in hardware, the three functions listed above, wold be carried out by the same hardware. The network required in its operation that the aspect angles at which the test data were collected be known. Although it is possible to obtain this information, it dictates in practice the use of auxilliary tracking radars and additional signal preprocessing to determine the target orientation relative to the radar line-of-sight at which the range profile data comprising the test data was acquired. This complication can be avoided if one can design a network capable of classifying a target from few echos or from a single echo or "look" (single range-profile) without having to specify at what aspect angle of the target the echo occurs. This capability is highly desirable and is important from a practical viewpoint.

To investigate the feasibility of robust radar target recognition from a single look we examined next the performance of a multilayered feedforward error back-propagation network. The network we set up was an outcome of an investigtion we carried out of a learning network for extrapolation and target identification. This network (see Appendix VI), consisted of three layers: an input layer of 101 complex neurons representing the complex frequency response of the target, a hidden layer of 101 real neurons, and an output layer of $N=2$ binary neurons capable of presenting $2^N=4$ target labels which can classify up to four targets. The connection weights between the input layer and the hidden layer are those of the discrete Fourier transform kernel and are fixed. The connection weights between the hidden layer

and the output layer are adaptive and are determined by an error driven supervised learning algorithm. The network was trained on the (6-17)GHz frequency response data of three test objects: scale models of a B-52, a Boeing 707 and a space shuttle. We found this net can learn the frequency responses, or corresponding range-profiles, of the three test targets constituting the training set. Following training, the net is able to classify any one of the frequency responses of an object presented to it by associating it with the correct object label formed by neurons of the output layer. When a two-out-of-three majority vote was adopted in keeping score of the network's performance as frequency response echos were presented to it, the score was found to be perfect even when only 35% of the training set of each target was employed in training the network. This constitutes good generalization and means that a network need not be trained with very large numbers of feature vectors before it can capture the underlining structure of the target. It is worh noting, that unlike the preceeding network this network does not require aspect information in its performance. In addition it was found that the network has excellent robustness. In that the excellent performance cited above can be maintained even at very low signal-to-noise ratio and over very wide dynamic range of the frequency response data. (See Appendix VI for detail.) The network achieves, despite its simplicity (it is essentially a one layer perceptron network), our stated goal namely that of robust distortion invariant classification of training targets.

At this stage of our research we thought that we had realized the task we set out to achieve. We were quickly disappointed. Despite of the excellent performance capabilities cited above, neither this network, nor the network described before, are of any practical use. Both networks lack cognitive ability. When presented with novel data from a target the net has not been trained upon, i.e. has not seen before, it could, because of the lack of cognition, classify it erroneously as one of the targets it has learned. This lack of cognition is a serious problem facing practical applications of neural network that need to operate in complex uncontrolled environments. This point requires some clarification. One can train a network for example to recognize handwritten zip code numbers. The trained network is useful because it is only meant to recognize zip code numbers. No one is going to use it to recognize the Japanese alphabet for example. It is designed to operate in a controlled environment. This is not true for a neural net designed to recognize radar targets because the environment in which the net is intended to operate is not controlled. Targets other than those the network is trained to recognize can occur in its environment. There are two possible solutions to this problem that come to mind. One is to train the network with every target it could conceivably encounter in its environment. This is not practical, because even if details can be worked out, it would result in very large networks of unacceptable size. The second solution, and this is often invoked by workers in the field when they realize that the network they developed is not cognitive, is to incorporate a "novelty filter." This consists of using auxilliary gear that can measure other attributes of the target such as size, speed, altitude, etc. and use these attributes to decide whether the target encountered is of interest or not, i.e., whether the output of the neural network engaged is to be taken seriously or not. The disadvantage of this approach is increased complexity and cost

4

of the data acquisition system. Biological neural networks possess inherent cognitive abilities. There is no doubt that multisensory modalities; which can be viewed as providing something akin to novelty filtering, are involved in networks of the brain to reduce ambiguities. There must be however more to it than that. We have started recently a study of the issue and are finding the results obtained so far most intriguing. We believe this study will lead to ways of designing a new generation of neural networks with inherent cognitive ability. Before discussing our findings in this regard we will briefly summarize the findings of our investigation in data acquisition and representation.

The range-profile of a target for a given aspect resembles the impulsive plane wave illumination of the target for that aspect provided the spectral window used in data acquisition is sufficiently wide. A general criterion for selecting the spectral width Δf is $\delta = c/2\Delta f$ where δ is the desired range resolution on the target and c is the velocity of light. In general terms, δ corresponds to the size of the finest detail on the target (and hence in its image) needed to distinguish it from other targets. Because the form of the echo (temporal impulse response) produced by an impulsive plane wave sweeping the target is independent of range to the target (it only depends on aspect), range-profile data ensures, when used as feature vector in a neural based radar target recognition scheme, that performance is independent of range. Invariance with target location within the field of view is obtained then by aiming the T/R antenna of the acquiring radar at the target at all times by precise tracking. Invariance with aspect is achieved then by training a suitable neural network with the normalized range-profile data collected over the solid angle of encounter of every target the network is required to learn. Angular sampling considerations applied to a target of extent L dictate that the number of range-profiles needed to characterize the target is given by $N = \Omega/\delta\Omega$ where $\delta\Omega \approx (\overline{\lambda}/L)^2$ with $\overline{\lambda}$ being the mean wavelength used in data acquisition and Ω is the solid angle of encounter. Values of N for typical aerospace targets and practical spectral windows can therefore be quite large. The generalization ability of trainable neural networks discussed earlier means that the network need not be trained with every one of its N range-profile but only with a fraction of them which we call the training set. This helps reduce training time. The training set can be selected randomly or uniformly over the solid angle of encounter.

The ultimate goal of our data acquisition and representation effort is to show that range-profile data collected in a controlled anechoic chamber environment employing scale models of targets of interest can, by paying careful attention to scaling issues based on the principle of electromagnetic similitude [5], be used to recognize the actual size targets by conventional broad-band coherent radar systems in the field. When the conductivity σ of scale models and actual targets is very high ($\sigma \to \infty$), electromagnetic similitude considerations show that scaling is satisfied when data acquisition with a scale model that is n times smaller than the actual target is carried out over a frequency range that is n times greater than frequency range of the actual radar used in the field.

We return now to describing our findings so far regarding introducing cognition to neural networks. The majority of neural networks described in the literature, compute by forming point attractors in phase-space with prescribed basins of attraction. We have recently described an error-driven algorithm for forming *string attractors* in phase-space of networks with synchronously updated neurons and proposed its use in target recognition, [6] (see also Appendix VII). A string attractor is basically a point attractor with filamentary, rather than "volumetric", basin of attraction. Synchronicity and its role in feature binding is receiving increased attention in the literature [7]-[9], but the question of how to achieve feature binding in practice has thus far received little attention. The learning rule given in [6] for forming a string attractor, i.e. storing a sequence of vectors in a network, applies also to forming a *periodic attractor* by closing the string on itself. The characteristics of periodic and string attractors, revealed so far in our work are: (a) High storage capacity $M \geq N$ where M is the number of vectors stored in the sequence and N is the number of neurons in the network. For example, M=40 bipolar binary vectors were stored in a network of N=32 bipolar binary neurons in less than 50 training cycles. (b) Arbitrary (i.e. highly correlated and nonorthogonal) vectors can be stored in sequence. (c) Initiated from any member of the stored sequence, a string attractor network cycles through all subsequent vectors and terminates on the last stored vector in the string, while a periodic attractor network would cycle repeatedly through all vectors stored which is equivalent to producing a periodic spatio-temporal oscillation of states of the neuron population. (d) Highly isolated periodic and string attractors are formed with the degree of isolation controlled by the threshold level of neurons. By this we mean, for relatively high neuron thresholds, initiators (initiating state vectors) with Hamming distance $d_H > 1$ from any of the stored vectors do not trigger the periodic attractor but cause the network instead to *bifurcate* and converge to a limit point which is usually a ground state or one close to it. (e) Several nonintersecting periodic or string attractors may be stored in the same network. (f) The learning rule in [6] for storing sequences scales well with network size, for instance, networks with 32, 64 and 128 neurons were tested and all showed similar behavior. (g) Sequence of arbitrary unipolar binary vectors can also be stored provided the vectors are not too sparse.

Periodic attractor networks with the above-listed properties, and particularly (d), offer a possible mechanism for cognition in that when the vectors stored are feature vectors representing an object in its different manifestations, and the initiating vector is one of the stored feature vectors, or is close to any one of them in the Hamming sense (e.g. $d_H \leq 1$), the periodic attractor will be triggered. Now if a label vector, identifying the object, was imbedded earlier on in the periodic attractor when it was formed, it would also be triggered once every period signaling thereby that the input is one of the feature vectors stored. Because of the high degree of isolation of a periodic attractor achieved by proper choice of neuron threshold an initiating input vector with Hamming distance $d_H > 1$ would not trigger the sequence or the imbedded label. Instead, the network bifurcates and switches its

operation to computing with point attractors whereby it proceeds to converge rapidly to a fixed ground state, where all neurons are in their low binary state, or one close to it and this would serve as an indication within the network that the input is not familiar providing thus cognition.

Feature vectors of more than one object can be stored in separate non-intersecting periodic attractors containing imbedded labels in the same network. Attractors and labels are triggered in such a network only if the initiator is of Hamming distance $d_H \leq 1$ from one of the vectors stored in an attractor. Novel initiators will not trigger any of the labels and this provides such a network with ability to finely distinguish if certain feature vectors are present in its environment.

Despite its potential usefulness for feature binding, periodic attractor networks are void of generalization because of their high isolation. A slight change in a feature vector that triggers the attractor renders it ineffective causing the network to bifurcate. This means that a recognized object can stop being recognized if its feature vectors change to the slightest. This suggests that periodic attractor networks need to be used with additional networks that can furnish the generalization capabilities needed in order to provide the composite network with cognition and robustness at the same time. Presently, we are seeking methods for imparting prescribed domains of attraction for each vector stored in the periodic attractor. This would provide the periodic attractor with controlled basin of attraction. Initial results suggest that this can be achieved by combining periodic attractor networks with arrays of feedforward feature extracting networks. Advantages of this hierarchial approach to network construction we are noting at this very preliminary stage, are modularity and potential reduction of learning time even in large networks because of segmentation. All this appears to be achieved while enjoying the good robustness and noise immunity of feedforward learning networks. Although such feedforward networks provide robustness and noise immunity, they lack cognition. Cognition is provided by the periodic attractor. This approach could provide us, for the first time, with a way for combining distinct neural network or neural modules in such a way as to achieve higher level processing such as cognition.

Finally we report on our findings in the area of photonic or optoelectronic implementation of neural networks. Interest in artificial neural networks implemented in analog hardware rather than digital software stems primarily from their potential speed advantage. The photonic approach is motivated by the desire to combine the best attributes of optics, namely parallelism and massive interconnectivity, with the best attributes of electronics, decision making (nonlinearity) and gain. During the period of this report we designed constructed and studied the performance of what we believe to be the first stochastic photonic learning machine (see Appendix VIII for detail). Learning in this machine is stochastic taking place in a self-organizing tri-layered opto-electronic neural net with plastic connectivity weights that are formed in a programmable nonvolatile spatial light modulator. The net, which can also be called a *Boltzmann Learning Machine,*

learns by adapting its connectivity weights in accordance to environmental inputs. Learning is driven by error signals derived from state-vector correlation matrices accumulated at the end of fast annealing bursts that are induced by controlled optical injection of noise into the network. Operation of the machine is made possible by two important developments in our work: Fast annealing by optically induced noisy thresholding, and stochastic learning with binary weights. Results obtained with a 24 neuron prototype partitioned into three layers with 8 input, 8 hidden, and 8 output neurons show that the machine can learn, with a score of about 95%, to associate two 8-bit vector pairs in 10-60 minutes with relatively slow (60 msec response time) neurons. Shifting to neurons with 1 μsec response time for example, could reduce the learning time by roughly 10^4 times. Slow neurons were deliberately used to make it easier to visually examine and record the changing state vector of the network as it operates which is displayed with an array of LEDs. Increasing the number of hidden neurons in this machine from 8 to 16 is shown, by numerical simulations, to increase the learning score to 100%. The spatial light modulator (SLM) used in constructing the machine had to be of the nonvolatile variety. The one such SLM available to us at the time, (and still is) was the magneto-optic SLM. A scheme for enhancing the frame rate of this SLM from video rate to 1000 frames/sec to speed-up learning was developed [10]. Unfortunately, the pixels of this device have binary (on-off) transmission only. This restricted the connection weights of the neurons in the machine to binary values. All adaptive learning algorithms require analog weights. To overcome this limitation we developed a scheme for Boltzmann machine learning with binary weights (see Appendix VIII). Although effective in learning, the number of associations the network could learn with the binary weights scheme is less than what it can learn with analog weights. This underlines the importance of developing programmable nonvolatile spatial light modulators for use in photonic learning machines.

3. LIST OF PUBLICATIONS

1. N. Farhat and B. Bai, "Echo Inversion and Target Shape Estimation by Neuromorphic Processing," Neural Networks, Vol. 2, pp. 117-125, 1989.

2. H.J. Li, N.H. Farhat and Y. Shen, "Image Interpretation and Prediction in Microwave Diversity Imaging," IEEE Trans. on Geoscience and Remote Sensing, Vol. 27, Jan. 1989, pp. 98-101.

3. H.J. Li, N.H. Farhat and Y. Shen, "Range Profiles and Images of a Loaded Straight Wire," IEEE Trans. on Antennas and Propagation, Vol. 37, Jan. 1989, pp. 94-99.

4. N.H. Farhat, "Microwave Diversity Imaging and Automated Target Identification Based on Models of Neural Networks," Proc. IEEE Special Issue on Radar Cross-Section of Complex Objects, Vol. 77, May 1989, pp. 670-680. (Invited).

5. N.H. Farhat and H. Babri, "Phase-Space Engineering for Neurodynamic Target Identification," Proc. IEEE - APS Int. Symp. and URSI Radio Science Meeting, Vol. II, pp. 768-771, IEEE Cat. No. CH-2654-2/89 June 1989.

6. N.H. Farhat and Z.Y. Shae, "Scheme for Enhancing the Frame Rate of Magneto-Optic Spatial Light Modulators," Applied Optics, Vol. 28, pp. 4792-4800, Nov. 1989.

7. N.H. Farhat, "Optoelectronic Neural Networks and Learning Machines," IEEE Circuits and Devices Magazine, Vol. 5, pp. 32-41, Sept. 1989 (Invited).

8. N.H. Farhat, "Photonic Neurocomputers and Learning Machines," Proc. IEEE Int. Symp. on Circuits and Systems, Vol. 1, pp. 696-699, (Invited).

9. N.H. Farhat, "Photonic Neurodynamical Systems for Learning and Cognition," Proc. OSA Topical Meeting on Nonlinear Dynamics in Optical Systems, (To be Published) (Invited).

Related Publications:

1. T. Chu and N. Farhat, "Polarization Effects in Microwave Diversity Imaging of Perfectly Conducting Cylinders," IEEE Trans. on Antennas and Propagation, Vol. 37, Feb. 1989, pp. 235-244.

2. N. Farhat and Z.Y. Shae, "An Optical Learning Machine," Proc. 1989 Hawaii International Conference on System Science, IEEE Cat. No. 89TH0242-8, p. 432 1989.

4. LIST OF PARTICIPATING SCIENTIFIC PERSONNEL AND ADVANCED DEGREES EARNED

N. Farhat - Principal Investigator

Z. Zhao - Research Associate

Graduate Research Fellows:

    B. Bai
    H. Babri
    A. Grott
    U. Lee
    K.S. Lee

Advanced Degrees Earned:

K.S. Lee - Ph.D Dissertation entitled: "A New Approach to Optical Information Processing Based on Neural Models with Application to Object Recognition." (Dec. 1987)

U. Lee - MSc. Thesis entitled: "High Resolution Microwave Imaging Facility with Extended Bandwidth." (June 1988)

B. Bai - Ph.D Dissertation entitled: "Image Reconstruction and Target Identification Based on Neural Models." (Aug. 1990)

5. REFERENCES

1. E.D. Mese, et. al., "Target Identification by Means of Radar," Microwave Journal, pp. 85-103, December 1984.

2. D.G. Dudley, "Progress in Identification of Electromagnetic Systems," IEEE Ant. and Prop. Newsletter, pp. 5-11, August 1988.

3. E.M. Kennaugh and D.L. Moffat, "Transient and Impulse Response Approximations," Proc. IEEE, Vol. 53, August 1965.

4. C.E. Baum, "The Singularity Expansion Method," in Transient Electromagnetic Fields, L.B. Felson (Ed.), Springer-Verlag, Berlin Heidelberg, (1976).

5. J.D. Stratton, "Electromagnetic Theory", Mc-Graw Hill, New York, (1941), pp. 48-490.

6. N. Farhat and H. Babri, "Phase-Space Engineering for Target Identification," Proc. IEEE AP-S International Symposium, Vol. II, pp. 768-771, IEEE Cat. No. CH-2654-2/89, (1989).

7. C.M. Gray, P. Köenig, A.K. Engel and W. Singer, "Oscillatory Responses in Cat Visual Cortex Exhibit Inter-Columnar Synchronization Which Reflects Global Stimulus Properties," Nature, Vol. 338, pp. 334-337 (1989).

8. R. Eckhorn, H.J. Reitboek, M. Arndt and P. Dicke, "Feature Linking Via Stimulus-Evoked Oscillations: Experimental Results From Cat Visual Cortex and Functional Implications From a Network Model," Proc. IJCNN'89, Vol. I, pp. I-723-I-730, IEEE Cat. No. 89 CH2765-6, (1989).

9. G. Hartman and S. Drue, "Feature Linking by Synchronization in a Two-Dimensional Network," Proc. IJCNN'90, Vol. I, pp. I-247-I-250, Lawrence Erlbaum Associates, Publishers, Hillsdale, NJ, (1990).

10. N.H. Farhat and Z.Y. Shae, "Scheme for Enhancing the Frame Rate of Magneto-Optic Spatial Light Modulators," Applied Optics, Vol. 28, pp. 4792-4800, Nov. 1989.

6. APPENDICES

Appendix I

Image Interpretation and Prediction in Microwave

Diversity Imaging

Hsueh-Jyh Li

Nabil H. Farhat

Yuhsyen Shen

Image Interpretation and Prediction in Microwave Diversity Imaging

HSUEH-JYH LI, NABIL H. FARHAT, AND YUHSYEN SHEN

Abstract—The microwave image of a metallic object is interpreted from a new point of view, based on the understanding of the interconnection between the scattering mechanisms, the data acquisition system, and the image reconstruction algorithm. From this understanding we are able to interpret and predict microwave images reconstructed from data collected over specified and angular windows. The connection between a special scattering mechanism, edge diffraction, and its reconstructed image is established. The microwave image of an edge will be two bright points whose locations correspond to the end points of the edge if the normal aspect angle is not included in the angular windows; otherwise a line joining the two end points and representing the edge will appear in the image. Experimental images of a trihedral reflector reconstructed from data collected over different angular windows support this new approach to image interpretation and prediction.

Spectral

I. INTRODUCTION

Microwave diversity imaging is an imaging technique that exploits possible degrees of freedom, including spectral, angular, and polarization diversities [1]. In this imaging system, an object is seated on a rotating pedestal and is illuminated by a plane wave. For each aspect angle a set of pulses at different frequencies is transmitted and its echoes are received. The object is then rotated and the measurement is repeated to obtain the multiaspect stepped frequency response of the scattering object.

In the microwave regimes, the physical optics (PO) approximation is usually used to model the scattered field of a conducting object. It was shown that a three-dimensional (3-D) Fourier transform (FT) relationship exists between the shape of a perfectly conducting object and its backscattered far field under the PO approximation [2]. However, the PO approximation is inadequate for scattering problems of a complex shaped conducting object. At high-frequency edge diffractions, multiple reflections, creeping waves, and surface traveling waves are also important scattering mechanisms [3]. A field scattered from these scattering mechanisms cannot be treated by the PO approximation. Additionally,

the spectral and angular windows for the data are usually restricted by practical constraints. Therefore, the microwave image of a metallic object might be different from its geometrical shape.

In this paper we will investigate microwave images of metallic objects employing microwave diversity imaging from a new point of view, based on the understanding of the interconnection between the object scattering mechanisms, the data acquisition system, and the image reconstruction algorithm utilized in image retrieval. The image reconstruction algorithm can be either the Fourier transform method or the back-projection method, and these two methods yield equivalent results [1], [4]. However, the back-projection method provides more physical insight into the image formation process [5]. Basically, the image is formed in three steps: 1) measure the scattered field over a specified spectral window and angular window; 2) obtain the range profile, which is the inverse FT of the range-corrected frequency response, at each aspect angle; and 3) back-project the range profile of each aspect angle onto an image plane to obtain the image. We will interpret and predict the microwave image based on the above three steps.

A different scattering mechanism might produce a different appearance in its microwave image. In this paper we will only deal with a special scattering mechanism—edge diffraction. For those objects consisting of conducting plates, edge diffractions are dominant contributors to the scattered field when the receiver is not in the specular direction of any one of the visible plates comprising the object. To a first order approximation the field scattered from the above type objects can be considered as a summation of the contributions from each "visible" plate, and the scattered field of a plate can be considered as a summation of the diffracted field from each "visible" edge. Therefore, diffraction from an edge is the basic building block for the scattering problem of those objects consisting of conducting plates.

In Section II the scattered field from an edge with finite length will be reviewed, the physical properties of its range profile will be explained, and the image formation for an edge with finite length will be discussed. A trihedral reflector is an object consisting of conducting plates. Experimental images of a trihedral reflector reconstructed from data collected over different angular windows will be demonstrated and interpreted in Section III.

II. SCATTERED FIELD, RANGE PROFILE, AND IMAGE FORMATION OF A FINITE EDGE

Consider a conducting plate placed on a rotating pedestal as illustrated in Fig. 1. Points P_1 and P_2 are two vertices of the plate and the line P_1P_2 forms an edge of the plate. In the laboratory coordinate system, define the z-axis in the direction of the rotational axis, and the t-axis in the direction of the line of sight. At the starting angle the polar coordinates of the end points P_1 and P_2 are (r_1, θ_1, ϕ_1) and (r_2, θ_2, ϕ_2), respectively. As the plate is rotated with an angle ϕ the coordinates of P_1 and P_2 become $(r_1, \theta_1, \phi_1 + \phi)$ and $(r_2, \theta_2, \phi_2 + \phi)$, respectively. The differential ranges of these two end points at rotation angle ϕ are then $r_1 \sin \theta_1 \cos (\phi_1 + \phi)$ and $r_2 \sin \theta_2 \cos (\phi_2 + \phi)$, respectively. It is noted that the dependence of the differential ranges of the end points on the rotation angle is sinusoidal.

Next we define an edge-fixed coordinate for the plate. Let the z'-axis be in the direction of the edge P_1P_2, and the x'-axis be normal to the edge and lying on the plate surface. The corresponding inclination angle of the transmitter/receiver to the edge-fixed coordinate system is θ' ($\phi = 0°$). As the plate is rotated through an angle ϕ, the corresponding inclination angle for the edge-fixed coordinate system becomes $\theta'(\phi)$. It is noted that θ' is not only a function of ϕ but also a function of the orientation of the plate and the edge.

The diffracted field of a wedge with finite length for arbitrary incident and diffracted angles has been treated [6], where the con-
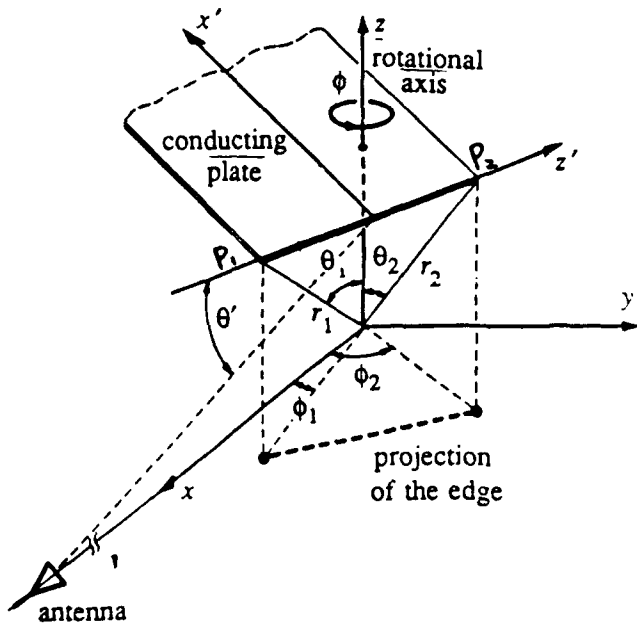
Fig. 1. Geometry and coordinates of an edge in the laboratory coordinate system and edge-fixed coordinate system.

DIFFERENTIAL RANGE

(a)

(b)

(c)   (d)

Fig. 2. Image formation of an edge. (a) Sketch of the range profiles of an edge at various aspect angles. (b) Implementation of the back-projection. Sketches of the images after back-projection (c) including and (d) without the aspect angle such that the edge is normal to the line of sight.

cept of equivalent electrical current and equivalent magnetic current has been applied. Denote the equivalent electric current and equivalent magnetic current on the edge as $I(z')$ and $M(z')$. The expressions of I and M for the backscattering case can be found in [6]. They are functions of the inclination angle and the azimuth angle, and are inversely proportional to the wavenumber k.

The backscattered field of an edge with finite length L expressed in the edge-fixed coordinate system can be written by [6]

$$E_\theta = \frac{j\omega\mu_0}{4\pi} \frac{e^{-jkr}}{r} \sin\theta' I(0) L \frac{\sin(kL\cos\theta')}{kL\cos\theta'} \qquad (1)$$

$$E_\phi = \frac{j\omega\mu_0}{4\pi} \frac{e^{-jkr}}{r} \eta \sin\theta' M(0) L \frac{\sin(kL\cos\theta')}{kL\cos\theta'} \qquad (2)$$

where $I(0)$ and $M(0)$ are the equivalent electric current and equivalent magnetic current at $z' = 0$, and η is the characteristic impedance of the free space.

At a specific aspect the range profile is obtained by FT the range-corrected frequency response. After range correction (i.e., the first two terms on the right of (1) and (2) being removed), the range-corrected field can be further simplified to

$$E_\theta' = \sin\theta' I(0) L \frac{e^{jkL\cos\theta'} - e^{-jkL\cos\theta'}}{2jkL\cos\theta'} \qquad (3)$$

$$E_\phi' = \eta \sin\theta' M(0) L \frac{e^{jkL\cos\theta} - e^{-jkL\cos\theta}}{2jkL\cos\theta'}. \qquad (4)$$

The FT of (3) and (4) with respect to $2k$ over a finite bandwidth will give two peaks, located at range about $\pm(L/2)\cos\theta'$, which are at the differential ranges of the end points of the edge, with amplitude proportional to $I(0)$ or $M(0)$, and $1/(L\cos\theta')$ if $\theta' \neq 90°$. At the rotation angle ϕ such that $\theta'(\phi) = 90°$, the range profile gives a single peak with strong magnitude because the two end points of the edge have the same differential ranges and all the points on the edges are in equidistance to the observation point.

After realizing the aspect dependence of the range profile of the edge, we can then form and predict the image of an edge by the technique of back-projection [4], [5], [7]. After back-projection, the contributions of a specific range profile to the reconstructed image will be two parallel lines oriented in the direction of ϕ. Because the trace of each end point versus the rotation angle is a sinusoidal, all back-projection lines for various rotation angles will
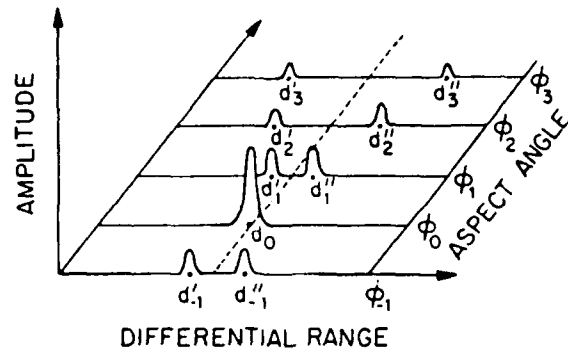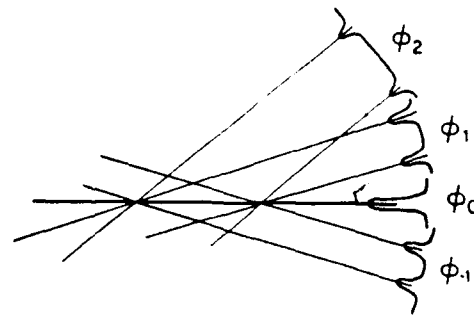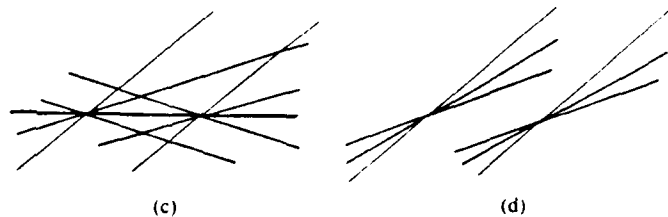
pass through the corresponding end point as in the case of computer-aided tomography (CAT), intensifying the brightness of the end points. However, when the aspect such that $\theta'(\phi) = 90°$ is within the angular window (i.e., the aspect at which the incident wave is normal to the edge is contained within the angular window), the back-projection due to this range profile will be a single bright line.

The above explanation is illustrated in Fig. 2. At rotation angle ϕ_0 the edge is normal to the line of sight (i.e., $\theta'(\phi_0) = 90°$), and the range profile for that aspect has a single peak with large amplitude. When plate is rotated to another angle ϕ, the range profile has two peaks located at d_i' and d_i'' with smaller amplitudes (see Fig. 2(a)). The implementation of back-projection is illustrated in Fig. 2(b). The sketches of the image after back-projection including and excluding the specular aspect are shown in Fig. 2(c) and (d), respectively. The above discussions and illustrations indicate that the microwave image of an edge will be two bright points whose locations correspond to the end points of the edge if the normal aspect angle is not included in the angular window; otherwise a line joining the two points and representing the edge will appear in the image.

III. Microwave Images of a Trihedral Reflector

To verify the new interpretation approach, the microwave images of a trihedral reflector reconstructed from data collected over various angular windows are demonstrated below.

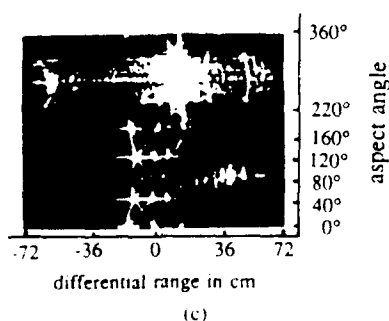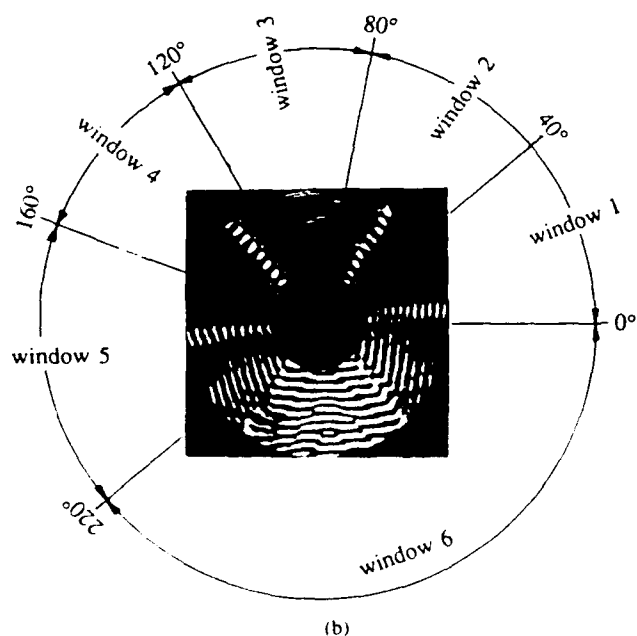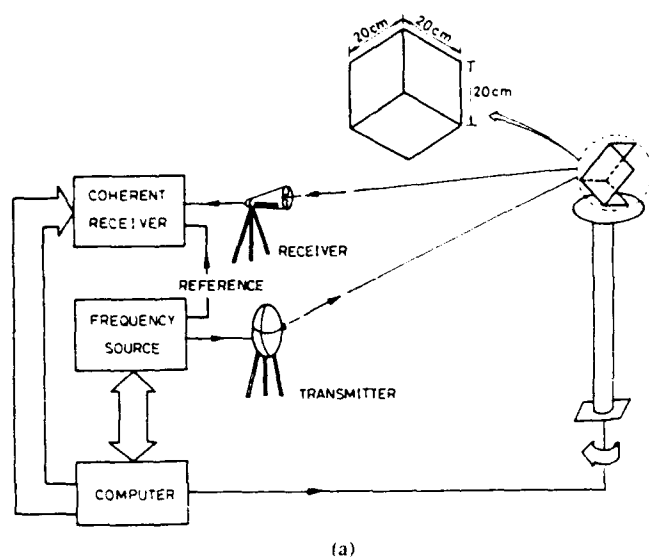The geometry of a trihedral reflector and the imaging arrange-

(a)

(b)

(c)

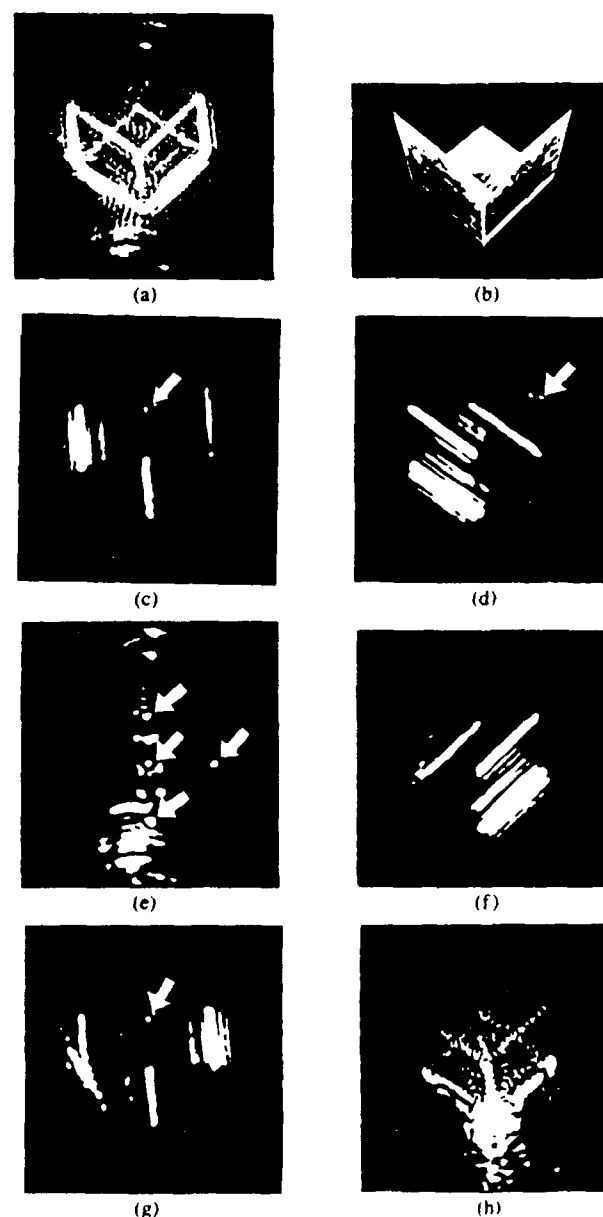(d)

(e)

(f)

(g)

(h)

Fig. 4. Photo image and microwave images of a trihedral reflector. (a) Microwave projective image reconstructed from data collected over angular window from $\phi = 0°$ to $220°$. (b) Projective photo image. Microwave projective images reconstructed from data collected over (c) angular window 1 ($\phi = 0°$ to $40°$); (d) angular window 2 ($\phi = 40°$ to $80°$); (e) angular window 3 ($\phi = 80°$ to $120°$); (f) angular window 4 ($\phi = 120°$ to $160°$); (g) angular window 5 ($\phi = 160°$ to $220°$); and (h) angular window 6 ($\phi = 220°$ to $360°$).

(c)

Fig. 3. Geometry, imaging arrangement, fringe pattern, and sinogram of a trihedral reflector (a) Geometry and imaging arrangement of a trihedral reflector (b) Real part of the range-corrected frequency response of the trihedral (c) Sinogram of the trihedral reflector

ment are shown in Fig. 3(a). The transmitting and receiving antennas have opposite senses of circular polarization. 101 equal frequency steps covering the 6-16.5 GHz range were used to obtain the frequency response of the trihedral reflector. The object is rotated clockwise 360°. The real part of the range-corrected complex

frequency response of the trihedral reflector is shown as a central slice of Fourier data in Fig. 3(b). The radial distance of a given sample in this plot represents the frequency while the polar angle represents the rotation angle ϕ. The brightness of each point is proportional to the amplitude of the frequency response. The range profiles for all aspect angles are represented as a sinogram. The sinogram representation has been used in CAT [7] and is applied here to represent the range profiles of various aspect angles. It is a 2-D intensity varied display with the abscissa of the differential range, the ordinate of the aspect angle, and the intensity or brightness proportional to the amplitude of the range profile. The sinogram of the trihedral reflector is shown in Fig. 3(c). The bottom line represents the range profile of the first aspect ($\phi = 0°$) while the top line represents the range profile of the last aspect angle.

The magnitude of the range profile is proportional to the brightness of the display and the sinogram is displayed in linear scale. The dynamic display range has been suitably chosen so that weak signals will not be overridden. Examining the sinogram one can find that bright points are present in certain aspect angles. Locations of these bright points correspond to the differential ranges of the "visible" edges that are normal to the line of sight.

The image reconstructed through an angular window covering from $\phi = 0°$ to $220°$ is shown in Fig. 4(a). It is seen that the image is a projective image projected onto the plane normal to the rotational axis. The optical projective image is also shown in Fig. 4(b) for comparison. To verify our new image interpretation approach stated in the previous section. we divide the whole angular window into six subwindows and reconstruct the image from each subwindow. The resultant images are shown in Fig. 4(c)–(h). Examining the resultant images. one can find that only those edges that are normal to the line of sight within the specified angular window appear in the image. The brightness of the end points of the edges has been intensified. It is noted that no edges are normal to the line of sight in angular window 3. Accordingly, no edges are present in the image while the brightness of the vertices are intensified. Furthermore, the effect of multiple reflections is pronounced for some aspects in this window as can be seen from the fringe pattern (Fig. 3(b)) and the sinogram (Fig. 3(c)). Multiple reflection usually distorts the image because the range profile does not reflect the range information of the object shape [5]. [8]. In angular window 6 strong multiple reflections are dominant contributors to the scattered field for most aspects. Although the edges can still be seen in the image, artifacts due to multiple reflections distort the image.

IV. DISCUSSION AND CONCLUSION

In this paper we interpret the microwave image of a metallic object from a new approach. based on the understanding of the interconnection between the scattering mechanisms. the data acquisition system. and the image reconstruction algorithm. From this understanding we can interpret and predict the microwave image reconstructed from data collected over specified spectral and angular windows. Experimental results support this new approach to image interpretation. Although the scattering mechanism treated in this paper is confined to the edge diffraction. the same approach can also be applied to establish the connection between the other scattering mechanisms and their reconstructed images [5]. Successful interpretation and prediction of the microwave image are fundamental to research in several areas. including target identification. classification. radar cross-section reduction. and image distortion [8].

REFERENCES

[1] N. H. Farhat. C. L. Werner. and T. H. Chu. "Prospect for three-dimensional projective and tomographic imaging radar networks." *Radio Sci.*, vol. 19. no. 5. pp. 1347–1355. 1984.

[2] N. Bojarski. "Inverse scattering." Nav. Air Syst. Command. Warminister. PA. Final Rep. N000-19-73-C-0312F. Feb. 1974.

[3] G. T. Ruck. D. E. Barrick. W. D. Stuart. and C. K. Krichbaum. *Radar Cross Section Handbook.* New York: Plenum. 1970.

[4] N. H. Farhat and T. H. Chu. "Tomography and inverse scattering." *International Commission on Optics.* vol. ICO-13. pp. 62–63. 1984.

[5] H. J. Li. N. H. Farhat. Y. Shen. and C. L. Werner. "Image understanding and interpretation in microwave diversity imaging." *IEEE Trans. Antennas Propagat.* to be published.

[6] A. Michaeli. "Equivalent edge currents for arbitrary aspects of observation." *IEEE Trans. Antennas Propagat.* vol. AP-32. no. 3. pp. 252–258. 1984.

[7] G. T. Herman. Ed.. *Image Reconstruction from Projections.* New York: Springer-Verlag. 1979.

[8] H. J. Li. N. H. Farhat. and Y. Shen. "Radar cross section reduction and image distortion employing microwave diversity imaging." submitted for publication.

Appendix II

Range Profiles and Images of a Loaded Straight Wire

Hsueh-Jyh Li

Nabil H. Farhat

Yuhsyen Shen

Range Profiles and Images of a Loaded Straight Wire

HSUEH-JYH LI, MEMBER, IEEE, NABIL H. FARHAT, FELLOW, IEEE, AND YUHSYEN SHEN, MEMBER, IEEE

Abstract—The range profiles and images of a straight wire without and with lumped impedance loading are discussed and demonstrated. The scattering mechanisms of a straight wire are qualitatively analyzed. Plots of range profiles at different aspect angles show that surface traveling waves are important scattering mechanisms of a straight wire. The presence of traveling waves makes ringlike artifacts appear in the reconstructed images. It is found that lumped impedance loading can effectively distort the range profiles and microwave images of a wire scatterer. In addition, randomly varied reactive loading can generate random peaks in the range profiles.

I. INTRODUCTION

THE PROPERTIES of the field scattered from a scatterer loaded with lumped impedance have been extensively studied [1]–[3]. Several interesting phenomena can then be deduced from the variation of the scattered fields. Fixed linear impedance loading can change the natural frequencies of a target [4]. Time-varying loading can make the receiver unable to phase lock to the frequency of the incident wave and can shift the apparent frequency of the scattered field to provide a false Doppler shift [3]. It can also spread the spectrum of the scattered field to decrease the energy within the bandwidth of a receiver [5]. The sensitivity of these phenomena to impedance loading has been discussed in [5].

In this paper, we will discuss two other properties, range profiles and images of a straight wire without and with lumped impedance loading. The range profile of a scatterer at an aspect is defined as the Fourier transform (FT) of the frequency response of the scattered field at that aspect. Range profiles can give useful insight into the scattering mechanisms of a scatterer. After the range profiles are obtained, an image can then be formed by back projecting the complex range profiles at various aspects into the imaging plane [6]. Microwave images of conducting objects have been interpreted satisfactorily through the understanding of the scattering mechanisms of the object and the procedures of the image reconstruction algorithm [7]. Different scattering mechanisms can produce different appearances of microwave images. It was reported that a surface traveling wave is the dominant

scattering mechanism for the backscattered field of a long thin wire with near end-on incidence [8]. Therefore, it will be of interest to examine the appearance of the image for objects with this special scattering mechanism.

In some applications it is desirable to distort the image of a target so that it cannot be recognized by radar [9]. If the wire is loaded with impedance, the impedance discontinuities on the wire surface will cause extra radiation. The effect of impedance loading on microwave images has not yet been reported. Monochromatic imaging of a monopole antenna has been studied holographically by Iizuka and Gregoria [10], who was interested in visualizing resonance effects. However, what we are interested in is a wire scatterer rather than an antenna and a frequency diversity image instead of a monochromatic image.

In this paper we will use the moment method to numerically calculate the field scattered from a loaded straight wire scatterer and derive its range profile and microwave image from the calculated scattered fields. A qualitative analysis of the scattering mechanisms of a straight wire will be given first. This analysis is then examined via plots of the numerical and experimental range profiles, which are then compared with the experimental results. The effect of impedance on the range profiles and the reconstructed images will be presented and discussed.

II. SCATTERING MECHANISMS OF A STRAIGHT WIRE

Radiation can originate from several places on an arbitrarily shaped wire object. These include the excitation region, an impedance load, a change in radius, a sharp bend, a smooth curve, and an open end [3]. Consider a straight wire illuminated by an impulsive plane wave with angle of incidence θ as shown in Fig. 1. In this scattering arrangement the only places which cause radiation are the end points of the wire. The pulse traveling in free space impinges on the upper end point first. Part of the incident energy is then reradiated, and the remaining energy continues to travel along the wire. This traveling pulse will be partly reradiated when it reaches the lower end and partly reflected upward along the wire. This process of radiation and reflection continues until the pulse dies out. The original pulse propagating in free space hits the lower end point some time after it impinges on the upper end point. The process of radiation, reflection, and guided propagation along the wire will then occur just as in the case of the upper end point. Different wave motions resulting from multiple interactions between the ends of the wire are indicated in Fig. 1. The differential path length l_i, which is the ith wave motion path relative to the path length when the
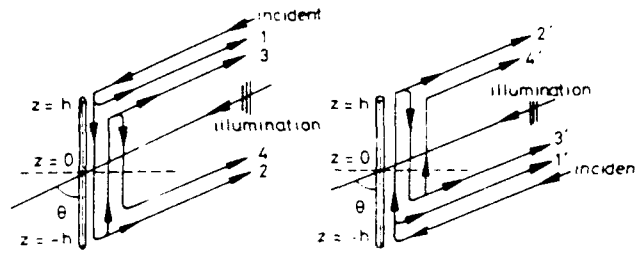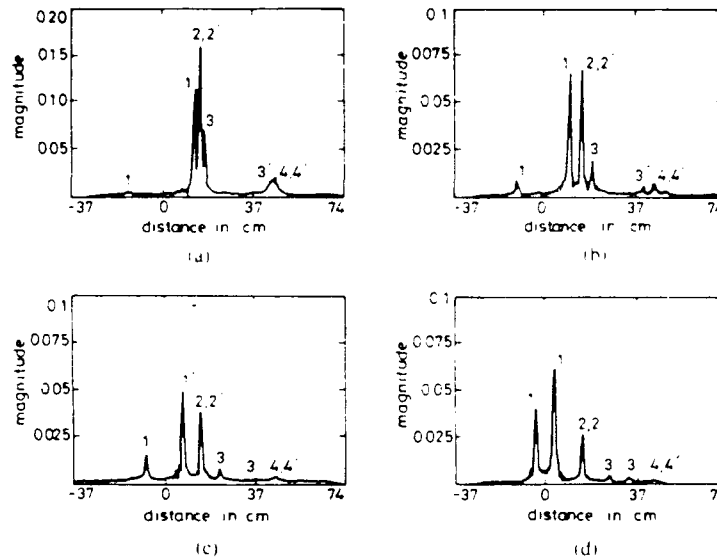
Fig. 1. Straight wire illuminated by impulse.

Fig. 2. Numerical range profiles of straight wire for angles of incidence equal to (a) 30°. (b) 45°. (c) 60°. (d) 75°.

impulsive illumination hits the center point of the wire, is as follows:

$$l_1 = -h \cos \Theta - h \cos \Theta = -2h \cos \Theta$$

$$l'_1 = h \cos \Theta + h \cos \Theta = 2h \cos \Theta$$

$$l_2 = -h \cos \Theta + 2h + h \cos \Theta = 2h$$

$$l'_2 = h \cos \Theta + 2h - h \cos \Theta = 2h$$

$$l_3 = -h \cos \Theta + 4h - h \cos \Theta = 4h - 2h \cos \Theta$$

$$l'_3 = h \cos \Theta + 4h + h \cos \Theta = 4h + 2h \cos \Theta$$

$$l_4 = -h \cos \Theta + 6h + h \cos \Theta = 6h$$

$$l'_4 = h \cos \Theta + 6h - h \cos \Theta = 6h.$$

III. RANGE PROFILES AND RECONSTRUCTED IMAGES

To examine the previous analysis, we use the moment method to theoretically calculate the field scattered from a straight wire scatterer from which we derive the range profiles and reconstruct the image. The piecewise sinusoidal Galerkin method is used [11]. Let the ratio of the length to the radius be 100, the length of wire be 30 cm, and the frequency coverage be from 6 to 16 GHz. In other words, the length in terms of wavelength ranges from 6 to 16. The polarization of the incident field is assumed to be θ-polarized. Shown in Fig. 2 are the magnitudes of the range profiles for angles of incidence

equal to 30°, 45°, 60°, and 75°. The location of the peak marked with *i* corresponds to the differential path length of the *i*th wave motion shown in Fig. 1. If we carefully examine the range profiles shown in Fig. 2, we can find that the peaks marked with 1 and 1´ depart more from the center as the angle θ decreases, while the peaks marked with 2 and 2´ and 4 and 4´ remain at the same position and thus are independent of the angle of incidence. Those peaks marked with 3 move toward 2, while those marked with 3´ move toward 4´ as θ increases. These observations verify the analysis stated in Section II

A real thin rod with length 12″ and diameter 1/8″ is used as a test object to experimentally verify the numerical results. The measurement arrangement is shown in Fig. 3. The wire scatterer is mounted on a rotating pedestal controlled by a microcomputer. A set of step frequencies are transmitted, and the scattered field is received. After that, the object is rotated and the measurement is repeated. The frequency coverage is from 6 to 16.5 GHz. The polarization status of the transmitting and receiving antennas are righthand circularly polarized and lefthand circularly polarized, respectively. A bistatic angle of 16° exists between these two antennas. The range profiles of this thin rod at several aspects are shown in Fig. 4. In this bistatic case the differential path lengths of path 2 and path 2´ are not equal. This fact accounts for the discrepancy between the experimental and numerical range profiles.

From the previous analysis and the range profiles shown in Figs. 3 and 4, one can see that the phenomenon of surface
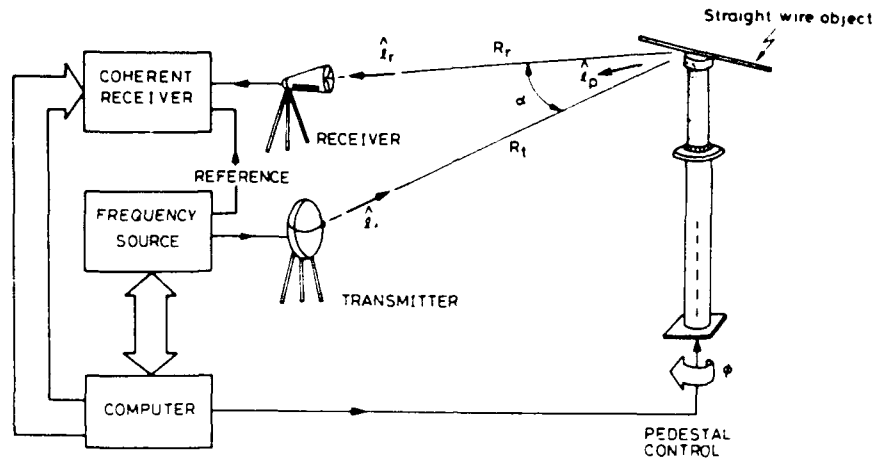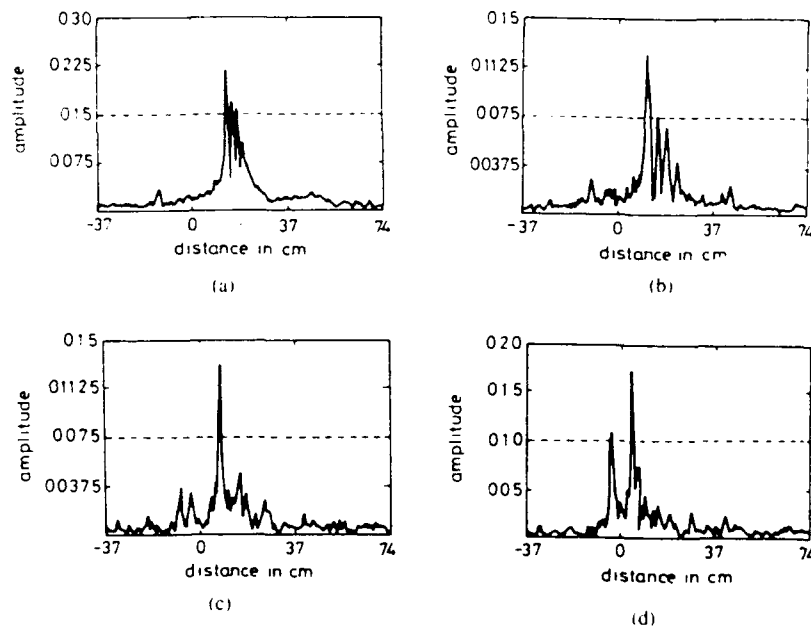
Fig. 3   Block diagram of microwave diversity scattering measurement system.

Fig. 4.   Experimental range profiles of thin rod for angles of incidence equal to (a) 30°. (b) 45°. (c) 60°. (d) 75°.

traveling waves is quite evident in the straight wire case. If the rotation center is chosen at the center point, the effect of constant ranges (2h, 6h, etc.) on the reconstructed image will be rings with constant radius [7]. Shown in Figs. 5(a) and 5(b) are the numerical and experimental images reconstructed from the data collected over an angular window in θ from 20° to 80°, respectively. It is seen that ringlike artifacts appear in the images and the end points are intensified. This example shows that the presence of traveling waves usually degrades the image.

IV. EFFECT OF IMPEDANCE LOADING

The geometry of a loaded straight wire is shown in Fig. 6. If three lumped resistors, each with resistance 50 Ω, are added at $z_1 = 0.5h$, $z_2 = 0$, $z_3 = -0.5h$, these loading points will cause extra reflections. Both the incident wave impinging on the loading points and the waves traveling along the wire arriving at the loading point will cause additional reflections. This fact results in additional peaks in the range profiles.
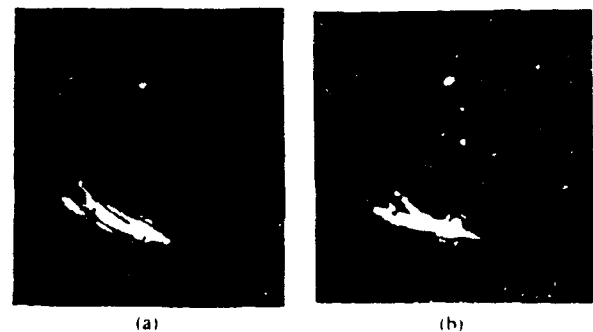
Fig. 5.   (a) Numerical image reconstructed from data collected over angular window from θ = 20° to 80°. (b) Experimental image reconstructed from the data collected over an angular window from θ = 20° to 80°

Shown in Fig. 7 are the range profiles of the three-loading-point wire at several angles of incidence. Examining these plots, one finds that more lobes appear and the lobe produced by the loading point is not as narrow as those produced by the end points. Furthermore, the number of lobes between 1 and
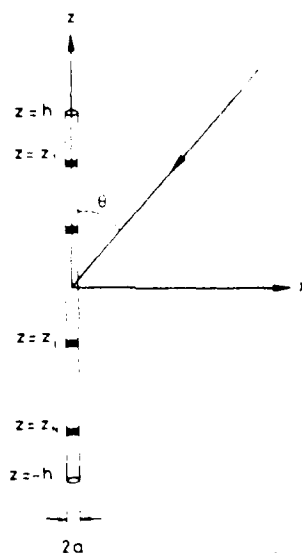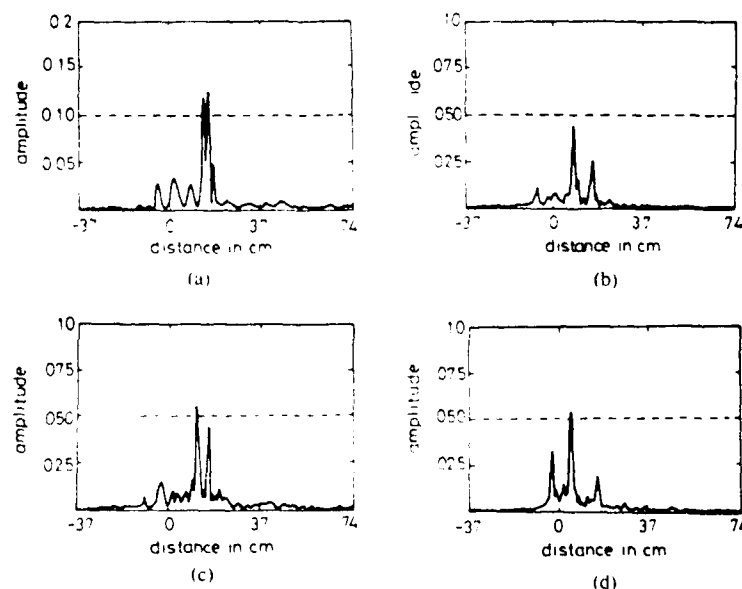
Fig. 6. Geometry of loaded straight wire.

Fig. 7. Numerical range profiles of straight wire with three loading points at angles of incidence equal to (a) 30°. (b) 45°. (c) 60°. (d) 75°

l' is not necessarily equal to the number of loading points (for example, see Fig. 7(b) with $\theta = 45°$). These additional lobes are due to reflections of the traveling waves.

To examine the loading effect experimentally, we divide the thin rod into three sections with a 1-mm gap between them. These gaps are expected to produce a loading effect. However, it is difficult to assign a loading value in each gap. In addition, the equivalent loading impedance is also a function of frequency because the gap distance in terms of wavelength is changed with frequency. The experimental range profiles for several angles of incidence are shown in Fig. 8. Extra peaks appear in the range profiles due to the discontinuities of the gaps. However, the magnitudes of these peaks differ from the counterparts of Fig. 7.

The numerical and experimental images reconstructed from the data collected over an angular window from $\theta = 20°$ to

80° are shown in Figs. 9(a) and 9(b), respectively. It is seen that the loading impedance and the surface traveling waves have distorted the images. By comparing the images of Figs. 9 and 5, one can conclude that the images have been successfully distorted by impedance loading. However, the price paid is an increase in the radar cross section (RCS) [5].

Finally, we examine the effect of time-varying loading on the range profiles. Range profiles usually give the maximum and minimum range information of an object along the direction of propagation, which in turn provide the information of the target dimension. In some applications, it is desired to distort the range profile so that the radar cannot deduce the object dimension from the range profile. One may use an active broad-band slave jammer to distort the range information, but this is not what we wish to discuss. We try to use a passive impedance load to achieve this goal. Impedance
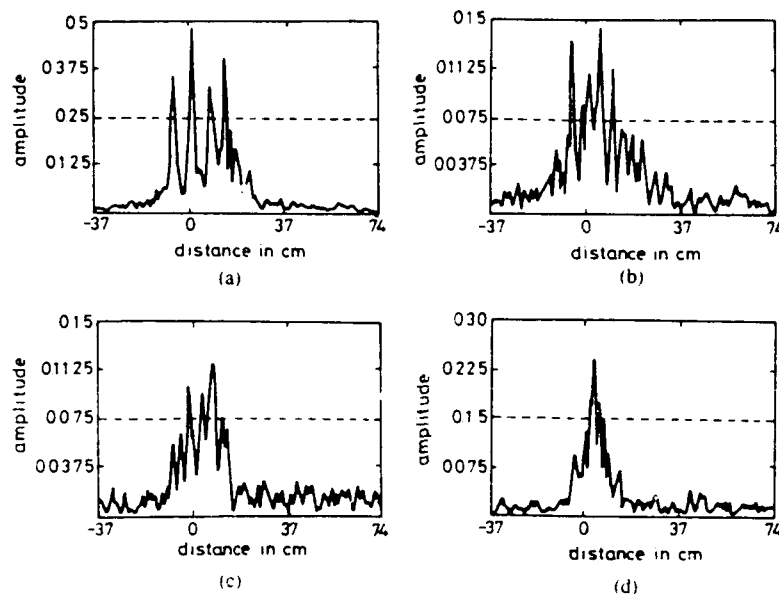
Fig. 8.   Experimental range profiles of three-segment thin rod at angles of incidence equal to (a) 30°. (b) 45°. (c) 60°. (d) 75°.
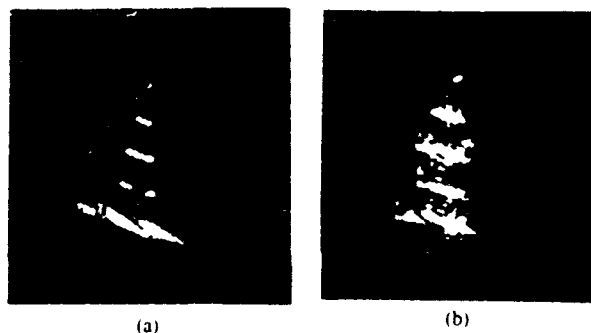

Fig. 9.   (a) Numerical image of straight wire with three loading points reconstructed from data collected over angular window from θ = 20° to 80°. (b) Experimental images of three-segment thin rod reconstructed from data collected over angular window from θ = 20° to 80°.

loading can change the magnitude and phase of the scattered fields. If the loaded values are randomly varied for each time instant, the randomness might cause random peaks in the range profile.

It has been concluded that reactive loading can make a more drastic change in the scattered fields (either in phase or amplitude) than resistive loading can, and increasing the number of loading points can produce greater field variation [5]. It is also known that the reflection coefficient at a given point is a function of the characteristic impedance and the loading impedance at that point. If the loading impedance at a point is randomly switched between capacitive loading and inductive loading, the phase of the reflection coefficient at that point will be changed at each time instant. Consequently, the peak of the range profile at that point may be reduced, and the phase variation of the backscattered field between two adjacent frequencies may be more abrupt. This will increase the effectiveness of the random loading in distorting the range profile.

In the following we compare the effect of a fixed loading, a randomly varied resistive loading, and a randomly varied

reactive loading on the range profiles of a loaded straight wire. The parameters used are number of loading points n equal to 5 and θ = 45°. Each loading impedance is either fixed to 50 Ω, or randomly resistively varied from 0 to 100 Ω, or randomly reactively varied from $-j50$ to $+j50$ Ω. The range profiles of the three loading cases are shown in Figs. 10(a), 10(b), and 10(c), respectively. From the figure one can find that the difference in the range profiles with fixed resistive loading and that with randomly varied resistive loading is small, and randomly varied resistive loading does not create random peaks.

V. CONCLUSION

The scattering mechanism of a straight wire has been qualitatively analyzed. Plots of range profiles at different aspect angles show that surface traveling waves are important scattering mechanisms of a straight wire. The presence of traveling waves makes ringlike artifacts appear in the image of a straight wire. It is also found that lumped impedance loading can effectively distort the range profiles and the reconstructed images. Furthermore, randomly varied reactive loading can

Appendix III

A New Iterative Algorithm for Extrapolation of Data Available in Multiple Restricted Regions with Application to Radar Imaging

H. J. Li
N. H. Farhat
Y. Shen

A New Iterative Algorithm for Extrapolation of Data Available in Multiple Restricted Regions with Application to Radar Imaging

HSUEH-JYH LI, NABIL H. FARHAT, FELLOW, IEEE, AND YUHSYEN SHEN

Abstract—A new iterative method for extrapolation of incomplete segmented data available in multiple separated bands is proposed and tested. The method uses the Burg algorithm to find the linear prediction parameters and an iterative procedure to improve the estimation of the linear prediction parameters and the extrapolation of the data. This method is especially effective when the spectra (Fourier transform of the observed data) are in discrete forms. In the context of radar imaging represented here, this means the objects consist of distinctly spaced scattering centers. The advantages of this algorithm are demonstrated using both numerically generated and realistic experimental data pertaining to high resolution radar imaging.

I. INTRODUCTION

IT IS WELL KNOWN that the resolution of microwave diversity imaging systems [1] depends on the spectral and angular (aspect related) windows. To obtain the range information of the target, one can use a pulsed signal analyzed in the time domain and map the range profile of the target as function of aspect angle or use a broad-band continuous wave (CW) signal analyzed in the frequency domain to yield its frequency response. The range resolution is inversely proportional to the bandwidth coverage of the measurement system. In practical situations, however, due to limitation of the measurement system or restriction of bandwidth allocation, the observed data can lie in multiple restricted spectral regions which we call passbands. Several methods of extrapolating the measured data beyond the observed regions have been proposed and tested [2]-[4] in an attempt to achieve the full resolution of the unrestricted spectral range, when a prior knowledge of the maximum dimension of the object exists and an iterative procedure is applied. The use of linear prediction for the interpolation and extrapolation of missing data and data gaps has also been reported [5].

To increase the resolution obtained from spectral data of such limited extent, techniques of nonlinear power spectrum estimation have been used with notable success [6]. These include autoregression (AR), linear prediction (LP), and maximum entropy method (MEM) and multiple signal classification (MUSIC) algorithm [7]. For a stationary Gaussian

process, the first three methods above can be shown to be equivalent [6].

Most of the nonlinear spectrum estimation techniques are developed to process the data in the time and frequency domains. However, there is an analogy between the time-frequency domain and space-spatial-frequency domain. In microwave diversity imaging, for a given aspect angle, the frequency response of the scattered fields corresponds to a set of time-series data, while the square of the absolute value of the range profile, which is defined as the Fourier transform of the frequency response, corresponds to the power spectrum.

It is known that the linear prediction method is especially suited for those cases when the spectra are in discrete form. Under high-frequency conditions, the scattered field from a complex shaped target can be attributed to a few discrete scattering centers that include edges. It will be shown that under the high frequency approximation the locations of the scattering centers and their scattering strengths are independent of the operating frequency for a given transmitter/receiver pair. This is equivalent to saying that the spectra (or range profiles) of the scatterer are also of discrete form. These phenomena provide the motivation to apply the linear prediction method to microwave diversity imaging.

Although the spectra estimated by MEM or AR can be very sharp and well resolved, this may not be an advantage in a microwave imaging system. If the data are not sampled densely enough in the spectral domain, the sharp, well-resolved components may be missed, and the results may not faithfully reflect the actual spectral amplitudes. Besides, image reconstruction from microwave diversity imaging systems involves coherent superposition of the data in the spectra, or range profiles, of the scatterer (obtained at different aspect angles), where these are estimated from partial data available in segmented bands [1]. If the estimated amplitudes of the range profiles obtained by MEM or AR depart from the desired values because of undersampling, image degradation will result. Furthermore, we are interested not only in the magnitude of the range profile, but also in the phase of the range profiles as required for the coherent superposition. Therefore, to overcome the dense sampling requirement and retain the phase information of the range profiles, it may be preferable to extrapolate the data available in the various passbands into the vacant bands before the spectra or range profile are formed, and image reconstruction is then undertaken.

To extrapolate the data beyond the observed region, an intuitive way is to predict the exterior data by using the same parameters obtained by the linear prediction model. One of the most popular approaches to linear prediction parameters estimation with N data samples is the Burg algorithm [6], [8]. For a given number of data samples in a given observation interval, in order to separate the discrete spectra (in this paper, spectrum is defined as the Fourier transform of the observed data), the required model order in the linear prediction method increases as the separation of spectra decreases, i.e., it is easier to model the data sequence for spectra with larger separation, which translates into well separated scattering centers, than those with closer separation. In addition, for a given model order and given number of sampling points, it is easier to distinguish the two close spectra components (scattering centers) by a data set with longer observation interval than that by a data set with shorter observation interval. It was also suggested that the model order should not exceed half of the number of data points for short data segment because otherwise the linear prediction spectral estimate will exhibit spurious peaks [6]. From the above observations, one can conclude that it would be more difficult to resolve two closer point targets (Fourier transform of the observed data in frequency domain) with short data band. If all the observed data within multiple restricted regions can be fully utilized, better resolution can be expected.

In this paper, a new iterative method which uses the Burg algorithm to find the linear prediction parameters and an iterative procedure to modify the prediction parameters is proposed and tested with both simulated and realistic measured data generated in our anechoic chamber experimental microwave imaging and measurement facilities. With this algorithm, one can obtain acceptable extrapolation beyond the observed region if the spectra are in discrete forms and the separation of the spectra are not too small. Both simulations and experimental results are presented to demonstrate as an example the effectiveness of the method in microwave diversity radar imaging.

II. The New Iterative Algorithm

An approach to linear prediction parameter estimation with N data samples $\{x_1, \cdots, x_N\}$ was introduced by Burg [8]. The linear prediction parameters are obtained by minimizing the sum of the forward and backward prediction error energies ϵ_p,

$$\epsilon_p = \sum_{n=p}^{N-1} |e_{pn}|^2 + \sum_{n=p}^{N-1} |b_{pn}|^2, \qquad (1)$$

subject to the constraint that the prediction parameters satisfy a recursion relationship [5]. e_{pn} is the forward prediction error with model order p and is given by

$$e_{pn} = \sum_{k=0}^{p} a_{pk} x_{n-k}, \qquad (2)$$

and b_{pn} is the backward prediction error with model order p and is given by

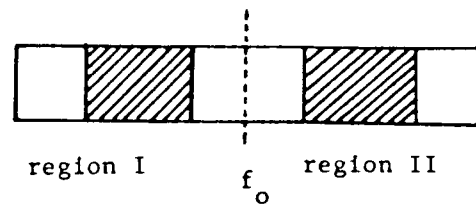$$b_{pn} = \sum_{k=0}^{p} a_{pk}^* x_{n-p+k}. \qquad (3)$$

Fig. 1. Available data in multiple regions. Passband (shaded region) surrounded by vacant bands.

a_{pk} are called linear prediction parameters, and the asterisk denotes the complex conjugate operation.

If one is going to extrapolate from the available data beyond the observed region, a straightforward way is to use the estimated prediction parameters a_{pk} and the measured data by the following equations:

$$\hat{x}_{N+j} = \sum_{k=1}^{p} a_{pk} x_{N+j-k}, \qquad j > 0; \qquad (4)$$

$$\hat{x}_{-j} = \sum_{k=1}^{p} a_{pk}^* x_{-j+k}, \qquad j > 0, \qquad (5)$$

where the caret denotes the estimated value.

If the data available are confined to multiple separate spectral regions or passbands of equal width as illustrated in Fig. 1, and one tries to extrapolate from the observed data to the vacant bands, an intuitive method is to divide the inner vacant band into two parts of equal width and to extrapolate into the left part by using the prediction parameters obtained from the data set of region I and extrapolate into the right part by using the model parameters obtained from the data set of region II.

If the data sequence can be correctly expressed by the prediction parameters, then the extrapolation error, which is defined as the absolute value of the complex difference between the actual values (either computer generated or measured values) and extrapolated values, would be very small. However, if the prediction parameters cannot model the sequence correctly, the error of extrapolation may accumulate. We have found that the linear prediction model which characterizes the data sequence is more accurate for longer data strings and larger model orders, especially in the presence of noise. However, the model order should not exceed half the number of samples because the estimated spectrum will produce spurious peaks [6].

In order to utilize the information available in different regions, a new iterative algorithm using the Burg algorithm to estimate the prediction parameters and an iterative procedure is proposed. The procedure illustrated in Fig. 2 is as follows.

1) Divide the inner vacant band into two parts of equal width. Extrapolate into the left part by using the prediction parameters obtained from the data set of region I and extrapolate into the right part by using the prediction parameters obtained from the data set of region II. If the bands are not equal in width, unequal division of the vacant intervening bands may be appropriate.
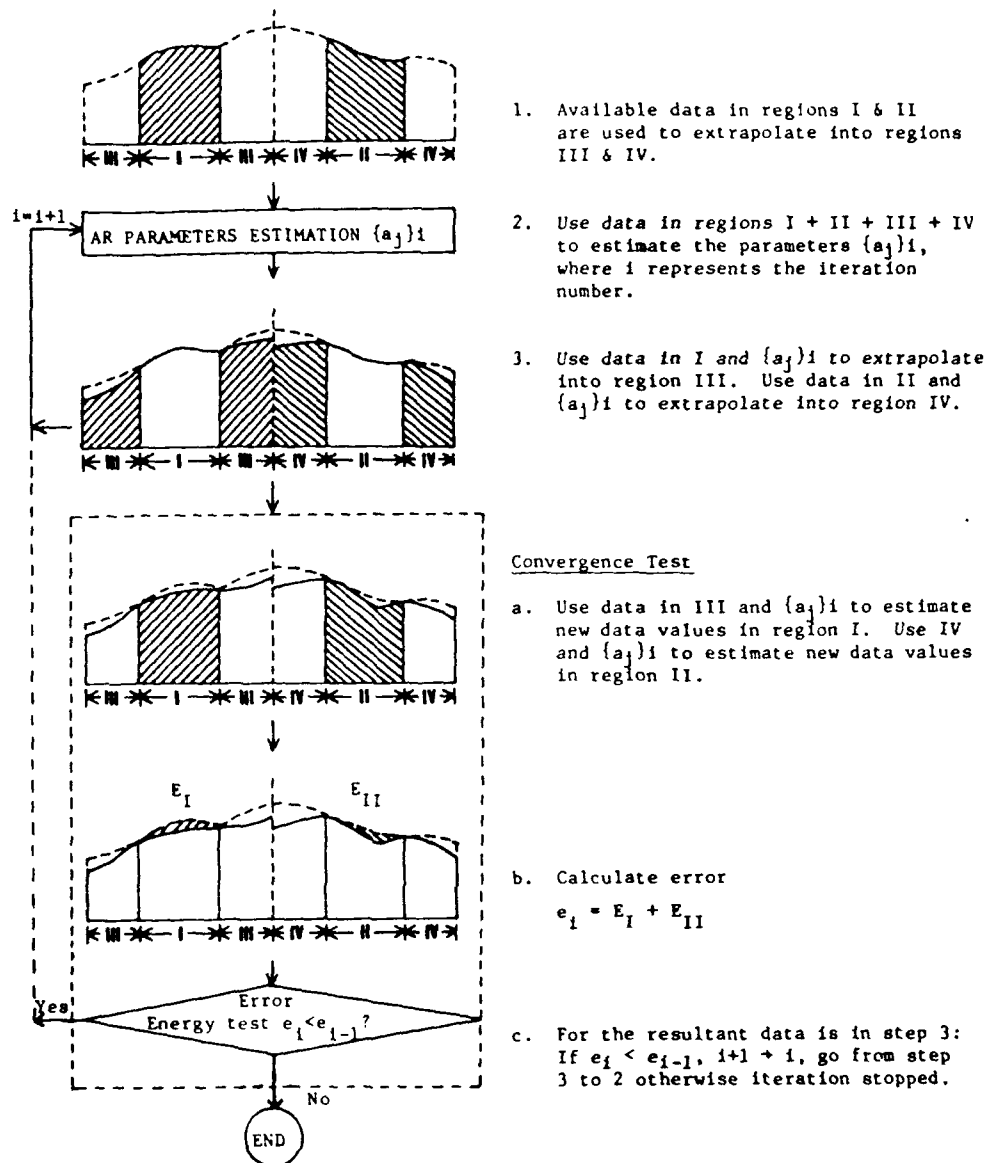
ITERATION ALGORITHM

1. Available data in regions I & II
   are used to extrapolate into regions
   III & IV.

i=i+1   AR PARAMETERS ESTIMATION {a_j}i

2. *Use data in regions* I + II + III + IV
   to estimate the parameters {a_j}i,
   where i represents the iteration
   number.

3. *Use data in* I *and* {a_j}i *to extrapolate*
   into region III. Use data in II and
   {a_j}i to extrapolate into region IV.

Convergence Test

a. Use data in III and {a_j}i to estimate
   new data values in region I. *Use* IV
   and {a_j}i to estimate new data values
   in region II.

b. Calculate error

   $$e_i = E_I + E_{II}$$

c. For the resultant data is in step 3:
   If $e_i < e_{i-1}$, i+1 → i, go from step
   3 to 2 otherwise iteration stopped.

Fig. 2. Schematic diagram of the proposed new iterative extrapolation method.

2) With the vacant bands' data together with the observed data, use the Burg algorithm to find a new set of prediction parameters.

3) Using this set of prediction parameters and the data of region I, extrapolate into the left part of vacant bands, and using the same set of prediction parameters and the data in region II, extrapolate into the right part of the vacant bands.

4) Using this set of parameters together with the extrapolated data, estimate the data in the observation region I and II. Calculate the error energy between the measured data and the estimated data in the observation regions. The error energy is denoted by E_1 and is given by

$$E_1 = \sum_i |x_i - \hat{x}_i|^2 + |x_i - \hat{x}_i'|^2 = \sum_i |e_i|^2 + |b_i|^2, \quad (6)$$

where x_i are the measured data, $\hat{x}_i$ are the forward

estimation of x_i, $\hat{x}_i'$ are the backward estimation of x_i, e_i is the forward prediction error, and b_i is the backward prediction error.

5) With the measured data together with the estimated vacant bands data, use the Burg algorithm to find a new set of prediction parameters. From the measured data and this new set of prediction parameters, extrapolate the vacant bands' data as described in step 3.

6) Use the same procedure of step 4 to calculate the new error energy of the passbands, call it E_2.

7) Compare E_1 with E_2, if E_2 is smaller than E_1, replace the error energy E_1 by E_2, repeat step 5.

8) If E_2 is greater than E_1, stop the iteration, and take the extrapolated data of the previous loop as the final result.

In step 1, if the width of a single band (band I and/or band II) is not large enough, the extrapolation errors produced by

the prediction parameters obtained from single passband data may be very large, in that case, we can set the data in the vacant bands to zero.

The above iterative method can be easily applied to the case where only one single data band is available. The procedures are almost the same except that only one data sequence is used to extrapolate to the exterior bands and to calculate the extrapolation errors.

III. Scattering Properties of a Metallic Object

In this section we shall show that under the high frequency approximation the scattered fields of a metallic object can be expressed as superposition of scattered fields of discrete scattering centers. These phenomena allow us to apply the proposed extrapolation algorithm to radar imaging.

For a metallic object large compared with wavelength, the scattering mechanism can be divided into the following components [9]:

1) specular scattering points;
2) scattering from surface discontinuity: edges, corners, tips etc.;
3) scattering from surface derivative discontinuities;
4) creeping waves;
5) traveling waves;
6) scattering from concave regions;
7) multiple scattering points.

For most situations, the major contributions to the scattered waves are ascribed to the specular scattering points and edge diffractions.

Consider a metallic object seated on a rotated pedestal and illuminated by a plane wave as shown in Fig. 3. The distance between the rotation center O and the transmitter and receiver are R_t and R_r, respectively, and the unit vectors in the directions of transmitter and receiver are $\hat{I}_t$ and $\hat{I}_r$, respectively. Under the physical optics and Born approximations, the vector potential at the receiver under the far-field condition can be expressed as [1]

$$\vec{A}(k, \hat{I}_t, \hat{I}_r) = \frac{jk}{4\pi R_r} e^{-jkR_r} \int_{S_{ill}} 2\hat{n}(\vec{r}')$$

$$\times \vec{H}_0(k) e^{jk[(\hat{I}_r - \hat{I}_t) \cdot \vec{r}']} dS', \quad (7)$$

where k is the wavenumber, S_{ill} the illuminated region, $\hat{n}(\vec{r}')$ the unit normal vector at the surface point $\vec{r}'$, and $\vec{H}_0(k)$ the incident magnetic field at the rotation center. The scattered field is related to the vector potential by

$$\vec{E}_s(k, \hat{I}_t, \hat{I}_r) = j\omega \vec{A}_T(k, \hat{I}_t, \hat{I}_r) \quad (8)$$

where $\vec{A}_T$ is the transverse component of $\vec{A}$ along the direction $\hat{I}_r$.

As k approaches infinity, the asymptotic expression of the above equation can be obtained by applying the stationary phase method [8] to (8). The result is

$$\vec{A}(k, \hat{I}_t, \hat{I}_r) = \frac{jk}{4\pi R_r} e^{-jkR_r} \sum_j \frac{j2\pi}{k \sqrt{S_j}} 2\hat{n}(\vec{r}'_n)$$

$$\times \vec{H}_0(k) e^{jk[(\hat{I}_r - \hat{I}_t) \cdot \vec{r}'_j]} \quad (9)$$
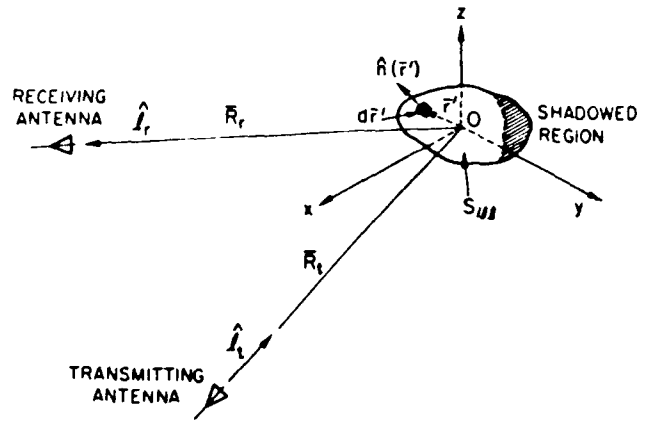

Fig. 3. Geometry of the scattering measurement system.

where $\vec{r}'_j$ are the vectors such that

$$\frac{d[(\hat{I}_r - \hat{I}_t) \cdot \vec{r}']}{da'}\bigg|_{\vec{r}' = \vec{r}_j} = 0, \quad (10)$$

and

$$S_j = \frac{d^2[(\hat{I}_r - \hat{I}_t) \cdot \vec{r}']}{da'^2}\bigg|_{\vec{r}' = \vec{r}_j} \quad (11)$$

where d/da' is the derivative with respect to the surface curvature. The points $\vec{r}'_j$ corresponding to the solutions of (11) are called stationary points or equiphase points or the scattering centers, the term $\hat{n}(\vec{r}'_j) \times \vec{H}_0(k)/\sqrt{S_j} = \vec{a}_j$ is called the scattering strength for the particular scattering center at $\vec{r}'_j$. It is seen that the locations of the scattering centers depend on the directions of $\hat{I}_r$, $\hat{I}_t$ as well as the shape of the metallic surface. The scattering strength depends on the local properties of the scattering centers. The above analysis illustrates that the object function we would be dealing with in high-frequency radar imaging are of discrete form consisting of point scattering centers.

If the received scattered fields have been calibrated with a reference target [1], the corrected vector potential can be expressed as

$$\vec{A}(k, \hat{I}_t, \hat{I}_r) = \sum_j \vec{a}_j e^{jk[(\hat{I}_r - \hat{I}_t) \cdot \vec{r}'_j]}. \quad (12)$$

The Fourier transform of (12) will give the range profile and scattering strength of the scattering centers.

IV. Results

In this section, the performance of the proposed new algorithm using both simulated and realistic data will be evaluated. First, assume for simplicity an object consisting of n point scatterers located at $(r_0 + y_j)$ is illuminated by a plane wave, where r_0 is the distance between the transmitter/receiver and a reference point of the object and y_j is the differential range of the jth scatterer (range relative to r_0). Under far field condition and ignoring multiple scattering, and considering for simplicity a scalarized version of (12), the corrected scalar

field can be expressed as

$$E_s'(k) = \sum_j a_j e^{j2k\gamma_j}. \qquad (13)$$

In the following simulation, the theoretical values of $E_s'(k)$ are calculated in 200 equally spaced frequency steps covering the frequency range $f_1 = 6$ GHz to $f_{200} = 16$ GHz, with an assumed signal to noise ratio set to 40 dB. These values anticipate the realistic experimental data utilized in testing the algorithm.

Assuming the available (computed) data are in the following passband (f_{30}, f_{80}) and (f_{120}, f_{170}). We want to extrapolate the data to the vacant bands (f_1, f_{29}), (f_{81}, f_{129}), and (f_{171}, f_{200}). The range resolution obtained by the discrete Fourier transform (DFT) method using the whole bandwidth (f_1, f_{200}) is about 1.5 cm. The resolution using a single frequency band is about 5.5 cm. The resolution using both frequency bands is about 2.0 cm, however, very high sidelobe levels will be produced. We consider an object consisting of seven point scatterers, the location and scattering strength for each point scatterer are $(r_1 = -30$ cm, $a_1 = 0.5)$, $(r_2 = -20$ cm, $a_2 = 0.5)$, $(r_3 = -10$ cm, $a_3 = 0.5)$, $(r_4 = -2$ cm, $a_4 = 1)$, $(r_5 = 10$ cm, $a_5 = 0.25)$, $(r_6 = 20$ cm, $a_6 = 0.25)$, $(r_7 = -30$ cm, $a_7 = 0.25)$. The values of the field at each sampled frequency f_j are calculated using (13).

Define the extrapolation error at frequency f_j as

$$\epsilon(f_j) = |E_s'(f_j) - \hat{E}_s'(f_j)|, \qquad (14)$$

where $\hat{E}_s'(f_j)$ is the extrapolated value at f_j. The extrapolation errors for different algorithms are compared and shown in Fig. 4(a). The bold solid curve is the amplitude of the theoretically computed fields $E_s'(f_j)$, the thin solid curves are the extrapolation error after 100 iterations using the algorithm proposed in [3], the dashed curves are obtained by using the Burg algorithm to find the prediction parameters from the respective passband, and using this set of parameters together with data in each passband to extrapolate to the outside regions (bands III and IV). The dotted line curves are obtained using this new algorithm with one iteration and with model order 25. The algorithm proposed in [3] basically involves application of the Gerchberg algorithm to data in the multiple restricted regions. However, no numerical or experimental results are given in that paper. It is clear from the results obtained here that the algorithm in [3] seems not to be effective in the case considered as the errors can exceed the amplitude of the theoretical fields. Extrapolation from single passband is not good in this example, because the model order is not sufficient to model the data series in the presence of noise. The proposed new method after one iteration is seen to produce small error.

The Fourier transform (FT) of the all-band data (i.e., data in region I to IV), passband data only, passband plus extrapolated data with the new proposed method are shown in Figs. 4(b)–4(e), respectively. Note that the FT of spectral data yields range profile of the scattering object. It is clear that FT using passband data only (Fig. 4(c)) has very high sidelobe structure, the FT of the extrapolated data using the algorithm in [3] (Fig. 4(e)) is totally different from the original of Fig. 4(b). The result obtained by Fourier transforming the data
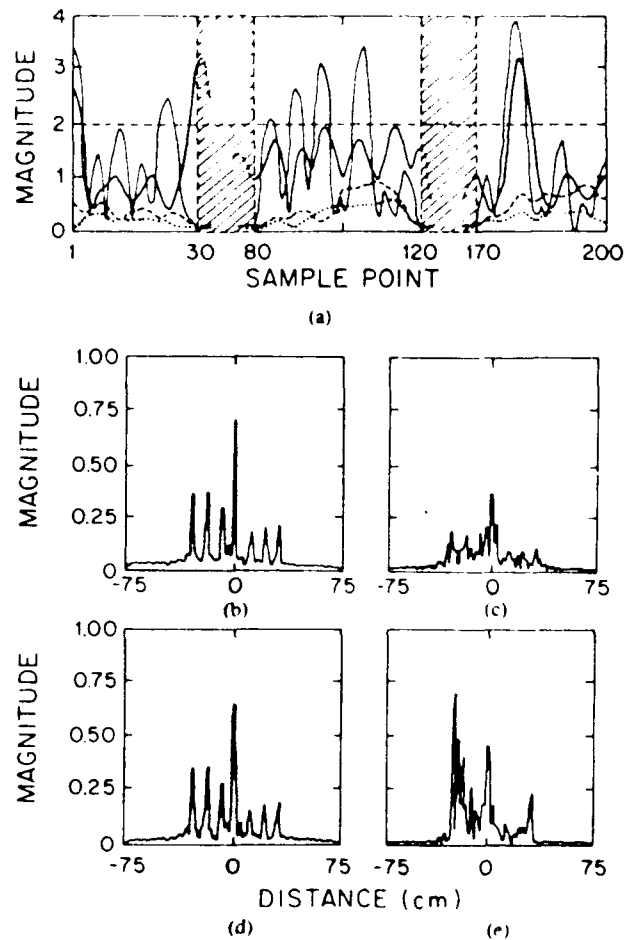

(a)

(b)   (c)

DISTANCE (cm)

(d)   (e)

Fig. 4. (a) Magnitude of theoretical fields and comparison of extrapolation errors of different methods, $f_1 = 6$ GHz, $f_{200} = 16$ GHz. ———: magnitude of theoretical fields; ——: extrapolation error from a single passband, no iteration; .....: extrapolation errors from new iterative algorithm; ··: extrapolation errors from algorithm proposed in [3]. (b) FFT of the whole band data. (c) FFT of the passband data. (d) FFT of the passband and extrapolated data with one iteration. (e) FFT of the passband and extrapolated data using algorithm proposed in [3].

generated by the proposed algorithm is shown in Fig. 4(d) which exhibits excellent agreement with the all-band result of Fig. 4(b). The magnitudes of the peaks in Figs. 4(b) and 4(d) depart from the original assigned values because of zero padding used in the fast Fourier transform (FFT) algorithm. This lack of fidelity in scattering strength reconstruction does not have a discernible degrading effect on the quality of image reconstructed as will be illustrated below, but is important and must be dealt with when quantitative analysis of scattering strengths is needed.

If the frequency coverage is increased to $f_1 = 6$ GHz, $f_{200} = 20$ GHz) with the number of sampling points being fixed to 200 and the passbands are kept at (f_{30}, f_{80}) and (f_{120}, f_{170}), the computed fields and the extrapolation errors would be as shown in Fig. 5. It is seen that the extrapolation error indicated by the dashed line becomes smaller. If the frequency coverage is decreased to $(f_1 = 6$ GHz, $f_{200} = 12$ GHz), the results would be as shown in Fig. 6. It is seen that the extrapolation errors indicated by the dashed and dotted curves are now both high. The FFT of the whole band data, passband data only, and the
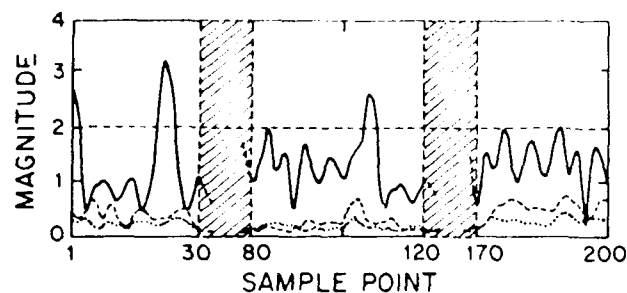
Fig. 5. Magnitude of theoretical fields and comparison of extrapolation errors with and without iteration, $f_1 = 6$ GHZ, $f_{200} = 20$ GHz. ——: magnitude of theoretical fields; ----: extrapolation error from respective passband, no iteration; .....: extrapolation errors from new iterative algorithm.
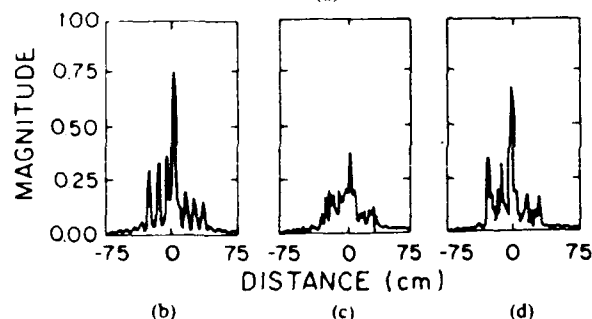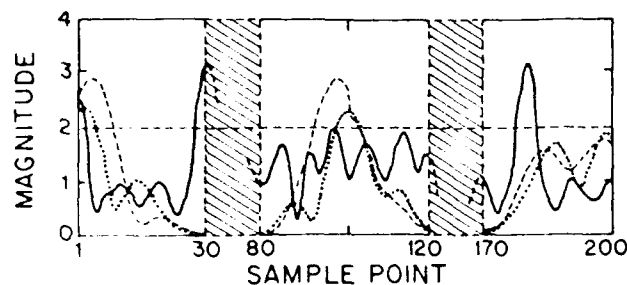

(a)

(b)   (c)   (d)

Fig 6. (a) Magnitude of theoretical fields and comparison of extrapolation errors with and without iteration, $f_1 = 6$ GHz, $f_{200} = 12$ GHz. ——: magnitude of theoretical fields; ----: extrapolation error from respective passband, no iteration; .....: extrapolation errors from new iterative algorithm. (b) FFT of the whole band data. (c) FFT of the passband data. (d) FFT of the passband and extrapolated data with one iteration.

extrapolated plus passband data using this method are shown in Figs. 6(b)–6(d), respectively. The results in Figs. 5 and 6 indicate the desirability of using segmented spectral data spanning wider spectral ranges.

Although the above algorithm is an iterative one, it was found that extrapolation errors usually decrease significantly after the first iteration, and further iterations do not seem to improve the results. Therefore, it is practical and frequently sufficient to use only one iteration.

The performance of the algorithm using realistic data is also evaluated. The test object, a metalized 100:1 scale model of a B-52 aircraft with 79-cm wing span and 68-cm long fuselage was mounted on a computer-controlled elevation-over-azimuth positioner situated in an anechoic chamber environment. Two hundred and one equal frequency steps covering the $f_1 = 6.1$ to $f_{201} = 17.5$ GHz range were used to obtain the frequency response of the object as described in [1]. The target
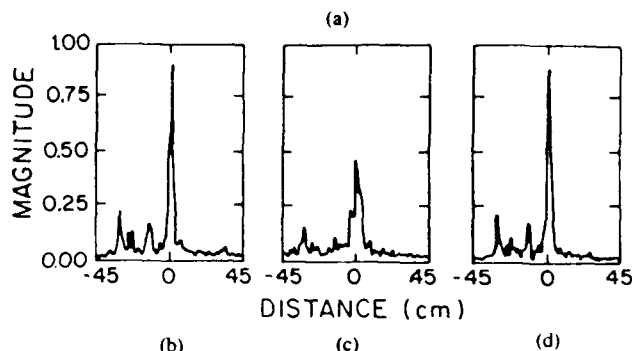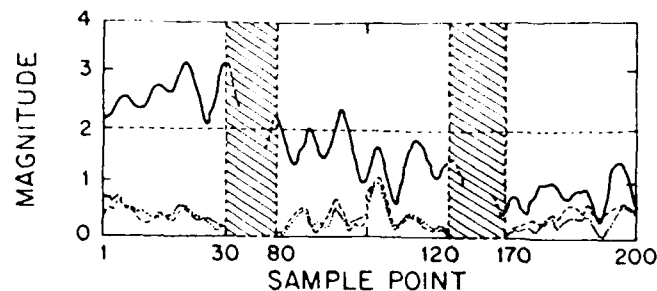

(a)

(b)   (c)   (d)

Fig. 7. (a) Magnitude of the measured fields and comparison of extrapolation errors without and with on iteration. ——: magnitude of theoretical fields; ----: extrapolation error from respective passband, no iteration; .....: extrapolation errors from new iterative algorithm. (b) FFT of the whole band data. (c) FFT of the passband data. (d) FFT of the passband and extrapolated data with one iteration.

is positioned for a fixed elevation angle of 30° while the azimuth angle was altered between 0° and 90° in steps of 0.7° for a total of 128 angular looks.

The passband is first defined as (f_{30}, f_{80}) and (f_{120}, f_{170}). The measured values and the extrapolated errors of the broadside look which is 90° from the head-on look are shown in Fig. 7(a). The solid line curve is the amplitude of the range-phase corrected field (see [1]). The dashed curve represents the extrapolation error resulting from extrapolating from each single band (bands I, II) with model order 25 as described in step 1 of the proposed algorithm. The dotted line curves are obtained using the new algorithm with one iteration and model order 25. The extrapolation error for measurement is defined in a manner similar to the definition of error in numerical simulation as the magnitude of the difference between the corrected measured fields and extrapolated fields. The Fourier transform from the whole band data, the passband data only, and the passband together with extrapolated data are shown in Figs. 7(b), 7(c), and 7(d) respectively. Fourier transform of the corrected scattered fields will give the range profile of the target in that view. In this figure, it is seen that the extrapolation errors do not improve after one iteration. The reason can be explained from the plot of the range profile shown in Fig. 7(b). In this view direction, the major contributions to the scattered fields are due to fuselage and primarily those engines and fuel tank which are on the illuminated side. Specular scattering from these points are well separated in time or distance and their number is small. Hence the linear prediction parameters obtained from single passband are sufficient to model the data sequence. The extrapolation errors are not as small as those obtained by simulations. The reason of this is that the applicability of linear prediction
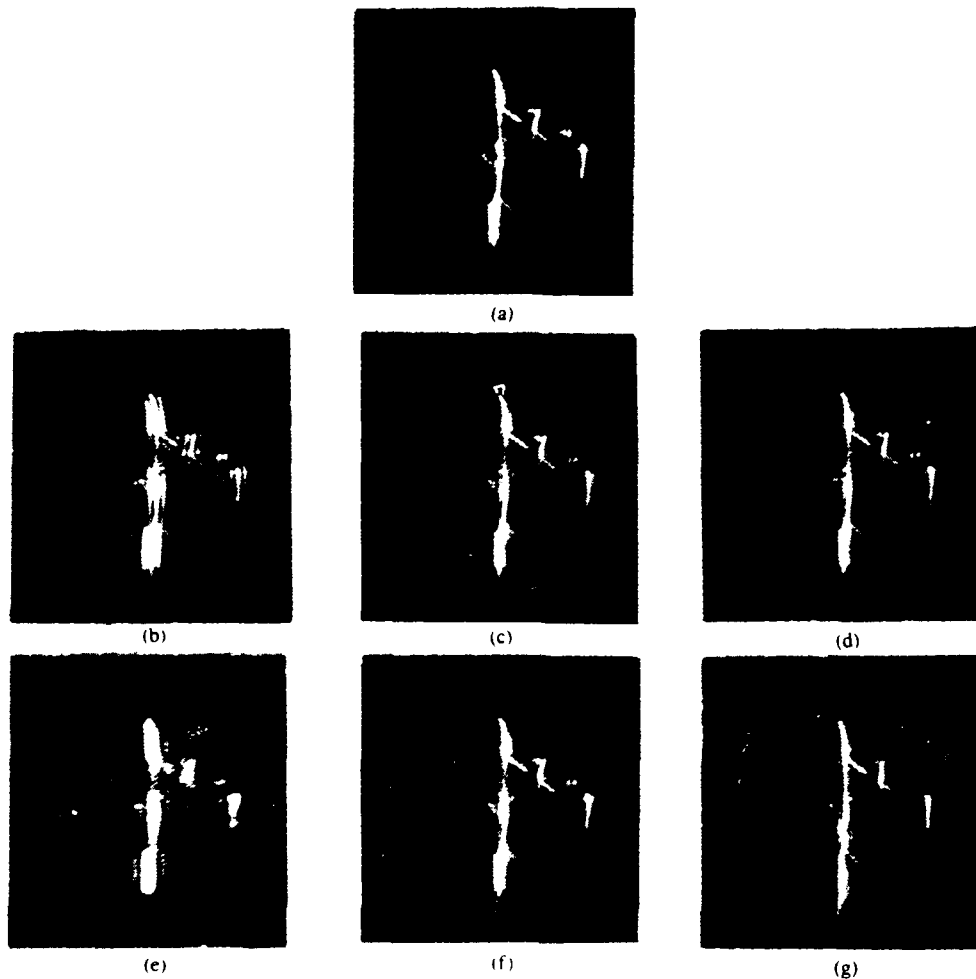
Fig. 8. Reconstructed images of the metalized scale model B-52 aircraft using an angular window 90° extending from head-on to broadside in 128 looks and different spectral coverage. Reconstructions from: (a) Entire bandwidth (f_1, f_{201}). (b) Passband (f_{30}, f_{80}). (f_{120}, f_{170}). (c) Passband (f_{30}, f_{80}), (f_{120}, f_{170}) and extrapolation data (extrapolated data into empty bands) without iteration. (d) Passband (f_{30}, f_{80}), (f_{120}, f_{170}) and extrapolation data with one iteration. (e) Passband (f_{65}, f_{110}). (f) Passband (f_{65}, f_{110}) and extrapolation data without iteration. (g) Passband (f_{65}, f_{110}) and extrapolation data with one iteration.

model to the extrapolation of scattered fields of a metallic object is based on the high-frequency approximation. In the measurement data, however, polarization effects, edge diffraction, multiple scattering and the failure to satisfy the high frequency approximation in the lower region of the frequency band utilized in the measurement will degrade the performance of the algorithm.

The reconstructed images of the test object using data collected in an angular windows of 90° extending from head-on to broadside in 128 looks (see [1] for details) and different frequency bands are shown in Fig. 8. The transmitting antenna is right-hand circularly polarized and the receiving antenna is left-hand circularly polarized, which constitutes by the convention given in [9] a co-polarized transmitting/receiving system. Fig. 8(a) is obtained by using the whole band data; Fig. 8(b) is obtained by using the passband data alone. Fig. 8(c) and 8(d) are obtained by extrapolating without iteration and after one iteration, respectively. The model order used is $M = 25$ in both cases.

If the passband is defined as (f_{65}, f_{110}), the reconstructed images obtained by using the passband data alone and by extrapolation without iteration and after one iteration are shown in Figs. 8(e), 8(f), and 8(g), respectively. The model order used is also $M = 25$.

It is seen that the image quality of Figs. 8(c) and 8(e) are as good as that of Fig. 8(a). These results show the effectiveness of the application of the proposed algorithm to radar imaging from segmented data bands.

V. CONCLUSION

A new method employing the Burg algorithm and an iterative procedure to extrapolate observed data beyond restricted regions of observation has been proposed and tested. Simulation and experimental results prove the effectiveness of this proposed method. The algorithm is especially effective when the spectra of the collected data (the object range profile in this case) are in discrete form. Possible applications of this new method can be found in diverse fields whenever the data is available in restricted bands. For example, in multiple band microwave imaging system, the quality of the image obtained by extrapolating from a much smaller bandwidth can be as good as that obtained by data in the full bandwidth. The cost of the imaging system can hence be reduced drastically as the cost of the required gear can be much lower than the cost of the

gear to cover the full bandwidth and restrictions on use of frequency bands can be accommodated.

REFERENCES

[1] N. H. Farhat, C. L. Werner, and T. H. Chu, "Prospects for three-dimensional projective and tomographic imaging radar networks," *Radio Sci.*, vol. 19, no. 5, pp. 1347-1355, 1984.

[2] R. W. Gerchberg, "Super-resolution through error energy reduction," *Opt. Acta*, vol. 21, no. 9, pp. 708-720, 1974.

[3] Y. Yamakoshi and T. Sato, "Iterative image restoration from data available in multiple restricted regions," *Appl. Opt.*, vol. 21, no. 24, pp. 4473-4480, 1982.

[4] C. Q. Lan, K. K. Xu, and G. Wade, "Limited angle diffraction tomography and its application to planar scanning systems," *IEEE Trans. Sonics Ultrasonics*, vol. SU-32, no. 1, pp. 9-16, 1985.

[5] S. B. Bowling and S. Lai, "The use of linear prediction for the interpolation and extrapolation of missing data and data gaps prior to spectral analysis," in *Proc. RADC Spectrum Estimation Workshop*, Oct. 1979, pp. 39-49.

[6] S. M. Kay and S. L. Marple, "Spectrum analysis—A modern perspective," *Proc. IEEE*, vol. 69, pp. 1380-1419, Nov. 1981.

[7] R. O. Schmidt, "Multiple Emitter Location and Signal Parameter Estimation," in *Proc. RADC Spectrum Estimation Workshop*, Oct. 1979, pp. 243-258.

[8] J. P. Burg, "A new analysis technique for time series data," NATO Advanced Study Institute on Signal Processing with Emphasis on Underwater Acoustics, pp. 12-23, Aug. 1968.

[9] G. T. Ruck et al., *Radar Cross Section Handbook*, G. T. Ruck, Ed. New York: Plenum, 1970, ch. 8.

[10] J. Mathews and R. L. Walker, *Mathematical Methods of Physics*, 2nd ed. Menlo Park, CA: Benjamin, 1970.

Nabil H. Farhat (S'58-M'63-SM'72-F'81) received the B.Sc. degree from the Technion-Israel Institute of Technology, Haifa, Israel, in 1957, the M.Sc. degree from the University of Tennessee, Knoxville, in 1959, and the Ph.D. degree from the University of Pennsylvania, Philadelphia, in 1963, all in electrical engineering.

In 1964 he joined the Faculty of the Moore School of Electrical Engineering, University of Pennsylvania, where he is now a Professor of Electrical Engineering and heads the Electro-Optics and Microwave-Optics Laboratory. His current research interests are in image understanding, microwave imaging and holography, optical information processing and modeling of neural network and self-organizing systems in all of which he has numerous publications. He is teaching courses in EM theory, electro-optics and holography on both graduate and undergraduate levels. His past research included the study of the interaction of EM radiation with plasmas and solids in the context of laser output energy measurement and photodetachment of negative ions. While Associate Professor, he was named to the Ennis Chair in Electrical Engineering. In 1985 he was named Distinguished Visiting Scientist at the Jet Propulsion Laboratory, Pasadena, CA.

Dr. Farhat is a recipient of the University of Pennsylvania Christian R. and Mary F. Lindback Foundation award for distinguished teaching. He is a Fellow of the Institute of Electrical and Electronics Engineers, and the Optical Society of America, and is a member of Sigma Xi, Eta Kappa Nu, the New York Academy of Science, the American Institute of Physics, the American Society for the Advancement of Science, the Franklin Institute and has served on the National Board of Directors of Eta Kappa Nu and has been an RCA consultant since 1969. He has served as Editor of *Advances in Holography* and Associate Editor of *Acoustical Imaging and Holography*. He is currently engaged in the preparation of two texts: *An Introduction to Electro-Optics and Microwave Imaging* and *Holography-Theory and Applications*.

Hsueh-Jyh Li was born in Yun-Lin, Taiwan, Republic of China, on August 11, 1949. He received the B.S.E.E. degree from National Taiwan University, Taipei, Taiwan, in 1971, and the M.S.E.E. from the University of Pennsylvania, Philadelphia, PA, in 1980.

Since 1973, he has been with the Department of Electrical Engineering, National Taiwan University, where he is an Associate Professor. For the period of September 1979-July 1980, he studied at the University of Pennsylvania. Since 1984, he has been a research fellow at the Electro-Optics and Microwave-Optics Laboratory of the University of Pennsylvania and is pursuing the Ph.D degree. His main research interests are in microstrip antennas, microwave imaging and radar cross section reduction.

Yuhsyen Shen was born in Chai-Yi, Taiwan, Republic of China, on October 20, 1954. He received the B.S. degree in telecommunication engineering from National Chiao-Tung University, Hsing-Chu, Taiwan, Republic of China, in 1977.

He had worked for two years as an engineer with Taiwan Telecommunication Administration in Taiwan. During 1981-1982, he was a Teaching Assistant in the Department of Electrical Engineering, University of Pennsylvania, Philadelphia. Since 1982 he has been a Research Fellow at the Electro-Optics and Microwave-Optics Laboratory at the same university. Currently he is a Ph.D candidate in electrical engineering. His research interests include inverse scattering, microwave imaging, digital signal processing, and optical information processing.

Appendix IV

Microwave Diversity Imaging and Automated Target Identification Based on Models of Neural Networks

NABIL H. FARHAT

Microwave Diversity Imaging and Automated Target Identification Based on Models of Neural Networks

NABIL H. FARHAT, FELLOW, IEEE

Invited Paper

Radar targets can be identified by either forming images with sufficient resolution to be recognized by the human observer or by forming signatures or representations of the target for automated machine recognition. Tomographic Microwave Diversity Imaging techniques that combine angular (aspect), spectral, and polarization degrees of freedom have been shown, as summarized in the first part of this paper, to be capable of producing images of the scattering centers of a target with near optical resolution. Despite this capability there are circumstances when the size and/ or cost of the physical aperture needed to furnish angular degrees of freedom is too high, or when the time delay involved in synthesizing such an aperture through relative motion between the radar system and the object being imaged (as, for example, in SAR and ISAR) is not acceptable. One is faced then with the problem of having to identify the target from a limited amount of information that is insufficient to produce an identifiable image. We show that collective nonlinear signal processing based on models of neural networks combined with the use of suitable target signatures (here sinogram representations) offer the promise of robust super-resolved target identification from partial information. Results presented are of numerical simulations for a neuromorphic processor where the neural net performs simultaneously the functions of data storage, processing, and recognition by automatically generating an identifying object label, and fast optoelectronic architectures and hardware implementations are briefly mentioned. Correct identification from as low as 10 percent of the full sinogram representations derived from real data collected in an anechoic chamber environment for three test targets (scale models of B-52, AWAC, and Space Shuttle) and taught to the network is demonstrated. Practical considerations and extensions to real systems are briefly discussed. The neuromorphic approach to target identification introduced here has the promise of obviating the need for large costly apertures that are needed for the imaging of remote targets. It also suggests that nonlinear multidimensional dynamical systems may provide an avenue to the problem of target identification from a single wide-band radar echo.

I. INTRODUCTION

There are two distinct approaches to radar target identification. One is microwave image formation followed by recognition and identification by a human observer, i.e., by the eye-brain system. Here, one is concerned with con-

cepts and methodologies for endowing the images formed with the highest resolution possible to facilitate their reliable identification by human observers. Near-optical resolution and cost effectiveness are usually the objective. The second approach is automated recognition of the target by a machine using suitable target signatures or representations. This approach is called for when we do not have sufficient information about the Radar Cross Section (RCS) of the various parts of the object to be able to define it. Here, one is concerned with issues of correct identification given partial or sketchy information irrespective of range or aspect of the target or its location within the field of view with the help of systems that can do this in robust and fault-tolerant manner. In this second approach, the processing carried out by the eye-brain system in identifying the image in the first approach is to be mimicked by a machine. The motives for automated recognition are varied with speed and cost effectiveness ranking high among them. Both approaches involve amplitude and phase measurements of radar echos from complex-shaped objects as function of orientation, frequency, and polarization using the same gear widely employed in making complex RCS measurements. In the following, the terms identification and recognition will be used interchangably.

In this paper, we discuss both approaches described above and show how they are interrelated and how an understanding of the microwave imaging process and target representation are required for the formulation of methods for automated target identification. We begin in Section II with a qualitative review of the principles and methodologies, of tomographic microwave diversity imaging extensively studied and developed in our laboratory where it is shown that microwave diversity imaging provides 3-D tomographic or projective images of scattering objects with near-optical resolution employing spectral, angular, and polarization degrees of freedom. Because of space limitations, it is not the aim here to dwell at length on the principles and methodologies of microwave diversity imaging which have been adequately described in earlier publications [1]-[8], [11]-[21]. Instead, the discussion here is made intentionally brief but with sufficient detail to

provide the background for ensuing treatment of auto-mated target identification. This is done by bringing out those attributes of microwave diversity imaging that are rel-evant to automated machine recognition. This is followed in Section III by a discussion of a new approach to target identification from incomplete or sketchy information based on models of neural networks. The work is motivated by the desire to further reduce the projected cost of micro-wave diversity imaging systems and by the fact that there exist important circumstances when a real (physical) or syn-thetic baseline for an imaging aperture cannot be formed because of physical constraints in the former or because the time delay associated with aperture synthesis by target motion in the context of Inverse Synthetic Aperture Radar (ISAR) is not acceptable. The aim is therefore to achieve automated recognition from partial information, especially when the amount of information available about the target is so meager that formulation of a recognizable image is out of the question. Our interest in neural signal processing or "brain-like" processing is readily appreciated when one notes the associative memory attributes of the eye-brain system, its amazing ability at supplementing or completing missing information, and the apparent ease and speed with which it solves ill-posed problems of the type encountered in vision, speech, and cognition in general. Neural pro-cessing furnishes a new powerful approach to signal pro-cessing that is both robust and fault tolerant and can be extremely fast when implemented optoelectronically in order to fully exploit the fit between what neural models can offer (powerful collective, nonlinear, and iterative (dynamical) processing) and what optics can offer (paral-lelism and massive interconnectivity) [9], [10]. The discus-sion in Section III includes descriptions of neural-net models and refers to optoelectronic architectures for real-izing content-addressable associative memories that can be useful in radar target recognition. Results representing the performance of software implementation of such neural processors in the recognition of scale models of aerospace targets employing sinogram representations are given. The sinogram representation is chosen as an example of a target representation (feature space or signature space) that is suitable for use with neural processors. Other represen-tations volving low-frequency polarization maps, e.g., plots of the state of polarization of the scattered field as a function of frequency on an inclination angle versus ellip-ticity angle Cartesian coordinate plane, and pole-residue representation [29] of the scattered field, can be equally considered.

Machine recognition with artificial neural networks relies therefore on the generation of target signatures (represen-tations of target features or attributes) that can lead to "dis-tortion tolerant" recognition, i.e., recognition irrespective of target range, orientation, or location within the field of view traditionally referred to as scale, rotation, and shift invariant recognition. The generation of such representa-tions usually involves the same gear employed in micro-wave (μw) and millimeter-wave (mmw) diversity imaging or in performing RCS measurements. In fact, the sinogram representation contains, as will be shown below, exactly the same information contained in a μw/mmw image of the target except that the information is arranged in a different format that is more amenable for use in automated rec-ognition schemes. The work presented here shows that

super-resolved recognition of complex-shaped scattering objects from partial information that can be as low as 20 to 10 percent of the sinogram representation is possible with neural net analog processors employing hetero-associative storage and recall where the outcome is a word label describing the recognized object. The neural net in this sense performs the functions of storage, processing, and recognition (labeling) simultaneously. The work also sug-gests a possible approach to target identification from a sin-gle broad-band radar echo based on nonlinear dynamical system theory and adaptive learning which will be briefly outlined.

II. Microwave Diversity Imaging

In this section, a brief qualitative outline of the principles, methodologies, and capabilities of microwave diversity imaging is presented.

A. Principles

Target-shape estimation in the context of inverse scat-tering from far-field data is a longstanding problem with considerable present-day interest that has been studied by many (see, for example, [2], [3], [11]-[19]). It can be shown from basic electromagnetic scattering theory, assuming that physical optics and Born approximations hold, that monostatic or bistatic measurement of the far field scat-tered by an object as a function of illuminating frequency and object aspect can be used to access the Fourier space $\Gamma(p)$ of the object-scattering $\gamma(r)$. Here, p and r are three-dimensional 3-D position vectors in Fourier space and object space, respectively. The object-scattering function γ can be loosely interpreted to represent the 3-D geomet-rical distribution and strength (RCS) of those scattering cen-ters of the object that contribute to the measured field. The Fourier space-data manifold $\Gamma_m(p)$ measured in practice is necessarily of a finite extent which depends on the values of p realized in the measurement. These depend in turn on geometry and on the angular and spectral windows uti-lized. It is possible then to retrieve a diffraction and noise-limited version γ_d of the object-scattering functions by 3-D Fourier inversion of Γ_m. In particular, tomographic or pro-jective reconstruction of γ_d based on the projection-slice theorem or the Radon transform (see, for example, [16]) have been demonstrated from computed [2], [3], [15], [16] and experimental [5] and [6] data. Image reconstruction using a filtered back-projection algorithm has also been dem-onstrated [20] and shown to yield images with equivalent quality to those obtained by Fourier inversion.

Accessing the Fourier space of a scatterer in practice is not direct. It requires preprocessing of the scattered far field one measures in order to remove an undesirable phase fac-tor due to propagation between the target and the receiver and to remove the effects of clutter and measurement sys-tem response [6]-[8]. The range-phase removal is essential for image reconstruction and is synonomous with syn-thesizing a common phase reference or phase center on the target. It can be interpreted as a Target Derived Reference (TDR) method [21] in which the target itself is made to fur-nish in effect the reference phase for the complex field mea-surements at an observation point. The vector nature of electromagnetic scattering can be treated by assuming that the scattering matrix which characterizes the polarization

properties of the target, and hence provides added information, is measured at every frequency and aspect angle at which the scattering target is observed. A polarization enhanced image can in principle be obtained by incoherent superposition (addition of intensities) of the images formed from the accessed Fourier-space data associated with each of the four components of the scattering matrix. In the work described below, polarization enhancement of the images is achieved by incoherent superposition of images derived from only the copolarized and cross-polarized components of the scattered field.

The above concepts represent the basic principles on which the methodologies of microwave diversity imaging, discussed next, are based.

B. Methodologies

In our work, the Fourier space of a scattering object is accessed using an automated experimental radar scattering and microwave imaging facility (see Fig. 1). The facility enables accessing the Fourier space of scale models of targets of interest placed in an anechoic chamber over extended microwave windows (10 MHz–26.5 GHz), for any state of
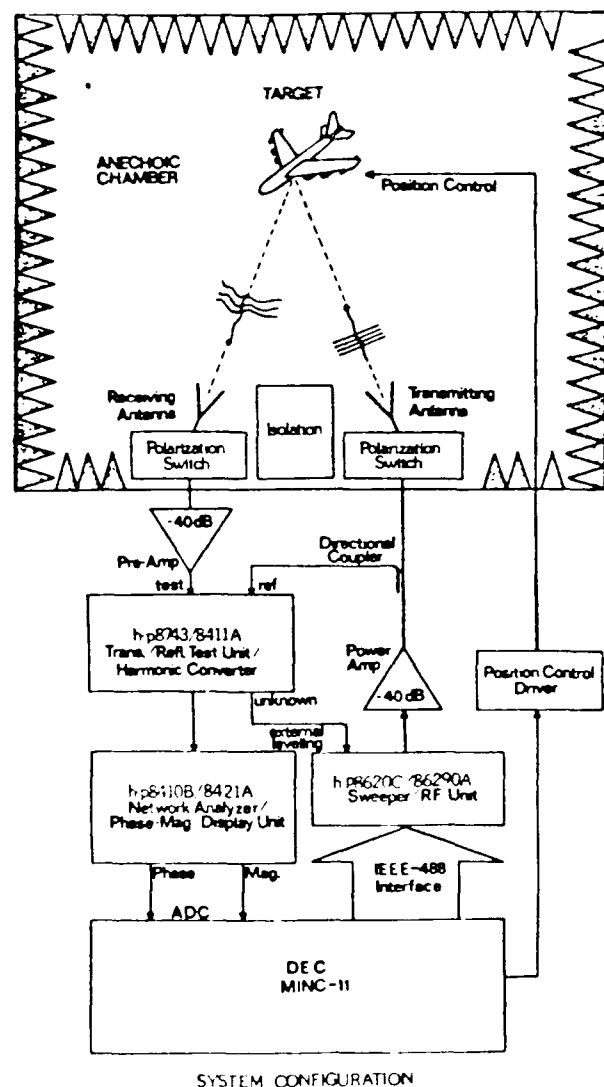

SYSTEM CONFIGURATION

Fig. 1. Experimental microwave measurement and imaging facility

polarization of the transmitting and receiving antennas, and for any aspect or target viewing angle. The instrumentation shown measures the stepped frequency response of the scatterer. Virtually any radar imaging configuration or innovative imaging concept can be readily simulated cost effectively. Inverse synthetic aperture radar (ISAR), spot-light imaging, and array imaging can all be simulated and studied. Also, any illuminating pulse can be synthesized by controlling the amplitude and phase of the CW signals used to illuminate and acquire the stepped frequency response of the target. In the arrangement shown in Fig. 1, the transmitting and receiving antennas are nearly monostatic, but bistatic and multi-static measurements can also be performed. State-of-the-art microwave instrumentation is used to enable making complex scattered field measurements with extremely high accuracy (± 0.1 dB, ± 0.5 degree) over a dynamic range of better than 80 dB. Better accuracy is achieved by averaging several independent readings at each measurement frequency. Frequency can be set automatically with an accuracy of better than 4 Hz and with stability of better than 240 Hz. Results demonstrating the capabilities of the facility in microwave diversity imaging of several representative targets are shown in Figs. 2 and 3. The Fourier slices shown in Fig. 2 consist of polar plots of 128 frequency responses of the test objective corrected for range-phase and system response taken over an angular window of 90° extending in azimuth from head-on to broadside at a fixed elevation angle θ with each view containing 128 frequency points. In these polar plots, frequency is along the radial direction and aspect (azimuth angle) is in the angular direction. Interpolation of the polar formatted data of a slice onto a rectangular grid followed by Fourier inversion yields in accordance to the projection slice theorem [22] a projection image of the scattering centers of the test object. The projection image represents the projection of the scattering centers of the target on a plane normal to the azimuthal axis of rotation (plane parallel to the plane of the Fourier slice). Fourier inversion of the frequency response for a given viewing angle yields the complex impulse response or complex range-profile of the target at that angle. The range-profile resembles the echo or response of the target when subjected to impulsive plane-wave illumination for the given viewing angle. The complex nature of the range-profile is caused by the fact that only positive spectral windows can be employed in practice. By displaying the modulus of the complex range-profiles side by side against the azimuthal angle of rotation ϕ, one obtains the sinogram representation for a given elevation angle θ of the object. Sinograms are discussed further and utilized in Section III.

Fig. 3 shows examples of projection images of two test objects and the process of their enhancement by polarization diversity and symmetrization. Circularly polarized plane-wave illumination was used, and both the co-polarized and cross-polarized components of the scattered field were measured; associated Fourier space slices were formed from which images were obtained. It is evident from the images formed, for the different polarization states, that these contain some complementary information. Therefore, some image enhancement can be expected when the intensities of the co-polarized and cross-polarized images are added as demonstrated by the images in Fig. 3(c). Because manmade objects of interest in imaging radars are invariably symmetrical and their plane or planes of sym-
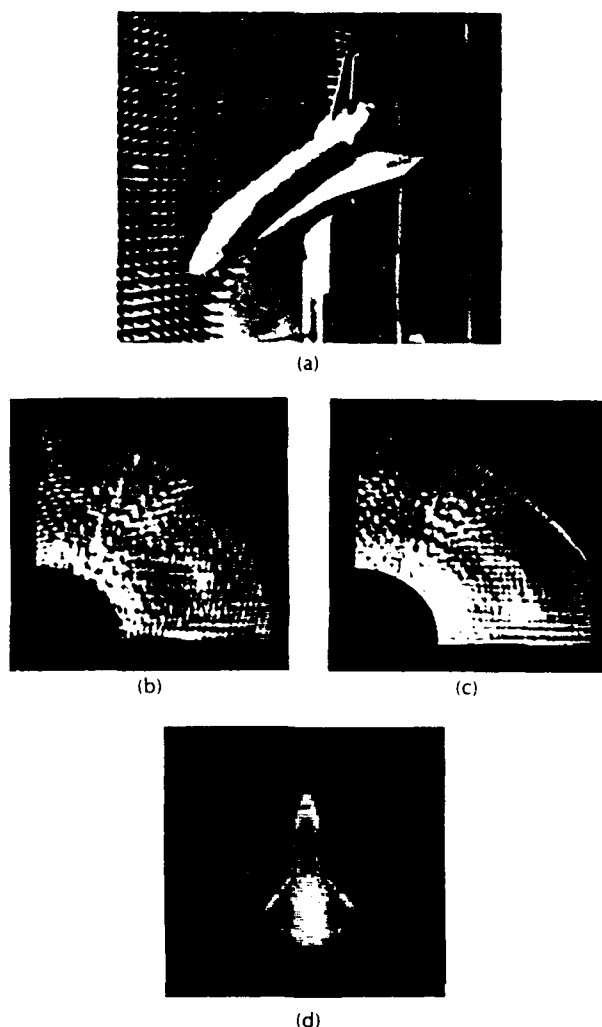
(a)

(b)　　　(c)

(d)

Fig. 2. Results of microwave diversity imaging of a (70:1) scale model of the space shuttle. (a) Object shown mounted on azimuth positioner (turntable) at an inclination angle θ = 30°, magnitude of (b) co-polarized and (c) cross-polarized Fourier space slices taken. (d) Polarization and symmetry-enhanced projection image. (In (b) and (c), radial coordinate represents frequency f and angular coordinate represents azimuthal angle ϕ, (6 $\leq$ f $\leq$ 17) GHz in 128 frequency steps and 0 $\leq$ ϕ $\leq$ 90° in 128 angle increments.)

metry can be inferred from their heading, symmetrization can be used to enhance the image further. As simple a concept as it is, symmetrization is a powerful tool developed in our work to exploit the afinity of the eye-brain system in recognizing symmetric patterns (e.g., ink blots employed in cognitive experiments). In certain instances, poor images that were hardly recognizable became meaningful and recognizable after symmetrization. Symmetrization of the polarization enhanced images in Fig. 3(c) about the vertical line of symmetry running through the fuselage was performed digitally leading to the polarization and symmetry enhanced images shown in Fig. 3(d). The image shown in Fig 2(d) was polarization and symmetry enhanced in the fashion described. Also, all images shown were actually magnified in the vertical direction by a factor $1/\cos\theta$ = 1.155, θ being the inclination angle at which data was acquired, in order to obtain a properly scaled projection image of the scattering centers as they would be seen for example, in a top view of the test object shown in Fig. 2(a). It is seen that
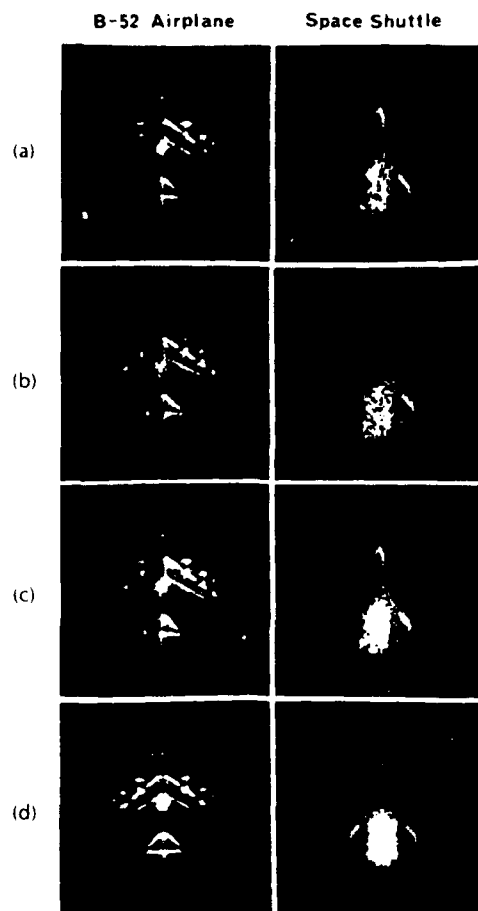
B-52 Airplane　　　Space Shuttle

(a)

(b)

(c)

(d)

Fig. 3. Examples of projection images of two test objects. (a) Co-polarized image. (b) Cross-polarized image. (c) Polarization enhanced image. (d) Symmetry enhanced image.

features of the test objects used are delineated clearly in correct geometrical relation and relative size enabling quick recognition of the scatterer by the eye-brain system. The image resolution achieved is of the order of 2 cm employing a (16-17)-GHz spectral window. It is worth noting that all images are naturally edge enhanced because of the specular nature of microwave scattering from smooth flat surfaces of the objects tested.

The quality and edge-enhanced nature of the microwave diversity images obtained above suggest they are well suited for automated pattern recognition by a machine, especially since the TDR technique results in images that are always centered within the image plane. This may be useful in certain situations. But when a human observer (the ultimate in pattern recognition systems) is available to analyze and recognize the image, the benefits of automated recognition of the image become questionable. Moreover, conventional pattern recognition works best when a good image is available and may falter when the image is incomplete or the amount of available information about the object or the target is insufficient for image formation. Of course, this is exactly the challenge in practice, namely target recognition from sketchy (partial and/or noisy) information which when taken by itself would not be sufficient to form a recognizable image. What is needed therefore is an automated recognition algorithm, of the kind described below, that can identify objects or targets even when the available information is sketchy.

Among its many astounding information processing capabilities, such as robustness and fault tolerance, the brain is also able to recognize objects from partial information. We can recognize a partially obscured or shadowed face of an acquaintance or a mutilated photograph of someone we know with little difficulty, and in reading text we are easily able to fill-in for misspelled or mistyped words. The same is true with understanding spoken language. The brain has a knack for supplementing missing information. Capitalizing on this observation and on our knowledge of neural models and their collective computational properties, a study of "neural processing" for recognizing microwave objects from partial information was undertaken. Details and results are given in the next section.

III. AUTOMATED TARGET RECOGNITION BASED ON MODELS OF NEURAL NETS

Neural-net models and their analogs furnish a new approach to signal processing that is nonlinear collective, robust, and fault tolerant. These models are highly stylized versions of biological neural nets in which neurons act as decision-making elements and the weights of interconnections between them represent the stored information or memory. A neuron receives exitatory and inhibitory inputs from other neurons and decides to fire, sending its own signal in the form of a train of impulses to other neurons, or not to fire, depending on whether or not the sum of the input signals to the neuron exceeds or not a prescribed threshold. The rate of firing (spike frequency) as a function of the sum of inputs and threshold value represents the transfer function or response of the neuron. The transfer function is usually highly nonlinear, making a neural net in essence a nonlinear multidimensional dynamical system with very rich phase-space behavior. A step function response is assumed for the neurons in the treatment here and discrete evolution of the state of the net in time, taken as an iteration number, is adopted. This results in a neural net with binary neurons (neurons firing or not firing). The state vector of such a net consisting of say N neurons, is represented then by a point in the N-dimensional phase-space of the net falling on the vertix of a hypercube and the behavior of the net can be visualized as stepped motion of the state vectors in phase-space over the verticies of the hypercube. The specific phase-space trajectory of a net depends on the weights or connectivity matrix, the neurons response and their threshold level, on initial state of the net, and on any external input signals the neurons receive besides input signals from other neurons. The recipe used below for storing information in the net produces fixed points in phase-space of the net that act as attractors for initial states that fall within their basins of attraction; this operation represents the associative memory or content addressable memory attribute of such networks and their ability to supplement missing information that will be elaborated on below. The dynamical phase-space behavior sketched above is what distinguishes the neural-net processing (neuromorphic processing) paradigm from other approaches to signal processing and is the underlying basis for the new approach to target identification from partial information we present in this and subsequent sections. In this approach, the measured micro-

wave scattering data is placed first in a format suited for neural-net processing before the above associative memory function is activated, as will be detailed later. Optical implementations of neural nets (see, for example, [9] and [10]) are attractive because of the inherent parallelism and massive interconnection capabilities provided by optics, and because of emergent optical technologies that promise high resolution and high-speed programmable spatial light modulators (SLMs) and arrays of bistable optical devices (optical decision making elements) that can facilitate the implementation and study of large networks. Optical implementation of a one-dimensional network of 32 neurons exhibiting robust content-addressability and associative recall has already been demonstrated to illustrate the above advantages [10]. By robust we mean fault tolerance and the ability to correctly recall from partial input data which may also contain errors. By one-dimensional we mean that (in the architecture used there), the neurons are deployed on a line. Two-dimensional arrangements of neurons are also possible and these are of interest because they are suitable for the processing of 2-D image data or 2-D object representations directly as described below, and offer a way for optical implementation of denser networks.

In the remainder of this section, we will discuss content addressable memory (CAM) architectures based on partitioning of the four-dimensional memory or interconnection matrix T_{ijkl} encountered in the storage of 2-D entities. A specific architecture and implementation based on the use of partitioned unipolar binary (u.b.) memory matrix and the use of adaptive thresholding in the feedback loop relevant to the treatment given below have been described elsewhere [23]. The use of u.b. memory masks greatly simplifies optical implementations and facilitates the realization of larger networks (10^3–10^4 neurons). Numerical simulations of the use of such 2-D networks in the recognition of dilute point-like objects similar to those arising in radar and other similar remote sensing imaging applications show that dilute objects pose a problem for CAM storage because of the small Hamming distance between them. The Hamming distance between two binary vectors or matrices of the same dimension is the number of bits in which they differ. We show that coding in the form of a sinogram representation or feature space of the dilute object can remove this limitation and leads to recognition from partial versions of the stored entities. The advantage of this capability in super resolved recognition of radar targets, where the principles and methodologies of microwave diversity imaging described earlier are employed to form sinogram representations that are compatible with 2-D CAM storage and interrogation, are discussed. Super-resolved automated recognition of scale models of three aerospace objects from partial information that can be as low as 10 percent of a learned entity is demonstrated employing hetero-associative storage and recall where the recognition outcome is a word label describing the recognized object. The treatment here is similar to one we have given elsewhere [23].

A. Two-Dimensional Neural Nets

Storage and readout of 2-D entities in a content addressable or associative memory is described next. Given a set of M 2-D bipolar binary $[+1, -1]$ patterns or entities $v_{ij}^{(m)}$, $m = 1, 2, \cdots M$ each of $N \times N$ elements, i.e., $N \times N$ bipolar

binary matrices, these can be stored in a manner that is a direct extension of the outer product storage formula for 1-D entities [31], [9], [10] as follows: For each element of a matrix, a new $N \times N$ matrix is formed by multiplying the value of the element by all elements of the matrix including itself taking the self product as zero. The outcome is a new set of N^2 binary bipolar matrices each of $N \times N$ elements. A formal description of this operation is

$$T_{ijkl}^{(m)} = \begin{cases} v_{ij}^{(m)} v_{kl}^{(m)} & i, j, k, l = 1, 2, \cdots, N \\ 0 & i = k, j = l \end{cases} \tag{1}$$

which is a four-dimensional matrix. An overall or composite synaptic matrix or connectivity memory matrix is formed then by adding all 4-D matrices $T_{ijkl}^{(m)}$, i.e.,

$$T_{ikjl} = \sum_m T_{ijkl}^{(m)}. \tag{2}$$

This symmetric 4-D matrix has elements that range in value between $-M$ to M in steps of two and which assume values of $+1$ and -1 (and zeros for the self-product elements) when the matrix is clipped or thresholded, as is usually preferable for optical implementations [10], [23]. Two-dimensional unipolar binary [0 1] entities $b_{ij}^{(m)}$ are frequently encountered in practice (e.g., binarized images and object representation). These can be transformed into bipolar binary matrices by forming $v_{ij}^{(m)} = (2b_{ij}^{(m)} - 1)$, which are then used to form the 4-D connectivity matrix or memory matrix as described before. Also, as in the 1-D neural-net case, the prompting or initializing entity can be unipolar binary $b_{ij}^{(m)}$, which would simplify further optical implementations in incoherent light [10], [23].

Architectures for optical implementation of 2-D neural nets must contend with the task of realizing a 4-D memory or interconnectivity matrix. Here, a scheme is presented that is based on partitioning the 4-D memory matrix into an array of $N \times N$ 2-D matrices each of which containing $N \times N$ elements. Thus, a 2-D neural net of $N \times N = 32 \times 32$ neurons would contain N^4 interconnections, i.e., over a million interconnections, which shows why hardware implementations that use light and optical interconnections rather than electronic interconnects are attractive. Provided that the number of entities stored is not excessive (see below), the 4-D interconnection matrix thus formed makes the stable states of the net (attractors in phase-space) identical to the entities stored. The maximum number of 2-D entities that can be stored in this fashion without degradation of recall is $M = N^2/8 \ln N$, which follows directly from the storage capacity formula for the 1-D neural-net case [24]. When initiated from a partial version of a given state, the network quickly converges, in a matter of a few iterations (see below) or time constants of the "neuron," to the stored entity closest in the Hamming sense to the initiating vector or matrix. This nearest neighbor search of the memory matrix for a given entity $b_{ij}^{(mo)}$ is done by forming the estimate

$$\hat{b}_{ij}^{(mo)} = \sum_{k,l}^{N} T_{ijkl} b_{kl}^{(mo)} \quad i, j, k, l = 1, 2, \cdots, N \tag{3}$$

followed by thresholding to obtain a new unipolar binary matrix which is used to replace $b_{ij}^{(mo)}$ in (3); the procedure is repeated to obtain a new estimate or state matrix. This process is repeated again and again until the state matrix or "vector" converges to the stored entity closest to the

initializing matrix $b_{ij}^{(mo)}$. This iterative process describes motion of the state "vector" of this 2-D net in its phase-space and can be viewed as a multidimensional, nonlinear, discrete, dynamical system describing the net's evolution from iteration to iteration. Architectures for optoelectronic implementation of the auto-associative storage and recall process described above based on partitioning the 4-D interconnection matrix in an array of $N \times N$ submatrices each of $N \times N$ elements have been described in detail elsewhere [23].

B. Sinogram Representation and Hetero-Associative Storage

Sinograms are object representations encountered in tomography [25], [26]. In simple terms applicable to microwave scattering, the sinogram of a scattering object is a Cartesian plot of the measured relative range or differential range of scattering centers on the object versus aspect angle. A scattering center is defined as any structural detail on the object that contributes to the measured scattered field. In our work, the sinogram of a target is formed by measuring the range-profile or differential range of the target as a function of the aspect angle and fixed elevation angle θ (see Fig. 4(c)) and by arranging the modulus of the measured range-profiles as vertical line intensity patterns side-by-side as function of aspect angle (for example, range-profiles versus azimuthal angle ϕ in Fig. 4(c) at fixed elevation angle θ). Sinogram construction is illustrated in Fig. 4 for a planar object consisting of three points of unequal

SINOGRAM GENERATION — PRINCIPLE

SINOGRAM GENERATION — EXPERIMENTAL

Fig. 4. Sinogram representation. (a) Scattering geometry for an idealized planar object. (b) Sinogram. (c) Simplified arrangement for experimental generation of sinogram.

strength. This object is chosen to represent a highly simplified radar target. Every point (or scattering center) of the object generates a sinusoidal trace in the sinogram whose amplitude is determined by the radial distance of that point from the center of rotation, whose phase is determined by the angular position of that point, and whose brightness or strength (represented in Fig. 4(b) by line thickness) is proportional to the strength of the scattering center. Note that scatterer 3, whose position coincides with the center of rotation, produced a zero amplitude line in the sinogram. A complete sinogram is produced by rotating the object 360°. It is worth noting that the range-profile of an object is independent of its far-field distance from the transmitter/receiver (T/R) in Fig. 4(a) or Fig. 4(c). The range-profile depends, however, on object aspect and on the spectral window and polarization used in data acquisition (see Section II-B).

Sinograms are particularly useful when the object is point-like and sparse or dilute, as is the case in microwave diversity imaging where the images formed consist ordinarily of a finite number of isolated scattering centers. Given a set of 2-D dilute objects (each consisting of a collection of a finite number of distinct point scatterers) and their corresponding set of associated sinogram representations, the Hamming distances between the sinogram representations will always be found to be greater than the Hamming distances between the objects themselves. This is assuming that objects and sinograms are quantized onto the same number and grid of binary pixels. The reason for this is that each point of the object produces a distinct sinusoidal trace and thus spawns many points in the sinogram representation. Therefore, if (for example) two dilute objects differ in only two pixels, their sinogram representation will differ by two sinusoidal traces and, hence, in many pixels. The increased Hamming distance makes it easier for an associative memory to distinguish between the sinograms than to distinguish between the objects themselves. This has the added attraction of making it less difficult to distinguish between similar objects, that is, objects with small Hamming distances between them. Sinogram representations also have the advantage of being useful, as will be clarified

below, in achieving distortion invariant (scale, rotation, and translation invariant) recognition.

In laboratory work, the sinogram representation of a complex-shaped test object is obtained as depicted in Fig. 4(c), which is a highly simplified version of the measurement system of Fig. 1. The number of range-profiles N_o needed to characterize the object and the number of samples N_R within each range-profile are determined by angular and spectral sampling considerations. Thus, for an object with maximum extent L, the maximum number of angular samples in one azimuthal direction is $N_o \approx 4\pi L/\lambda_{min}$, and the maximum number of samples N_R within a range-profile is $N_R = N_f = 2\Delta f L/c$, where Δf is the width of the spectral window used, N_f is the number of frequency points, c is the velocity of light, and λ_{min} is the shortest wavelength used. The sinogram of an actual microwave target differs in appearance from the sinogram of the idealized object described above in that the intensity or brightness of its sinusoidal traces changes (fades in and out) with the aspect or viewing angle because of the anisotropic nature of the scattering centers on actual targets. Fig. 5 gives an example of the sinogram of a scale model of a B-52 test object produced from a slice of its Fourier space (shown in Fig. 5(a)) obtained at an object inclination angle of $\theta = 30$ (see Fig. 4(c)) employing the measurement facility of Fig. 1. Both intensity and 3-D perspective displays of the resulting sinogram are shown in Fig. 5(b) and (c), respectively. The sinogram shown demonstrates clearly how sinusoidal traces of the different scattering centers fade in and out as a function of target aspect (here azimuth angle ϕ) and how point-like scattering centers such as the tips of engines and fuel tanks (see the B-52 part of Fig. 3(d)) produce more distinct traces than edge-like or extended scattering centers of the target. Thus, the sinogram pattern tends to characterize the target by its dominant point-like scattering centers that are visible over an extended range of aspect angles. The sinogram pattern is a map of the measured relative positions between such centers as the target is rotated about a specified axis. Complete sinogram representation of a 3-D target involves sinogram maps such as the one shown in Fig. 5 for all elevation angles θ of expected encounter. The range of
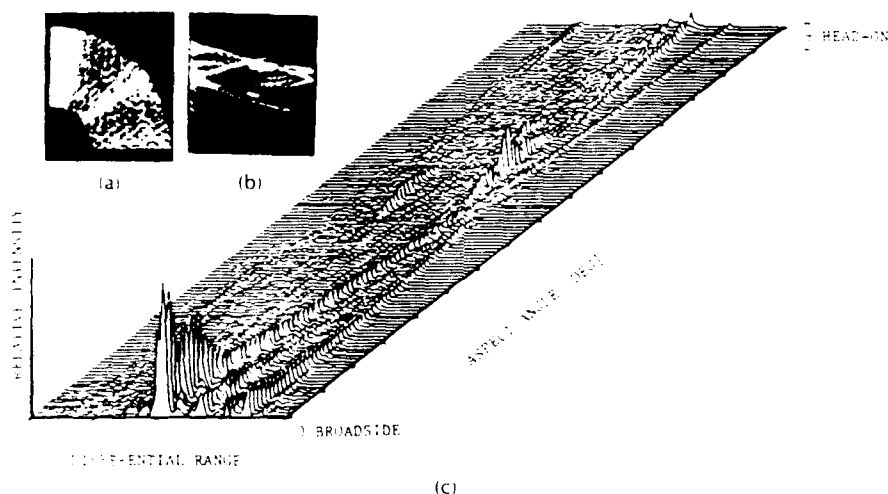

(a)   (b)

(c)

Fig. 5. Sinogram of a 100:1 scale model of a B-52 test object. (a) Fourier space slice from which the sinogram is generated (b) Intensity display and (c) 3-D perspective display of the sinogram. Note "broadside" and "head on" are specified for inclination angle of $\theta = 30°$.

azimuth angles ϕ needed would be confined to those indicated by practical encounter scenarios.

It is worth mentioning that the alignment of the range-profiles to produce distinct sinusoidal traces in the range-aspect displays (Fig. 5(b) and (c)) is an essential requirement for image reconstruction by back-projection [20]. The alignment process also defines the center of rotation or phase center of the target, in that had a point scatterer been located at the rotation center, it would produce a straight line at constant range in the sinogram. The alignment is also equivalent to the TDR procedure referred to in Section II-A and described in more detail elsewhere [8], [21]. Thus, formation of a distinct sinogram is not only needed for representing the target but it also an essential step for removing the unknown range to the phase center of the target and the removal of undesirable effects associated with migration of its phase center with aspect. The crispness with which one or more sinusoidal traces appear in the sinogram in this alignment process can serve as a measure of how well the unknown range to a common reference point (center of rotation or phase center of the target) can be compensated for in the different aspect looks at the target. Quantization and thresholding of the sinogram pattern of Fig. 5 into a grid of $N \times N$ binary pixels yields the sinogram representation b_{ij} of the target that is suitable for the associative storage and recall process described in Section III-A. In the top row of Fig. 6 are shown the sinogram represen-
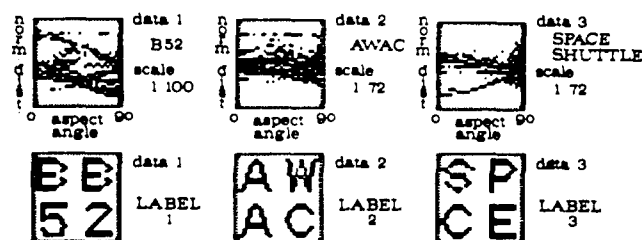

Fig. 6. Hetero-associative storage. Sinogram representations (top) and associated word labels (bottom) of three aerospace test objects.

tations of scale models of three aerospace test objects (B-52, AWAC, and Space Shuttle) interpolated and digitized onto a grid of 32×32 binary pixels. These are treated as a learning set and stored hetero-associatively rather than auto-associatively by replacing $v_{kl}^{(m)}$ in (1) by $r_{kl}^{(m)}$, where k, $l = 1, 2, \cdots, 32; m = 1, 2, 3,$ and where $r_{kl}^{(m)}$ are bipolar binary versions of the abbreviated word labels shown in the bottom row of Fig. 6 with which the three test objects are to be associated. In this fashion, a nonsymmetric 4-D hetero-associative memory or connectivity matrix T_{ijkl} is formed in which the associations between the three sinogram representations and their word labels are embedded. The connectivity matrix is used in the numerical simulations described next.

IV. RESULTS

Numerical simulations of interrogating the hetero-associatively formed memory matrix with complete and partial versions of the three entities (sinogram representations) stored in it following the procedures of Section III-A were carried out. Complete and partial versions of the three

stored sinogram representations were used to initialize the network. The partial versions of the stored entities ranged down to a fraction $\eta = 10$ percent of the full representation. Here, η is the ratio of the number of range-profiles entered to the total number of range profiles used to characterize the object in its sinogram representation. Reliable identification of the partial sinogram input was found to occur after one iteration for all entities stored down to $\eta = 0.2$ confirming convergence to a stable state even when the T_{ijkl} matrix is not symmetrical, as is usually required for convergence [31]. This, and the observed speed of convergence, may indicate a difference in the behavior of 2-D nets and their 1-D counterparts whose reason is yet to be determined. For $\eta = 0.1$ or less, successful recall of correct labels was found to depend on the angular location of the partial data with which the memory is presented. In most cases of $\eta = 0.1$, the net labeled the partial initializing input correctly, as illustrated in the AWAC example of Fig. 7, and in those cases when it did not do so, it produced a garbled and/or contrast-reversed version of a label that resembled one of the other labels (see the B-52 examples in Fig. 7). Below $\eta = 0.1$, the reliability of recall deteriorates rapidly. However, in nearly all simulations with partial input, failure of the net to label the entry correctly was manifested by convergence onto a garbled and/or contrast-reversed version of one of the identifying labels. This behavior could be usefully interpreted as the net indicating it has insufficient information and that more information is needed before a decision (identification) can be made and that otherwise no decision should be made.

Rapid "one-shot" convergence to correct association exhibited above even with small values of η means, in the language of dynamical systems, that the fixed point-attractors (stored associations) in the phase-space of the net are strong and they possess large basins of attractions.

The results above illustrate the potential of neuromorphic processing in object identification from partial sinogram information (object representation). What is noteworthy is that the net in those simulations performed the functions of storage, processing, and labeling simultaneously, which is the hallmark of distributed collective processing. The performance of such nets is also known from other work to be robust and fault tolerant. In an actual hardware implementation of a prototype neural net of 32 neurons, correct associative recall from partial information continued to take place even when nearly 20 percent of the neurons were disabled [10]. The binary nature of the sinogram representation resulting from interpolation and thresholding the raw sinogram data (e.g., of Fig. 5(a)) is expected to impart to it some immunity to noise present in the measured data. To apply the method in practice, several issues related to the generation of sinogram libraries and to the ability to determine the aspect angles for which data is collected must be considered. These are briefly addressed in the following section.

V. DISCUSSION

Methodologies of microwave diversity imaging studied extensively at the Electro-Optics and Microwave Optics Laboratory of the University of Pennsylvania for more than two decades provide the basis for a new generation of 3-D tomographic imaging radars that can furnish shape esti-
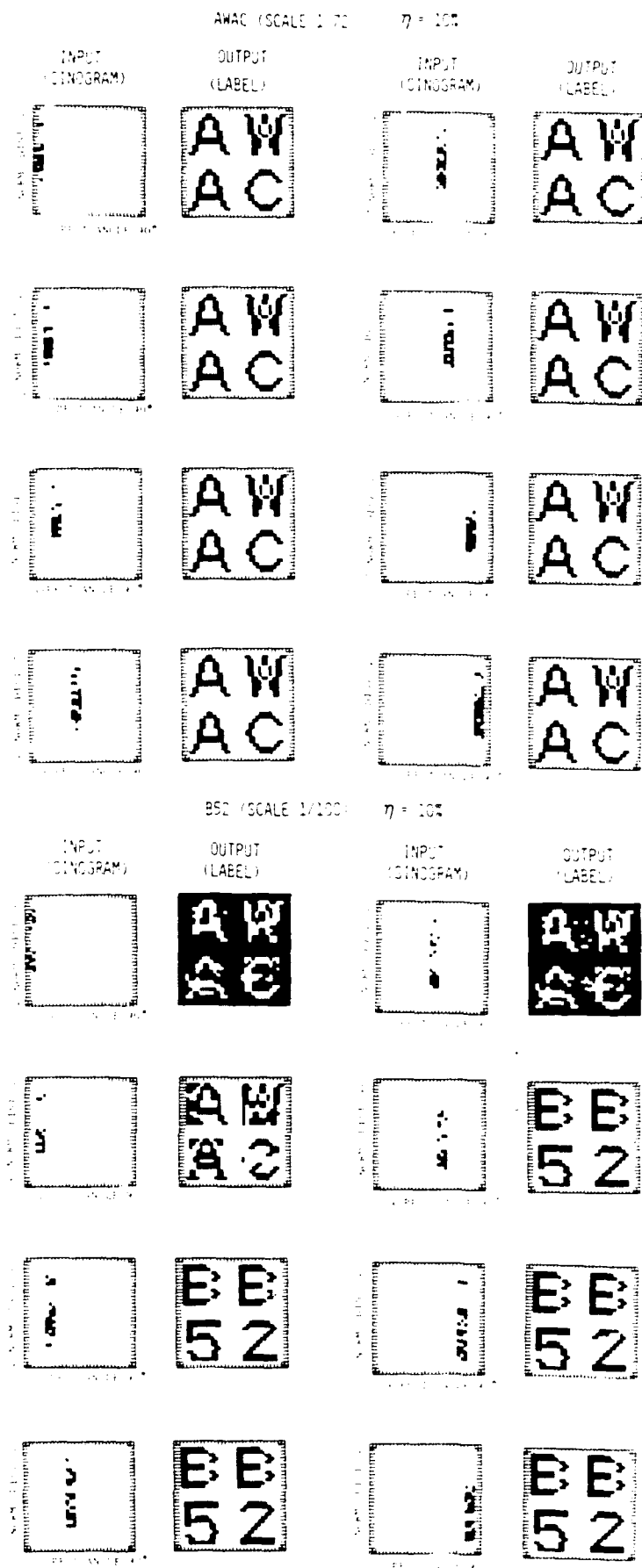
Fig. 7. Effect of position of angular window on reliability of recall when the net is initialized with partial sinogram data ($\eta = 0.1$)

678

PROCEEDINGS OF THE IEEE, VOL. 77, NO. 5, MAY 1989

mates of the 3-D distribution of scattering centers on remote aerospace targets with near-optical resolution. Arrays of broad-band coherent transmitter-receiver pairs employing the TDR technique can be used to access the Fourier space of remote scattering targets. Resolution in such systems depends on the angular and spectral windows, utilized for data acquisition and on polarization diversity. Unprecedented centimeter resolution has been demonstrated in projection rather than 3-D images of scale models of such targets employing gigahertz spectral windows, wide angular windows of $\pi/2$ [Rad.], and image enhancement by polarization diversity and symmetrization. Image-reconstruction algorithms based on Fourier inversion or by filtered backprojection are equally applicable and have been found to yield comparable results. The use of spectral, angular, and polarization degrees of freedom in such imaging systems has the advantage of increasing the information content of the object-scattered wavefields. This enbles a broadband, polarization-selective array aperture to acquire more information about a scattering object than it could have monochromatically (at a single frequency) or at a single polarization. A useful tradeoff between spectral and angular degrees of freedom exists. It enables considerable thinning of the imaging array. Because angular degrees of freedom are associated with the number of elements or stations in the array, their replacement with less costly spectral degrees of freedom, associated with the number of frequency points used in data acquisition, can cut cost and lead to significant improvement in cost effectiveness.

Despite these attractive attributes of microwave diversity imaging systems, there are circumstances when the baseline (physical or synthetic) required to realize the wide angular windows needed to achieve high resolution is not available or is not sufficient to form a recognizable image. One has to rely then on means of target identification other than image formation and analysis by the eye-brain system.

The "neuromorphic" or "brain-like" processing approach to super-resolved, robust, and fault tolerant recognition described in the preceding section is not only intellectually attractive, providing for the first time a connection between neural nets and applied electromagnetics, but could also obviate the need for large expensive imaging array systems (of the type needed in microwave diversity imaging systems and other more conventional approaches to radar target imaging) and can avoid the time spent for aperture synthesis for example by target motion in ISAR imaging. The implication of this for microwave (and other) automated object-identification systems can be far reaching and is sufficient motivation to search for a new generation of automated neuromorphic radar and sonar recognition systems, that can identify remote targets from only a few looks [27]. Many of the findings of the work reported here also carry over to the domain of machine vision and recognition for robotic applications. The problem then is however more complex because objects of interest are not found in perfect isolation as is the case in recognizing aerospace targets. In the radar-target identification scenario, suitable target representations (signatures or feature spaces) such as the sinogram representation described above would be generated cost effectively from scale models of targets of interest in a controlled anechoic chamber environment employing measurement systems, of the type we have described. The representations would be

"taught" to an associative memory or a neural network that can be used to recognize partial sinogram representations of actual targets collected by actual broad-band coherent radar systems. Realization of this scenario entails careful consideration to scaling issues and to the principles of "electromagnetic similitude" [28] in order to ensure that the sinogram representations collected using scale models in an anechoic chamber RCS measurement facility resemble as closely as possible those of the actual targets. This and other issues such as "fluctuations" of echos from actual airborne targets because of flexing, deformation, or wind-buffeting, the minimum number of looks (range-profiles) needed to represent an actual target i.e., characterize it for all practical encounter aspects; the number and size of neural models needed for the identification of a given number of targets, together with the use of sequential storage and recall, and the self-organization and learning capabilties of neural nets must be addressed before the neuromorphic approach to target identification can find practical application. The latter capabilities have the potential of producing improved neuromorphic target recognition schemes that can learn the underlying structure of the associations presented to them with generalization (i.e., non-rote learning) [30]. These issues and others are currently under investigation [32]. The ultimate aim of this work is to achieve reliable distortion independent recognition from one look. In this regard, we offer the following final remarks. Because for fixed spectral window, the range profile of a target is basically independent of range and depends only on target aspect, the prospect of achieving recognition from a single look (single range-profile) would mean complete distortion-independent identification, that is, recognition independent of target range or aspect. How can this be done? One can conceive of the following approach or scenario that is being considered in our work, [33], as a direct extension of the ideas given in this paper. In this approach, one seeks neural-net structures and storage recipes that can produce prescribed controlled periodic attractors. Periodic attractors are represented by closed trajectories in phase-space. Thus, we envision a net in which we can specify and obtain the next state of the net given the present state in a closed or open sequence of states to enable storage and recall of prescribed sequences of state vectors instead of the "fixed point" phase-space attractors encountered in the above hetero-associative storage and recall work. Each periodic attractor in the envisioned net would consist of a sequence of state vectors, representing, for example, thresholded versions of angularly adjacent range-profiles of a target, with each sequence containing an extra lable vector inserted to identify the target associated with that sequence or periodic attractor. A periodic attractor of the net associated with a given target, would be triggered when the net is initiated by either an initial state that coincides with one of the constituent thresholded range-profiles of that attractor or by an initial state that is sufficiently close to any one of the constituent range-profiles in the Hamming sense. No matter which thresholded range-profile is used to initiate it, the net would eventually end up cycling through the associated periodic attractor and, hence, through all other associated range-profiles, including the label state vector whose occurrence we assume can be isolated and used to trigger an identification marker of the target, thus identifying it from the single available ini-

tializing range-profile data. Although in its early stages of development, the above "phase-space engineering" concept and possible scenario for automated target identification from a single wideband radio echo helps one appreciate of the unique possibilities and power of the neural paradigm and the collective nonlinear dynamical system theory approach to signal processing.

REFERENCES

[1] N. H. Farhat, "Principles of broad-band coherent imaging," *J. Opt. Soc. Amer.*, vol. 67, pp. 1015-1020, Aug. 1977.
[2] N. H. Farhat and C. K. Chan, "Three-dimensional imaging by wave-vector diversity," *Acoust. Imaging, vol. 8, Proc. 1978 Int. Symp. Acoust. Imaging*, A. Metherell, ed., pp. 499-515, Plenum Press, 1980.
[3] C. K. Chan and N. H. Farhat, "Frequency swept imaging of three dimensional perfectly reflecting objects," *IEEE Trans. Antennas Propagat.*—Special Issues on Inverse Scattering, vol. AP-29, pp. 312-319, Mar. 1981.
[4] N. H. Farhat, "Holography, wavelength diversity and inverse scattering," in *Optics in Four Dimensions-1980, M. A. Machado and L. M. Narducci eds. New York: American Inst. of Phys. 1981, pp. 627-642.
[5] N. H. Farhat, T. H. Chu, and C. L. Werner, "Tomographic and projective reconstruction of 3-D image detail in inverse scattering," in *Proc. 10th Int. Optical Computing Conf.*, pp. 82-88, 1983.
[6] N. H. Farhat, C. L. Werner, and T. H. Chu, "Prospects for 3-D tomographic imaging radar networks," in *Proc. URSI Symp. Electro-Magnetic Theory*, (Santiago De Compostela, Spain), Aug. 1983, pp. 279-301, Aug. 1983.
[7] N. H. Farhat, "Projection imaging of 3-D microwave scatterers with near optical resolution," in *Indirect Imaging*, J. A. Roberts, Ed. London: Cambridge University Press, 1984.
[8] N. H. Farhat, C. L. Werner, and T. H. Chu, "Prospects for three-dimensional projective and tomographic imaging radar networks," *Radio Sci.*, vol. 19, pp. 1347-1355, Sept.-Oct. 1984.
[9] D. Psaltis and N. Farhat, "Optical information processing based on an associative-memory model of neural nets with thresholding and feedback," *Opt. Lett.*, vol. 10, pp. 98-100, 1985.
[10] N. H. Farhat *et al.*, "Optical implementation of the Hopfield model,"*Appl. Opt.*, vol. 24, pp. 1469-1475, May 1985.
[11] N. Bojarski, "Three-dimensional short pulse inverse scattering," Syracuse Univ. Res. Rep., Syracuse. NY, 1967.
[12] N. Bajarski, "Inverse scattering," Naval Air Command Final Rep. N000 19-73-C0312F, 1974.
[13] R. M. Lewis, "Physical optics inverse diffraction," *IEEE Trans. Antennas Propagat*, vol. AP-17, pp. 308-314, May 1969.
[14] S. R. Raz, "On scatterer reconstruction from far field data," *IEEE Trans. Antennas Propagat.*, vol. AP-24, pp. 66-70, Jan. 1976.
[15] Y. Das and W. M. Boerner, "On radar shape estimation using algorithms for reconstruction from projections," *IEEE Trans. Antennas Propagat.*, vol. AP-26, pp. 274-279, Mar. 1978.
[16] W. M. Boerner, C-M. Ho, and B. Y. Foo, "Use of Radon's pro-

jection theory in electromagnetic inverse scattering," *IEEE Trans. Antennas Propagat.*, vol. AP-24, pp. 360-367, Mar. 1981.
[17] J. L. Walker, "Range-Doppler imaging of rotating objects," *IEEE Trans. Aerospace Electronic. Syst.*, vol. AES-16, pp. 23-25, Jan. 1980.
[18] D. C. Munson, J. D. O'Brien, and W. K. Jenkins, "A tomographic formulation of spotlight-mode synthetic aperture radar," *Proc. IEEE*, vol. 71, pp. 917-925, Aug. 1983.
[19] C. C. Cheng and H. C. Andrews, "Target motion induced radar imaging," *IEEE Trans. Aerospace Electron. Syst.*, vol. AES-16, pp. 2-14, Jan. 1980.
[20] N. H. Farhat and T. H. Chu, "Tomography and inverse scattering," in *Proc. 13th Cong. Int. Commission of Optics* (Sapporo, Japan), 1984, pp. 62-63, 1984.
[21] N. H. Farhat, C. K. Chan, and T. H. Chu, "A target derived reference for frequency diversity imaging," presented at the North American Radio Science/IEEE Meeting, Quebec, Canada, 1980.
[22] R. M. Mersereau and A. V. Oppenheim, "Digital reconstruction of multidimensional signals from their projections," *Proc. IEEE*, vol. 62, pp. 1319-1339, Oct. 1978.
[23] N. Farhat *et al.*, "Optical analogs to two-dimensional neural networks and their application in recognition of radar targets," in *Neural Networks for Computing*, J. S. Denker, Ed. New York: Am. Inst. of Phys., pp. 146-152, 1986.
[24] R. J. McEliece, E. C. Posner, E. R. Rodermich, and S. Venkatesh, "The capacity of the Hopfield associative memory," *IEEE Trans. Inform. Theory*, accepted for publication.
[25] G. R. Gindi and A. F. Gmitro, "Optical feature extraction via the Radon transform," *Opt. Engrg.*, vol. 23, pp. 499-506, Sept./Oct. 1984.
[26] G. Herman, *Image Reconstruction From Projections*. New York: Academic Press, 1980, p. 11.
[27] Super-resolution, patent disclosure filed by the University of Pennsylvania, April 1987.
[28] J. D. Stratton, *Electromagnetic Theory*. New York: McGraw-Hill, 1941, pp. 488-490.
[29] M. Van Blaricum and R. Mitra, "A technique for extracting the poles and resides of a system directly from its transient response," *IEEE Trans. Antennas Propagat.*, vol. AP-23, pp. 777-781, Nov. 1975.
[30] D. E. Rumelhardt and J. McClelland, *Parallel Distributed Processing*, Vols. I and II. Cambridge, MA: MIT Press, 1986.
[31] J. J. Hopfield, "Neural networks and physical systems with emergent collective computational abilities," *Proc. Natl. Acad. Sci.*, vol. 79, pp. 2554, 1982.
[32] N. H. Farhat, "Optoelectronic analogs of self-programming neural nets: Architectures and methodologies for implementing stochastic learning by simulated annealing," *Appl. Opt.*, vol. 26, pp. 5093-5103, Dec. 1987.
[33] N. H. Farhat and H. Bahri, "Phase space engineering for neurodynamic target identification," to be published in *Digest 1989 IEEE-APS Int. Symp. and URSI National Radio Science Meeting*.

Nabil H. Farhat received the B.Sc. degree in 1957 from the Technion-Israel Institute of Technology, Haifa; the M.Sc. degree in 1959 from the University of Tennessee, Knoxville; and the Ph.D. degree in 1963 from the University of Pennsylvania, Philadelphia, all in electrical engineering.

In 1964, he joined the faculty of the Moore School of Electrical Engineering, University of Pennsylvania, where he is now Professor in Electrical Engineering and heads the Electro-Optics and Microwave-Optics Laboratory. His current research interests are in image understanding, microwave imaging and holography, optical information processing and modeling of neural network and self-organizing systems, in all of which he has numerous publications. He is teaching courses in EM Theory, electrooptics and holography on both the graduate and undergraduate

levels. His past research included the study of the interaction of EM radiation with plasmas and solids in the context of laser output energy measurement and photodetachment of negative ions.

While Associative Professor, Dr. Farhat was named to the Ennis Chair in Electrical Engineering. In 1985, he was named Distinguished Visiting Scientist at the Jet Propulsion Laboratory in Pasadena. He is a recipient of the University of Pennsylvania Christian R. and Mary F. Lindback Foundation Award for distinguished teaching. He is a Fellow of the Optical Society of America, and is a member of Sigma Xi, Eta Kappa Nu, the New York Academy of Science, the American Institute of Physics, the American Society for the Advancement of Science, the Franklin Institute, and has served on the National Board of Directors of Eta Kappa Nu and has been an RCA consultant since 1969. Dr. Farhat has served as Editor of *Advances in Holography* and Associate Editor of *Acoustical Imaging and Holography*. He is currently engaged in the preparation of two texts: *An Introduction to Electro-Optics and Microwave Imaging* and *Holography-Theory and Applications*.

ORIGINAL CONTRIBUTION

Echo Inversion and Target Shape Estimation by Neuromorphic Processing

NABIL H. FARHAT AND BAOCHENG BAI

University of Pennsylvania

Abstract—*A neural net processor is described for echo inversions and target shape estimations from incomplete frequency response data. The processor accomplishes the inversion and estimation by minimizing an energy function which bears information about the measured data, as well as the relationship between the target shape function (image) to be reconstructed and its frequency response. An iterative algorithm is developed for the processor to minimize its energy function to give the desired image as its neural state outputs. Successful digital reconstructions with the neural net processor using microwave radar imaging data are presented and an opto-electronic implementation of the processor is described. Heuristic extension to make the processor more neuromorphic by introducing nonlinearity is discussed and digital reconstructions with this extension are shown; these reflect noticeable improvement in image quality.*

I. INTRODUCTION

Neural net models and their analogs (Ballard, 1986; Hopfield, 1982) represent a new approach to collective signal processing that is robust and fault tolerant and can be extremely fast. These properties stem directly from well recognized information processing capabilities of the brain. Although the brain is not as good in arithmetic operations as a digital computer, it is known that when it comes to operations such as association, categorization, classification, feature extraction, recognition, and optimization, it can outperform even the most powerful up-to-date computers. Collective information processing in the brain makes use of the massive interconnectivity of neurons (the decision making elements) of the brain and their ability to store information as weights of links between them. The brain's amazing capabilities in analyzing sensory data along with its complex thought and intelligent reasoning ability makes it an intriguing model for smart sensing and automated recognition systems. An interesting aspect of the

brain's ability to process sensory data is the ease with which it solves computationally complex problems, associated for example with vision, that are basically inverse problems which are known to be computationally vexing because of their ill-posedness (Tikhonov & Arsenin, 1977). When processing sensory data, the brain can still perform its tasks successfully even when the information it is presented is partial (or incomplete) and contains errors. Based on those remarkable information processing capabilities of neurons in the brain, a neural net processor is studied and reported upon here in the context of image reconstructions from incomplete data.

The problem of image (or object function) reconstruction from limited frequency data arises in many remote sensing applications including radar and sonar imaging. A one-dimensional object function $f(r)$ of limited extent possesses a frequency response (Fourier transform) $F(p)$ that extends over the entire frequency space. In practice, the frequency response $F(p)$ can only be measured over a finite region of the frequency space (p-space). The traditional approach by Fourier inversion of the measured response $F_d(p)$ yields an imperfect estimate $\hat{f}(r)$ of the object function because values of $F(p)$ outside the frequency measurement window are taken to be zero which violates a priori knowledge. Retrieval of $f(r)$ from $F_d(p)$ is also known to be an ill-posed problem in the sense that noise contamination and incom-

pleteness of the measured response $F_d(p)$ can result in large fluctuations in object function reconstructions. The neural net processor to be discussed accomplishes the reconstruction from incomplete frequency response data by minimizing an energy function which bears information about the measured data, the underlying (Fourier) relationship between the object function and the measured data. The energy function is set up in such a way as to agree with a priori knowledge and overcome the ill-posedness of the problem. An iterative algorithm for the processor is derived and its performance evaluated numerically in the reconstruction of radar range profiles from realistic data will be presented. The realistic data are collected in a broad-band microwave cross-section measurement facility employing microwave diversity techniques in which angular, spectral, and polarization degrees of freedom are combined to extract maximum information about the scattering object. Therefore all the following discussion with regards to imaging will be relevant to microwave diversity radar imaging.

The implementation of the neural net processor can be achieved opto-electronically. The massive connectivity and parallelism of the neural net processor can be realized by optics while the decision making and any required gain can be realized by electronics. The detailed implementation scheme of the neural net processor will be discussed. Finally, heuristic extension of the neural net processor to include nonlinear neural mapping, which makes it more neuromorphic, will be discussed and the reconstruction of microwave diversity radar image based on this extension will also be given.

II. BACKGROUND

In microwave diversity radar imaging (Farhat, Werner, & Chu, 1985a) as well as in many other radar imaging applications, such as synthetic aperture radar, etc., the frequency response of an object (or target) to be imaged can be accessed only for a limited frequency band and a limited range of aspect viewing angles, because of instrument limitations and other practical reasons. The data in the microwave imaging system described in Farhat et al. (1985a) are collected over a polar format or polar frequency grid depicted in Figure 1. Here p_x and p_y are Cartesian coordinates of spatial frequency space (p-space); p_1 and p_2 are the start and stop spatial frequencies, respectively, associated with the start and stop frequencies ω_1 and ω_2 employed in gathering the frequency response data; θ_1 is the start viewing angle and θ_2 the stop viewing angle, and $\Delta\theta$ is the total viewing angle. The purpose of microwave imaging is to extract information such as the size and shape, about a scattering target through microwave scatter-
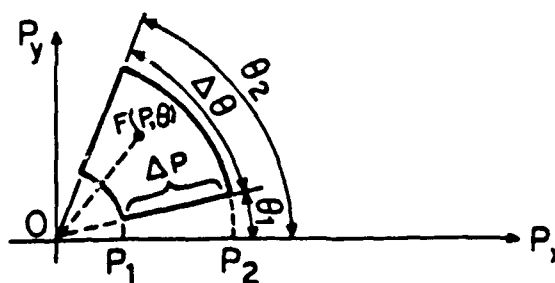

FIGURE 1. The p-space data collection in microwave imaging.

ing measurement; to achieve this goal in three dimensions for a 3-dimensional (3-D) object in reality, the frequency scattering measurement has to be carried out in the 3-D Fourier or frequency space of the object. But measurement over 3-D manifold in Fourier space is impractical. On the other hand, the 2-dimensional (2-D) frequency space grid shown in Figure 1, which represents a slice of the 3-D frequency space, can be easily accessed with practically feasible radar systems (Farhat et al., 1985a). When inverted, this 2-D frequency space measurement gives rise to a 2-D projection image of the 3-D object and with sufficiently wide angular window (range of aspect angles) $\Delta\theta$ enough image information for identification of the object can be obtained as will be seen in the results shown later. The 2-D image can be reconstructed from the frequency measurement over the frequency space grid in Figure 1 by invoking the filtered back-projection theorem (Farhat, Ho, & Chang, 1983) as follows: first, 1-dimensional (1-D) inversion along the radial direction with respect to the variable p for a given aspect angle θ is done to obtain the so called range-profile which bears information about the projection of the scattering centers of the 3-D object on the line of sight of the interrogating radar or a radar cross-section measurement system for the given aspect angle θ. Then, the 2-D image is reconstructed by coherently summing the filtered back-projected value (Farhat et al., 1983) of every range profile for all aspect angles taken in the imaging process (see Farhat et al. (1983) for more details).

The 2-D object function to be reconstructed should reveal the size and shape of the scattering target. Such a 2-D object function can be found under general approximations. There are two approximations involved in high resolution microwave imaging work. One is the physical optics approximation, which requires the wave-length of the microwave used for imaging be smaller than the characteristic size of the object, and the other is the Born approximation, which ignores multiple scattering at the object (Farhat et al., 1985a; Ruck, Barrick, Stuart, & Krichbaum, 1970). If the imaging fre-

quency band (spectral window) $\omega \in [\omega_1, \omega_2]$ is chosen to satisfy both approximations, it can be rigorously shown (Chan & Farhat, 1981) that the frequency response $F(p, \theta)$ (or $F(\omega, \theta)$) corresponds to a real object function when the object is perfectly conducting or when it is composed of a lossless dielectric. We will concentrate on this kind of object; however, the method presented can be extended to other kind of objects.

From the 2-D image reconstruction procedure mentioned earlier, it is seen that the 2-D image is just a projected summation of range profiles over the θ direction and this summation process is, of course, well-posed (Hadamard, 1923; Tikhonov & Arsenin, 1977) and can be done to the desired accuracy. Therefore, if the range profile for every aspect angle can be retrieved correctly, the 2-D image will be reconstructed satisfactorily. The issue is then how to reconstruct the range profile for every individual aspect angle satisfactorily. Since the range profile reconstruction for a given aspect angle is a 1-D problem, we will use scalers r and p to represent points in object domain and Fourier space or p-space, respectively, and by object function we will be referring one range profile, unless it is otherwise specified as a 2-D or 3-D object function in the following analysis. The traditional approach to reconstructing a range profile is to employ the Fourier inversion method. Fourier inversion of the measured frequency response $F_d(p)$ yields an estimate of the object function,

$$f(r) = \int_{-\infty}^{+\infty} F_d(p)e^{ipr}dp = \int_{p_1}^{p_2} F(p, \theta)e^{ipr}dp. \quad (1)$$

Here, the following assumption about the measured data has been made,

$$F_d(p) = \begin{cases} F(p, \theta) & \text{for } p_1 \leq p \leq p_2 \text{ and fixed } \theta \\ 0 & \text{otherwise} \end{cases}$$

For the Fourier inversion method, it is assumed that the frequency response $F(p)$ outside the measurement band $[p_1, p_2]$ is zero and consequently the object function $f(r)$ estimated from the finite measurement band will generally be complex. The assumption and the result violate a priori knowledge that an object function of finite extent in practice has a frequency response of infinite extent and that the object function to be reconstructed is real. Failure of Fourier inversion in eqn (1) to satisfy a priori knowledge can be traced to the ill-posed nature of the inverse problem (Hadamard, 1923; Tikhonov & Arsenin, 1977). In practice, the measured frequency response is contaminated more or less by noise, and also the measured response $F_d(p)$ is only part of the Fourier transform of the object function $f(r)$ to be reconstructed and $F_d(p)$ is incomplete. Retrieval of

$f(r)$ from $F_d(p)$ is ill-posed in the sense that small change in the measured frequency response $F_d(p)$ can alter radically the estimate $f(r)$ of the object function as a consequence of noise contamination and incompleteness of $F_d(p)$. This motivates the study for a new method to achieve fast and robust reconstructions satisfying a priori knowledge.

III. RECONSTRUCTION BY NEURAL PROCESSOR

A neural net processor is studied to solve the problem of object function reconstruction from incomplete frequency responses. The neural net processor models the collective computational behavior of neurons in human brains and is set up to be formed of massively interconnected "neurons" with parallel processing capability. The problem to be solved by the neural net processor is formulated in terms of desired optima (usually minima). To compute solutions to the optimization problem, the connectivities (synapses) of the net form an energy space to appropriately represent the optimization problem so that the net will rapidly converge to its energy minima corresponding to the minima of the problem when the bias input representing the available information is fed into the net.

The reconstruction of range profile for an individual aspect angle in microwave diversity imaging is a 1-dimensional problem. For a given aspect angle, since the frequency response of the range profile (or 1-D object function) is known for a finite frequency band and to reconstruct the original object function from this kind of knowledge of the frequency response is an ill-posed problem, the energy function for the neural net is set up by the following considerations:

1. The Fourier transform of the reconstructed object function should agree with the known (measured) frequency response over the given frequency band $[p_1, p_2]$ in the "best way";
2. the ill-posedness will be remedied by using regularization (Tikhonov & Arsenin, 1977).

Accordingly, the following function is chosen as the energy function,

$$H(\bar{f}) = \|F_d(p) - F(p)\|^2 + \alpha R(\bar{f}) \quad (2)$$

where, $\bar{f}$ denotes the object function to be reconstructed and is a state vector of the net; $F_d(p)$ the frequency response from measurement over $[p_1, p_2]$; $F(p)$ the Fourier transform of $\bar{f}$, and $\|\cdot\|$ a norm defined on the frequency space $\dot{c} \ni F(p)$. It is seen that the first term in eqn (2) does reflect the fitness of the reconstruction with the known data in the frequency domain, that is, the first term vanishes if

$F_d(p) = F(p)$. The term $R(\bar{f})$ in eqn (2) is a regularization operator on $\bar{f}$ to overcome the ill-posedness of the problem and it is chosen by considerations of the object function to be reconstructed and a priori knowledge. Since functions representing physical objects in microwave diversity imaging are usually continuous and cannot have abrupt discontinuities, so Tikhonov's regularization functions (Tikhonov & Arsenin, 1977) and their similar forms for maintaining smoothness of the reconstruction will be used and represented by $R(\bar{f})$; one of the Tikhonov's regularization functions used in our study is,

$$R(\bar{f}) = \int \{f^2(r) + [f'(r)]^2\} dr. \qquad (3)$$

The constant α in eqn (2) is called the regularization parameter to control the trade off between fitness (small α) and smoothness (large α) of reconstructions.

When the Fourier transform $F(p)$ is expressed in terms of the object function $\bar{f}$, the energy function $H(\bar{f})$ in eqn (2) will only be a function of the variable $\bar{f}$, since F_d is the measured frequency response and is known. An iterative algorithm for the neural net processor is derived by evaluating $dH(\bar{f})/df(m)$ to find the energy change ΔH due to the change of the mth sample of $\bar{f}$ or the change of the state value of the mth neuron in the processor. To find the minima of $H(\bar{f})$, $H(\bar{f})$ is desired to decrease as $\bar{f}$ changes and accordingly the update neural net iterative equation (see appendix for detail derivations) for the $(j + 1)$th iteration in terms of the jth iteration is found as,

$$f^{(j+1)}(m) = f^{(j)}(m)$$
$$+ \lambda \left\{ \sum_{m'=0}^{M} 2Re[T_{m,m'}]f^{(j)}(m') + I - S_m \right\} \qquad (4)$$

where S_m is viewed as a regularization related adaptive threshold and for the regularization function in eqn (3), it is given by,

$$S_m = 2\alpha \left\{ f^{(j)}(m) \left(\Delta r + \frac{1 + A_2}{\Delta r} \right) - \frac{1}{\Delta r} \right.$$
$$\left. [A_1 f^{(j)}(m - 1) + A_2 f^{(j)}(m + 1)] \right\} \qquad (5)$$

with Δr being the sampling interval in the object space $\ni \bar{f}$ and A_1 and A_2 given constants. $Re[T_{m,m'}]$ is the real valued interconnectivity matrix that represents the underlying Fourier transform and is given by

$$Re[T_{m,m'}] = -Re \left[\sum_{i=1}^{N} K_{im} K_{im}^* \right]$$

with N being the total number of measurement samples in the frequency domain and K_{im} the Fourier

kernel. The term I_m in eqn (4) is the external input related to the measured data and is given by

$$I_m = 2Re \left[\sum_{i=1}^{N} F_d(i) K_{im}^* \right]$$

and is identified as the real part of the complex range profile generated by Fourier inversion of the measured frequency response F_d; λ in eqn (4) is defined as the "gain" of the mth neuron in the net and is chosen as to satisfy,

$$\frac{1}{\lambda} + \left[T_{k,k} - \alpha \left(\Delta r + \frac{1 + A_2}{\Delta r} \right) \right] > 0 \qquad (6)$$

in order to make $H(\bar{f})$ decrease as $\bar{f}$ changes. The iterative neural net algorithm in eqn (4) has been digitally tested with realistic data F_d for scale models of aerospace test objects collected in a microwave imaging facility at the University of Pennsylvania. One of the models used is a B-52 airplane. The frequency response data are collected over a frequency window from 6(GHz) to 17(GHz) and a 90° angular viewing window which extends from the broadside to head-on of the airplane. Over the 90° viewing window, there are totally 128 looks (views) taken and the range profile for each view is reconstructed from the measured frequency response data using the neural net processor expressed by eqn (4); the 2-D object function is finally obtained by the back-projection algorithm which coherently sums the filtered back-projected value of $\bar{f}$ for all the views in the proper angular orientations over a rectangular image plane grid (Farhat et al., 1983). Shown in Figure 2(a) is the B-52 airplane model used; Figures 2(b) and 2(c) show the 1-D range-profiles reconstructed by the FFT algorithm and the neural net processor, respectively. Shown in Figure 2(b) is the modulus of the reconstructed complex range profile while shown in Figure 2(c) is the intensity of the real range profile. The 2-D object image reconstructed by the traditional FFT and filtered back-projection is shown in Figure 3(a) and that obtained by the neural net processor followed by filtered back-projection is shown in Figure 3(b). Since the airplane is illuminated from only one-side of the fuselage, images initially reconstructed are brighter on the illuminated side of the fuselage and both images shown in Figures 3(a) and 3(b) are the symmetrically enhanced images of the initial reconstructions about the symmetrical axis of the airplane—the fuselage. It is worth noting that most man made aerospace objects possess one or more axis of symmetry and these are usually determined from object bearing. Comparing the reconstructions by the two different methods, the following observations can be made.

- Reconstruction by the neural net processor has lower back-ground noise level which can be helpful
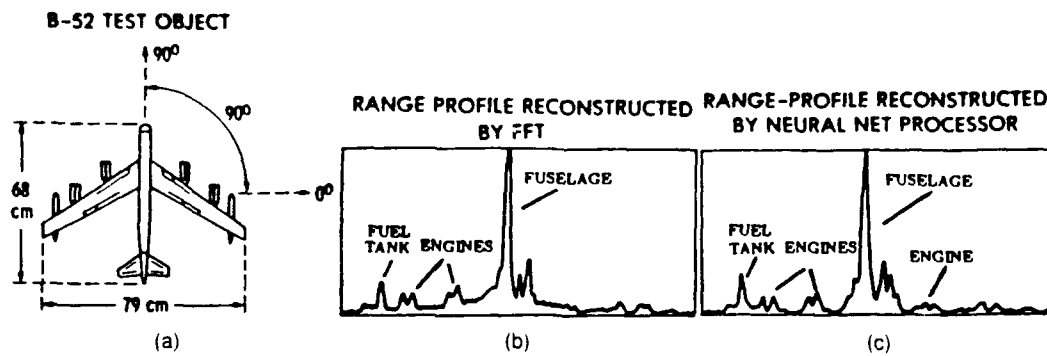
FIGURE 2. (a) B-52 airplane model; (b) reconstruction by FFT; (c) reconstruction by neural net processor.

in practical applications where signal to noise ratio is low and leads to improved images.

• Reconstruction by the neural net processor is obtained by assuming that the object function is real and this makes it easier for opto-electronic implementations.

IV. OPTO-FLECTRONIC IMPLEMENTATION OF NEURAL NET PROCESSOR

Optical processing systems offer potential for ultra fast speed and means for realizing parallel processing as well as massive interconnections among processing elements. Therefore, optics can be used for the implementations of neural net models (Farhat, Psaltis, Prata, & Paek, 1985b) for computing and information processing, while the decision making elements in the implementation can be realized electronically at present. The architecture for an opto-electronic implementation ot the neural net iterative algorithm expressed in eqn (4) is shown in Figure 4. The neural state vector $\bar{f}$ in the implementation is represented by the output of the light emitting diode (LED) array. Although LED can only represent positive func-

tions with its output intensity, the real valued function $f^{(i)}(m)$ in microwave diversity imaging can be handled by using separate LEDs to code positive and negative values of $f^{(i)}(m)$. The interactions among neurons are provided by broadcasting the neural states, that is, the outputs of the LEDs, through the 2-D interconnectivity matrix mask $Re[T_{m,m'}]$ and the output (the activation potential) of each neuron is picked up by the photo-detector (PD) array. The term I_m that represents the measurement data and the adaptive threshold S_m that overcomes the ill-posedness of the problem can be computed digitally and injected into the system either electronically or optically as shown, but completely analog schemes for computing these terms are also possible (an example of analog generation of S_m is given below). The neural "gain" $\lambda(\lambda < 1)$ can be realized with an optical or electronic attenuation. The resultant output from each attenuator would be used to drive the LED array which will in turn update the neural state to $f^{(i-1)}(m)$ for the $(j + 1)$th iteration.

The regularization factor S_m is adaptively generated in analog fashion according to the neural state
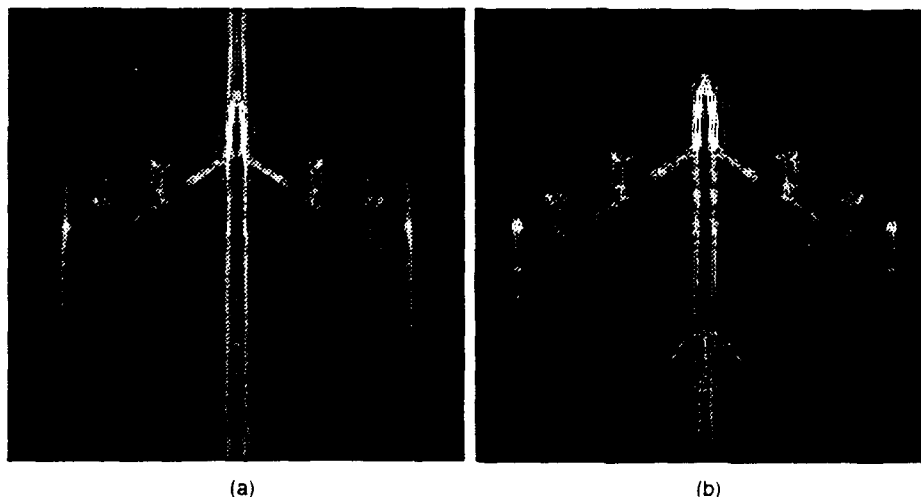

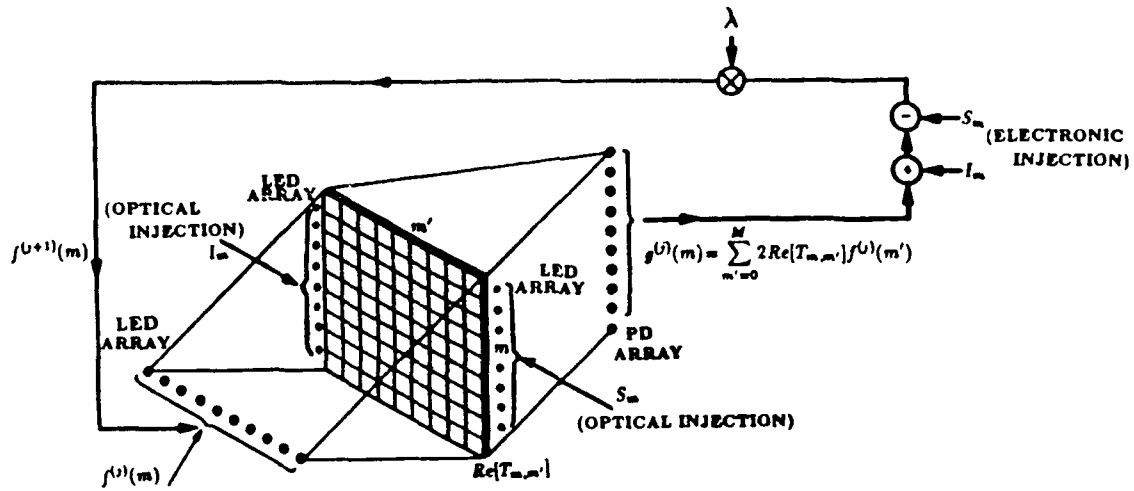FIGURE 3. (a) 2-D image reconstructed by FFT; (b) 2-D image reconstructed by neural net processor.

FIGURE 4. Opto-electronic implementation.

in the net. Shown in Figure 5 is an optical shuffle scheme for doing this. The input to this generating system is the neural state array $f^{(j)}(m)$ in Figure 4 and the output can be fed into the neural net iterative processor shown in Figure 4 either electronically or optically (e.g., through the vertical LED array S_m). The anamorphic imaging systems, L_1 and L_2, are used to smear LEA (light emitting array) output representing the neural states vertically over the beam splitter cube (BSC). Properly arranged, the tilted mirrors TM_1 and TM_2 can reflect the light from the BSC to PDA1 to form the term $[f^{(j)}(m - 1) + f^{(j)}(m + 1)]$, while the mirrors M_1 and M_2 can reflect the light from BSC to PDA2 to form the term $f^{(j)}(m)$. The constants $(1/\Delta r)$ and $[\Delta r + (2/\Delta r)]$ shown in Figure 4 are obtained by setting $A_1 = A_2 = 1$ in S_m in eqn (5) for the cases of $0 < m < M$ and they can

be multiplied with the proper terms through optical (or electronic) multipliers.

V. HEURISTIC EXTENSION

By examining the neural net iterative algorithm expressed in eqn (4), the overall activation potential of the mth neuron in the net can be written as,
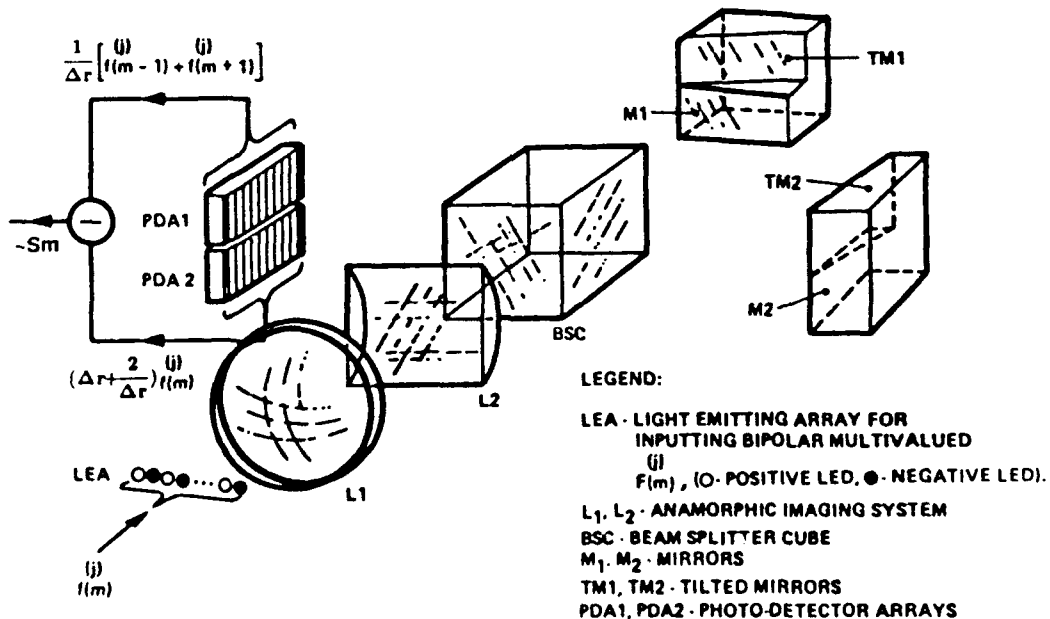
$$u_m = \sum_{m'} W_{m,m'} \cdot v_{m'} - \theta_m + \lambda I_m \qquad (7)$$

where,

$$v_{m'} = f(m')$$

$$W_{m,m'} = \delta_{m,m'} + 2\lambda Re[T_{m,m'}]$$

$$\theta_m = \lambda S_m.$$

FIGURE 5. Optical shuffle scheme for generating S_m.

The mapping equation in conventional neural nets is.

$$v_m = g(u_m) \qquad (8)$$

and $g(u_m)$ is a sigmoidal function. For the problem of image reconstruction. multivalued neural states v_m have to be used to represent the bipolar object function. In an attempt to make the neural net processor more neuromorphic. modification must be made to the conventional neural mapping equation expressed in eqn (8) to preserve the multivalued neural responses. Heuristically therefore the nonlinear mapping will be confined only to the adaptive threshold θ_m such that $\theta_m = g(S_\tau)$ with S_τ being a linear combination (window) of the neural state vector $\bar{v}$ of the net. The term I_m. which represents the known information. will not go through the nonlinear mapping in order to preserve the original available information. Accordingly. the neural state mapping equation will be of the following form.

$$v_m = \sum_{m'} W_{m,m'} v_{m'} - g(S_\tau) + \lambda I_m. \qquad (9)$$

As mentioned earlier. the adaptive threshold represents the regularization factor in the original energy function. The introduction of nonlinear adaptive threshold $g(S_\tau)$ will extend the set of the regularization functions applicable. The adaptive threshold S_m in eqn (5) can be viewed as a linear convolution (or a kind of linear mapping) $\bar{f} * \bar{x}$ of the neural states $\bar{f}$ with a filter $\bar{x}$ consisting of three discrete points having values

$$x(-1) = -A_2 \Delta r. \; x(0) = \Delta r - \frac{1 - A_1}{\Delta r}.$$
$$x(1) = -A_1 \Delta r$$

respectively. as shown in Figure 6(a) when $A_1 = A_2 = 1$. This linear mapping can be replaced with a

nonlinear mapping of the form $\zeta \tanh(\eta S_\tau)$. where ζ and η are constant parameters. A preliminary image obtained with this nonlinear adaptive threshold is given in Figure 6(b) which reveals features of the original object that were not discernible in the preceding images. For example. the double barreled nature of the engines is now more clearly delineated.

VI. DISCUSSION

The neural net processor can also be used for object reconstructions when the relationship between the measurement data and the object function is not necessarily Fourier transform: in this case. there is no fast and robust algorithm found so far for reconstructions. But the neural net processor concept presented here can be easily applied just by modifying the optical mask representing the underlying transform to achieve fast and robust reconstructions. The term $I_m = 2Re\left[\sum_{i=1}^{N} F_d(i) K_{im}^*\right]$ is actually the real part of the complex range-profile computed from measured frequency response data by FFT and it can be viewed as the partial input "seed" or "key" to the neural net as the initial estimate of the real range profile of the object function to be reconstructed. The neural net processor concept described can be applied to a wide range of practical problems simply by inputing the corresponding partial "key" as I_m to the neural net. Nonlinear regularization functions can be introduced in the neural net processor as described and many nonlinear or linear regularization functions with high degree of smoothness that is difficult to realize rapidly by digital computation can be easily realized optically. The regularization parameter α. which controls the fitness and smoothness of the reconstructions in our research of microwave image reconstructions. can also be adaptively changed dependent on the fitness of the reconstruction with the
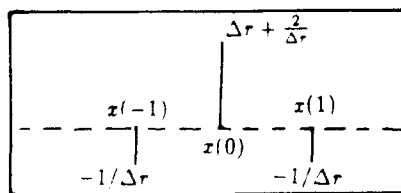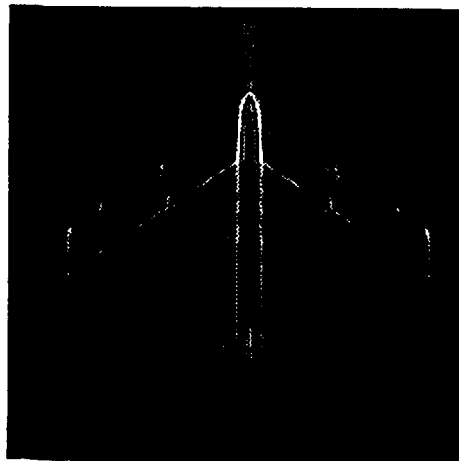
(a) (b)

FIGURE 6. (a) Linear mapping function: (b) image reconstructed by nonlinear mapping.

measurement data during the iterative process of the neural network. Doing imaging adaptively, and incorporating attractive information processing features of neurons, could make processors of the kind described here unique and powerful to outperform many existing processors.

REFERENCES

Ballard, D. H. (1986). Cortical connections and parallel processing: Structure and function. *Behavioral and Brain Sciences*, **9**, 67–120.

Chan, C., & Farhat, N. H. (1981). Frequency swept tomographic imaging of three-dimensional perfectly conducting objects. *IEEE Transaction on Antennas and Propagation*, **AP-29**, 312–319.

Farhat, N. H., Ho, Y., & Chang, L. S. (1983). Projection theorem and their application in multi-dimensional signal processing. In G. M. Morris (Ed.), *Advances in optical information processing, Proceedings of the International Society of Photo-Optical Instrumentation*, **388**, 140–151.

Farhat, N. H., Werner, C. L., & Chu, T. H. (1985a). Prospects for three-dimensional projective and tomographic imaging radar network. *Radio Science*, **19**, 1347–1355.

Farhat N. H., Psaltis, D., Prata, A., & Paek, E. (1985b). Optical implementation of the Hopfield model. *Applied Optics*, **24**, 1469–1475.

Hadamard, J. (1923). *Lectures on the Cauchy problem in linear partial differential equations*. New Haven, CT: Yale University Press.

Hopfield, J. J. (1982). Neural network and physical systems with emergent collective computational abilities. *Proceedings of the National Academy of Sciences of the United States of America*, **79**, 2554–2558.

Ruck, G. T., Barrick, D. E., Stuart, W. D., & Krichbaum, C. K. (1970). *Radar cross section handbook*. New York: Plenum Press.

Tikhonov, A. N., & Arsenin, V. Y. (1977). *Solutions of ill-posed problems*. New York: Wiley.

APPENDIX: DERIVATION OF THE ITERATIVE EQUATION

This appendix derives the iterative equation for the neural net processor. The energy function for the neural net processor is given in eqn (1) and is rewritten here,

$$H(\bar{f}) = \|F_d - F\|^2 + \alpha R(\bar{f}). \qquad (A.1)$$

As mentioned in the text, $\bar{f}$ denotes the object function to be reconstructed and F is the Fourier tansform of $\bar{f}$; F_d is the frequency response from measurement; $R(\bar{f})$ is a regularization operator on $\bar{f}$ and α a regularization parameter. In the derivation here, we will use the following form as the norm in the frequency domain,

$$\|F_d - F\|^2 = \sum_{i=1}^{N} |F_d(i) - F(i)|^2 \qquad (A.2)$$

where N is the number of samples in the frequency space and also the number of frequency measurement samples. $F_d(i)$ and $F(i)$ are the frequency response samples at the ith frequency point.

For a spatially limited function $f(r)$ and its Fourier transform $F(p)$, there exists the following relationship,

$$F(p) = \int_a^b f(r)e^{-ip r}dr \qquad (A.3)$$

where the spatially limited function $f(r)$ is assumed as,

$$f(r) = \begin{cases} \neq 0 & \text{if } r \in [a, b] \\ = 0 & \text{otherwise.} \end{cases}$$

Usually, $F(p)$ is measured at equally spaced discrete frequency points in $[p_1, p_2]$, that is,

$$p_i = p_1 + (i - 1)\frac{p_2 - p_1}{N - 1} \quad i = 1, 2, \ldots, N \qquad (A.4)$$

where $[p_1, p_2]$ corresponds to the frequency band $[\omega_1, \omega_2]$ used in the measurement.

Replace eqn (A.3) with a linear algebraic equation for computation purposes,

$$F(i) = F(p_i) = \sum_{m=0}^{M} K_{im} f(m). \qquad (A.5)$$

The approximation sum of Simpson's rule for an integral is,

$$\int_a^b g(x)dx \approx \frac{h}{3}[y_0 + y_l + 2(y_2 + y_4 + \cdots + y_{l-2})$$
$$+ 4(y_1 + y_3 + \cdots + y_{l-1})]$$

where, l is an even number and the function $g(x)$ is evaluated at point x_k, which satisfies the relationship $x_k = a + kh$ (h can be a constant or variable), to give $y_k = g(x_k)$, for $k = 0, 1, 2, 3, \ldots, l - 1, l$.

If Simpson's sum is used in eqn (A.5), we have,

$$f(m) = f(a + m \cdot \Delta r) \quad \left(\Delta r = \frac{b - a}{M}\right) \qquad (A.6)$$

$$K_{im} = \frac{\beta \Delta r}{3} e^{-ip_i(a + m\Delta r)} \qquad (A.7)$$

where, the constant β is given according to Simpson's rule as,

$$\beta = \begin{cases} 1 & \text{if } m = 0 \text{ and } m = M \\ 2 & \text{if } m \text{ is even and } m \neq M \\ 4 & \text{if } m \text{ is odd} \end{cases}$$

and M is an even integer and $(M + 1)$ is the total number of samples in the object domain.

If the regularization function in eqn (3) in the text is used and the rectangular rule is used for its numerical evaluation, the energy function in eqn (A.1) will be of the following form,

$$H(\bar{f}) = \sum_{i=1}^{N} |F_d(i) - F(i)|^2$$
$$+ \alpha \sum_{m=0}^{M} \left\{ f^2(m) + \left[\frac{f(m - f(m - 1)}{\Delta r}\right]^2 \right\} \Delta r$$
$$= \sum_{i=1}^{N} [|F_d(i)|^2 - F_d(i)F^*(i) - F_d^*(i)F(i) + F(i)F^*(i)]$$
$$+ \sum_{m=0}^{M} \left\{ f^2(m) + \left[\frac{f(m - f(m - 1)}{\Delta r}\right]^2 \right\} \Delta r. \qquad (A.8)$$

Using eqn (A.5), we will have,

$$\sum_{i=1}^{N} F(i)F^*(i) = \sum_{i=1}^{N} \left[\sum_{m=0}^{M} K_{im}F(m)\right]\left[\sum_{m'=0}^{M} K_{im'} F(m')\right]^*$$
$$= \sum_{m=0}^{M} \sum_{m'=0}^{M} \left[\sum_{i=1}^{N} K_{im}K_{im'}^*\right] f(m)f^*(m')$$
$$= -\sum_{m=0}^{M} \sum_{m'=0}^{M} T_{m,m'} f(m)f(m'). \qquad (A.9)$$

Here, the notation

$$T_{m,m'} = -\sum_{i=1}^{N} K_{im}K_{im'}^*$$

has been used and $f^*(m') = f(m')$, that is, $f(m')$ is real, has been assumed.

Treating the other term accordingly, we will get,

$$\sum_{i=1}^{N} [F(i)F_d^*(i) + F^*(i)F_d(i)] = \sum_{m=0}^{M} I_m f(m) \qquad (A.10)$$

with the notation,

$$I_m = \sum_{i=1}^{N} [K_{im}F_d^*(i) + K_{im}^*F_d(i)] = 2Re\left[\sum_{i=1}^{N} F_d(i)K_{im}^*\right].$$

From eqn (A.5), it is seen that the direct Fourier inversion of the measured frequency response $F_d(i)$ would yield an estimate of the object function given by (with a scale constant),

$$f(m) = \sum_{i=1}^{N} F_d(i)K_{im}^* \qquad (A.11)$$

and I_m would just be the real part of this Fourier estimate.

Using eqns (A.9) and (A.10), the energy function $H(\bar{f})$ can be rewritten as,

$$\begin{aligned}
H(\bar{f}) = &-\sum_{m=0}^{M}\sum_{m'=0}^{M} T_{m,m'} f(m)f(m') \\
&- \sum_{m=0}^{M} I_m f(m) + \sum_{i=1}^{N} |F_d(i)|^2 \\
&+ \alpha \sum_{m=0}^{M} \left[f^2(m)\left(\Delta r + \frac{1}{\Delta r}\right) \right. \\
&\left. - \frac{2}{\Delta r} f(m)f(m-1) + \frac{f^2(m-1)}{\Delta r} \right]. \qquad (A.12)
\end{aligned}$$

Note that $f(m) = 0$ for $m < 0$ or $m > M$ has been assumed.

The first derivative of $H(\bar{f})$ with respect to $f(m)$ is found as,

$$\begin{aligned}
\frac{dH(\bar{f})}{df(m)} = &-\sum_{m'=0}^{M} [T_{m,m'} + T_{m',m}]f(m') - I_m \\
&+ 2\alpha\left\{ f(m)\left(\Delta r + \frac{1+A_2}{\Delta r}\right) \right. \\
&\left. - \frac{1}{\Delta r}[A_1 f(m-1) + A_2 f(m+1)]\right\} \qquad (A.13)
\end{aligned}$$

where, the constants A_1 and A_2 are given as,

$$A_1 = \begin{cases} 1 & \text{if } 0 < m \le M \\ 0 & \text{if } m = 0 \end{cases}$$

$$A_2 = \begin{cases} 1 & \text{if } 0 \le m < M \\ 0 & \text{if } m = M. \end{cases}$$

From $T_{m,m'} = -\sum_{i=1}^{N} K_m K_{m'}^*$, it is seen that $T_{m',m} = -\sum_{i=1}^{N} \times K_{m'} K_m^* = (T_{m,m'})^*$, so,

$$T_{m,m'} + T_{m',m} = 2Re[T_{m,m'}]. \qquad (A.14)$$

If the higher order derivatives are ignored, the change ΔH of the energy function $H(\bar{f})$ due to the change of the mth neuron's output $f(m)$ can be written as,

$$\begin{aligned}
\Delta H = H^{(i+1)}(\bar{f}) - H^{(i)}(\bar{f}) &= \frac{dH(\bar{f})}{df(m)} \Delta f(m) \\
&= \frac{dH(\bar{f})}{df(m)} [f^{(i+1)}(m) - f^{(i)}(m)]. \qquad (A.15)
\end{aligned}$$

We want to find the minima of $H(\bar{f})$, so we want $H(\bar{f})$ to decrease as $f(m)$ changes, that is,

$$\Delta H = \frac{dH(\bar{f})}{df(m)} [f^{(i+1)}(m) - f^{(i)}(m)] < 0. \qquad (A.16)$$

Therefore, we take,

$$\Delta f(m) = f^{(i+1)}(m) - f^{(i)}(m) = -\lambda \cdot \frac{dH(\bar{f})}{df(m)}. \qquad (A.17)$$

Here, the constant λ is chosen in such a way as to ensure descent of the energy of the net to a minimum of $H(\bar{f})$ and this will be discussed later in this appendix.

From eqns (A.13) and (A.14) and using the proper values for the constants A_1 and A_2, we will have,

$$\begin{aligned}
f^{(i+1)}(m) &- f^{(i)}(m) \\
&= \lambda\left\{ \sum_{m'=0}^{M} 2Re[T_{m,m'}]f^{(i)}(m') + I_m - S_m\right\} \qquad (A.18)
\end{aligned}$$

with the term S_m being,

$$\begin{aligned}
S_m = 2\alpha\left\{ f^{(i)}(m)\left(\Delta r + \frac{1+A_2}{\Delta r}\right) \right. \\
\left. - \frac{1}{\Delta r}[A_1 f^{(i)}(m-1) + A_2 f^{(i)}(m+1)]\right\}. \qquad (A.19)
\end{aligned}$$

It is seen that eqn (A.18) is the iterative equation for the processor given in eqn (4) in the text and when $0 < m < M$, eqn (A.19) is eqn (5) in the text.

Now let us determine the conditions that λ must satisfy in order to find the minimum of $H(\bar{f})$. When the value of the kth neuron is changed from $f^{(i)}(k)$ to $f^{(i)}(k) + \Delta f(k)$, the energy function change can be written as,

$$H(\bar{f}) + \Delta H_k(\bar{f}) = H(\bar{f} + \delta_{km}f(m)). \qquad (A.20)$$

Referring to eqn (A.12), it is found,

$$\begin{aligned}
\Delta H_k(\bar{f}) = &-\sum_{m'=0}^{M} [2Re[T_{k,m'}]f(m') + I_k - S_k] \Delta f(k) \\
&- \left[T_{kk} - \alpha\left(\Delta r + \frac{1+A_2}{\Delta r}\right)\right] [\Delta f(k)]^2. \qquad (A.21)
\end{aligned}$$

Using eqns (A.17) and (A.18) to express $\Delta f(k)$, we will obtain,

$$\Delta H_k(\bar{f}) = -\left[\frac{1}{\lambda} + T_{kk} - \alpha\left(\Delta r + \frac{1+A_2}{\Delta r}\right)\right] [\Delta f(k)]^2. \qquad (A.22)$$

Since $[\Delta f(k)]^2$ is nonnegative, if λ satisfies,

$$\frac{1}{\lambda} + \left[T_{kk} - \alpha\left(\Delta r + \frac{1+A_2}{\Delta r}\right)\right] > 0 \qquad (A.23)$$

then, $\Delta H_k(\bar{f}) \le 0$, that is, $H(\bar{f})$ will decrease and find its minima as $f(m)$ changes.

From eqn (A.7) and the notation $T_{m,m} = -\sum_{i=1}^{N} K_m K_m^*$, we can find,

$$T_{kk} = -\sum_{i=1}^{N} K_k K_k^* = -\sum_{i=1}^{N} |K_k|^2 = -\frac{(\beta\Delta r)^2}{9} N \qquad (A.24)$$

which is a known constant for the given sample interval Δr in the object domain and the total number of samples N in the frequency domain. Therefore, λ can be determined from the known quantities according to eqn (A.23).

LEARNING NETWORKS FOR EXTRAPOLATION AND RADAR TARGET IDENTIFICATION

Baocheng Bai and Nabil H. Farhat

University of Pennsylvania

The Moore School of Electrical Engineering

Electro-Optics and Microwave-Optics laboratory

Philadelphia, PA 19104

ABSTRACT: The problem of extrapolation for near-perfect reconstruction and target identification from partial frequency response data by neural networks is discussed. Because of ill-posedness, the problem has traditionally been treated with regularization methods. The relationship between regularization and the role of hidden neurons in layered neural networks is examined. and a layered nonlinear adaptive neural network for performing extrapolations and reconstructions with excellent robustness is set up. The results are then extended to neuromorphic target identification from a single "look" (single broad-band radar echo). A novel approach for achieving 100% correct identification in a learning net with excellent robustness employing realistic experimental data is also given. The findings reported could potentially obviate the need to form radar images in order to identify targets and could furnish a viable and economical means for identifying non-cooperative targets.

1   Introduction

For an object function $o(r)$ of finite spatial extent. the corresponding frequency response $F(p)$ extends over the entire frequency domain $-\infty < p < +\infty$. Because of practical constraints. the frequency response $F(p)$ can only be measured over a finite frequency window $p_1 < p < p_2$ to give the measured frequency response $F_m(p)$. The traditional and widely used approach of Fourier inversion. by means of a discrete Fourier transform (DFT). as an algorithm for retrieving $o(r)$ from $F_m(p)$ violates *a priori* knowledge of the object function

and yields an estimate of $o(r)$ with limited resolution, which may not satisfy the resolution requirements in demanding applications.

More sophisticated methods for retrieving a better estimate of $o(r)$ from $F_m(p)$ exist. The retrieval of $o(r)$ from the partial information $F_m(p)$ in the presence of noise is, however, known to be an ill-posed problem [1],[2]. Studies have been carried out for retrieving $o(r)$ by incorporating *a priori* knowledge and minimizing a certain "cost function" related to $F_m(p)$ subject to a given criterion [3]. Mathematically, the function to be minimized can be put into the following general form:

$$H(o) = ||F_m - F||^2 + \alpha R(o) \tag{1}$$

where F_m is the measured frequency response; F is the Fourier transform of the estimate function $o(r)$; $R(o)$, called the regularization function, is to ensure that the reconstructed $o(r)$ has certain smoothness properties; and α, called regularization parameter, adjusts the degree of fitness expressed in the first term on the right hand side of (1) relative to the degree of regularization or smoothness expressed in the second term. For example, the function $R(o)$ in Tikhonov's regularization method [1] is taken to be a sum of the squared derivatives of $o(r)$,

$$R_T(o) = \sum_k [o^{(k)}(r)]^2 \tag{2}$$

to ensure that $o(r)$ has the required degree of smoothness. Here $o^{(k)}$ represents the kth derivative of the function $o(r)$.

There are limitations, however, to all existing reconstruction algorithms: either an algorithm works well only for a certain class of object functions or the *a priori* knowledge requirement is too stringent to be satisfied. The maximum entropy algorithm [4], which works well for point-like object functions, can be placed into the former class, while the Papoulis-Gerchberg's algorithm [5],[6], which requires knowledge of the exact extent of objects, can be placed into the latter class. By inspecting equation (1), one appreciates that reconstructions will be dependent upon the regularization function $R(o)$ chosen and that a given $R(o)$ will only ensure certain regularization (or smoothing) properties for the object function $o(r)$. This is the reason why different algorithms with different $R(o)$ work well only for a certain set of object functions. For example, the maximum entropy algorithm works well for point-like object functions and Tikhonov's regularization is good for continuous object functions. This represents one difficulty in choosing the regularization function $R(o)$

in setting up the cost function $H(o)$ in (1). Another difficulty is in choosing the regularization parameter α for a given reconstruction problem. For practical reconstructions from noise contaminated data, the parameter α can be chosen mathematically depending on the signal-to-noise ratio in the data. This in turn introduces the added problem of having to estimate the signal-to-noise ratio, which in practice is difficult to do.

Neural net models offer a new dynamic approach to collective nonlinear signal processing that is robust and fault-tolerant and can be extremely fast when parallel processing techniques are utilized [3],[7]. Neural net models provide a new way of looking at signal processing problems and can offer novel solutions. A neural net processor for solving image reconstruction problems through the minimization of an energy function of the type given in (1) has been studied earlier [3]. Here, a neural net approach to the problem involving self-organization and learning is investigated. By making use of the neural paradigm albeit in a highly simplified and loose sense, our nets allow for complex neurons and complex interconnection weights, in addition to the more biologically plausible real neurons and real interconnects. An adaptive three-layer neural net will be used to solve image reconstruction problems. Learning is carried out in the net to change the interconnections between neurons in different layers by using the error back-propagation algorithm [8]-[11].

The analogy and relationship between the role played by hidden neurons and that played by regularization functions in neuromorphic solutions of the image reconstruction problem in (1) will be discussed. It will be shown that hidden neurons play a certain regularization role, and that regularization functions in neuromorphic processors can be realized with hidden neurons. In the approach presented, learning enables the neural net to form automatically the regularization function $R(o)$ and the regularization parameter α, and to carry out near-perfect reconstructions adaptively and with excellent robustness.

The near-perfect reconstruction results motivate further study of object recognitions with label representations. A three-layer nonlinear net will be discussed for practical radar target identification. A novel approach to achieve perfect (100% correct) identification of three test targets utilizing realistic data collected in an anechoic chamber using scale models of actual targets will also be presented. The findings support and demonstrate the viability of the neuromorphic automated target identification first proposed by Farhat *et al.*[16] as a replacement to the traditional, but considerably less economical, approach of radar imaging.

2 Problem Formulation

For a spatially limited object function $o(r)$ and its Fourier transform $F(p)$, there exist the following well-known relationships:

$$F(p) = \int_{-\infty}^{+\infty} o(r)e^{-jpr} dr \tag{3}$$

$$o(r) = \frac{1}{2\pi} \int_{-\infty}^{+\infty} F(p)e^{jpr} dp \tag{4}$$

where the spatially limited $o(r)$ satisfies,

$$o(r) = \begin{cases} \neq 0 & \text{if } r \in [r_1, r_2] \\ = 0 & \text{otherwise} \end{cases} \tag{5}$$

The spatial frequency variable p has the dimension of inverse length $[\text{m}^{-1}]$. The spatial frequency band corresponding to the frequency band $[\omega_1, \omega_2]$ used for measurement will be denoted as $[p_1, p_2]$. When the frequency response $F(p)$ is measured at equally spaced discrete frequency points over the measurement band $[p_1, p_2]$, that is, at the frequency points,

$$p_k = p_1 + (k-1)\Delta p \qquad k = 1, 2, \cdots, N \tag{6}$$

where N is the total number of measurements taken and $\Delta p = (p_2 - p_1)/(N-1)$, the estimate of the object function by the discrete Fourier transform (DFT) algorithm (the discrete form of (4)) can be expressed as,

$$o(i) \stackrel{\Delta}{=} o(r_i) = \frac{\Delta p}{2\pi} \sum_k F(k)e^{jp_k r_i}$$

$$= \frac{\Delta p}{2\pi} \sum_k F(k)e^{j[p_1 + (k-1)\Delta p][r_1 + (i-1)\Delta r]}$$

$$i = 1, 2, \cdots, M \tag{7}$$

where $\Delta r = (r_2 - r_1)/(M-1)$ is the object function sampling interval and M the total number of samples in the object domain. The resolution of the DFT estimation is known to be proportional to $2\pi/(p_2 - p_1)$ and is insufficient for discerning object detail with spacing finer than $2\pi/(p_2 - p_1)$. Several methods for exceeding this resolution and achieving super-resolution have been studied in the past [4]-[6], but these methods suffer from certain limitations, as noted in the introduction. Reconstructing microwave radar images from data processed by minimizing an energy function of the form given in (1) through neuromorphic

processing has previously been considered [3]. Results of our continuing work on the relationship between the role of hidden neurons and regularization functions discussed in [3] are presented in the next two sections.

3   Neuromorphic Image Reconstruction

In this section we present a brief review of radar image reconstruction by neuromorphic processing [3] in order to lay the foundation for our subsequent discussion of the relation between the role of hidden neurons in layered nets and regularization functions. The function to be minimized in microwave radar imaging by neural net processing [3] has the same form as that in (1),

$$H(o) = ||F_m - F||^2 + \alpha R(o) \tag{8}$$

All quantities in (8) are the same as defined earlier. The norm defined in the complex space C is of the following form:

$$||F_m - F||^2 = \sum_{i=1}^{N} |F_m(i) - F(i)|^2 \tag{9}$$

When the Fourier transform F is expressed in terms of the object function o(r), the energy function $H(o)$ in (8) will only be a function of the variable o(r), since F_m is the known measured frequency response. After some manipulations and by assuming that the object function to be reconstructed in microwave radar imaging is real (see [3]), the following state update equation for the neuromorphic processor can be obtained:

$$o^{(j+1)}(k) = o^{(j)}(k) + \Delta o(k) + \lambda I_k \qquad 0 \le k \le M \tag{10}$$

$$\Delta o(k) = \lambda \left[2 \sum_{i=1}^{M} \Re[T_{ki}] o^{(j)}(i) - S_k \right] \tag{11}$$

where $o^{(j)}(k)$ represents the state of the kth neuron at the jth iteration; λ is defined as the gain of the kth neuron; and T_{ki} is a quantity which bears information about the transformation (here the Fourier transform) from the space $\Theta \ni o$ to the space $\Omega \ni F$. The term I_k represents the available information F_m, given by,

$$I_k = 2\Re \left[\sum_{i=1}^{N} F_m(i) K_{ik}^* \right] \tag{12}$$

where $K_{ik} = c \cdot e^{jp_i \cdot r_k}$ is the Fourier kernel and c is a constant. Equation (12) is identified as the real part of the complex object function generated by Fourier inversion of the measured

frequency response F_m. The term S_k in (11) is viewed as a regularization-related adaptive threshold, given by the following expression:

$$S_k = 2\alpha[A_{kk}o^{(j)}(k) + A_{k(k-1)}o^{(j)}(k-1) + A_{k(k+1)}o^{(j)}(k)]$$ (13)

where A_{kk}, $A_{k(k-1)}$, and $A_{k(k+1)}$ are constants [3], for a stabilizing (regularizing) function of the following form in Tikhonov's regularization method:

$$R(o) = \sum_{i=1}^{M} \left[o^2(i) + \left(\frac{o(i) - o(i-1)}{\Delta r} \right)^2 \right] \Delta r$$ (14)

or in its equivalent continuous form:

$$R(o) = \int \left\{ o^2 + [o'(r)]^2 \right\} dr$$ (15)

The neural net update transformation as expressed in (10) is carried out iteratively until the global minimum of the energy function of (8) is reached.

Microwave radar images reconstructed using the neural net processor described in (10) showed improvement over images reconstructed by DFT algorithm, when Tikhonov's stabilizing function (14) or an adaptive threshold linearly related to the neural states as expressed in (13) was used [3]. In conventional neural nets, binary neurons and nonlinear mapping of neural states are used [7]; this is largely responsible for the robust and fault tolerant collective signal processing properties of neural nets. The neural state update equation in (10) is a linear iterative equation when the threshold of linear mapping of neural states given in (13) is used; in this case, the advantage exploited in a neural net using (10) to solve the problem in (8) is only the parallel processing capability of the neural net. No use is made of nonlinear mapping. For the problem of image reconstruction in (8), multi-valued (analog) neural states have to be used to represent the bipolar object function. Therefore, in order to make the neural net processor in (10) more neuromorphic, nonlinear mapping can be introduced only via the adaptive threshold S_k. A nonlinear function of the form,

$$g(S_o) = \tanh(S_o)$$ (16)

similar to the sigmoidal function widely used in conventional neural nets [7], [8] was introduced heuristically and employed for the adaptive threshold, with S_o being a linear combination of the neural states [3]. The adaptive threshold S_k in (13) is a linear combination of the three nearest states only and S_o in (16) denotes a linear combination of possibly

many states in general. The neural state update equation in (10) can then be rewritten as,

$$o^{(j+1)}(k) = o^{(j)}(k) + \Delta o(k) + \lambda I_k \qquad 0 \le k \le M \qquad (17)$$

$$\Delta o(k) = \lambda \left[2 \sum_{i=1}^{M} \Re[T_{ki}] o^{(j)}(i) - g(S_o) \right] \qquad (18)$$

The neural net processor in (17) v as used to reconstruct one-dimensional functions (range-profiles) from measured frequency response data F_m for a sufficiently wide range of aspect angles of a scaled model of an aerospace test object. A two-dimensional object function representing a projection image of the test object was formed by coherently summing the back-projections of the one-dimensional range-profiles based on the projection-slice theorem [3], [12].

The scale model used in this study is that of a B-52 airplane. Realistic frequency response data F_m for the object were gathered for a range of aspect angles in an anechoic chamber microwave scatter measurement facility for two different frequency bands: one extending from 6 GHz to 17 GHz and the other from 2 GHz to 26.5 GHz. Images reconstructed from the two frequency bands by DFT inversion and back-projection are shown in Figs. 1(a) and (b), respectively. The image in Fig. 1(b) from the wider frequency band of 2 GHz to 26.5 GHz has a higher resolution than the image in Fig. 1(b) from the narrow frequency band of 6 GHz to 17 GHz, as would theoretically be expected. It clearly shows the double-barreled nature of the engines, a detail which is not clearly delineated in the image in Fig. 1(a). The image reconstructed from frequency response data acquired over the narrower band (6 GHz to 17 GHz) using the neural net processor expressed in (17) with the nonlinear threshold mapping function given in (16) is shown in Fig. 1(c); this image has nearly the same resolution as the image reconstructed over the band from 2 GHz to 26.5 GHz and the double-barreled nature of engine is once again clearly delineated. The image quality obtained using the neural net processor expressed in (10) with the linear threshold mapping function is inferior to that in Fig. 1(c), indicating the importance of incorporating nonlinearity [3]. These results demonstrate the high resolution capability of nonlinear neural nets in image reconstructions.

4 Relationship Between the Role of Hidden Neurons and Regularization Functions

The neural net processor expressed in (17) is basically of the Hopfield variety [7]. It works iteratively until a stable state of the net is reached to give a solution for the image reconstruction problem of (8). The iterative process can be implemented by a parallel feedback loop [3] in which the net's new state is obtained by the feedback of the state change $\Delta o(k)$ computed from the neural state for the preceding iteration (see schematic Fig. 2(a)). The computation of $\Delta o(k)$ can be implemented by a subnet with one hidden layer of neurons as shown in Fig. 2(b). By comparing (17) with Fig. 2(b) it can be noted that the hidden layer neurons implement the nonlinear adaptive threshold related to the regularization function. Thus, the weights (or synaptic connections) used for the adaptive threshold can be combined with other weights that directly connect the input layer with the output layer, if the adaptive threshold is a linear mapping of neural states like that shown in (13). In this case, the neural net update equation (10) can be rewritten as:

$$o^{(j+1)}(k) \;=\; o^{(j)}(k) + \Delta o(k) + \lambda I_k \qquad 0 \le k \le M \tag{19}$$

$$\Delta o(k) \;=\; 2\lambda \sum_{i=1}^{M} \left[\Re[T_{ki}] - \alpha \delta_{kk} A_{ki} - \alpha \delta_{(k-1)i} A_{ki} - \alpha \delta_{(k+1)i} A_{ki} \right] o^{(j)}(i) \tag{20}$$

where δ, is the Dirac delta function. On the other hand, the total connections implemented from the input layer through the hidden layer to the output layer in Fig. 2(b) can not be combined with other direct connection weights from the input to the output layers. This demonstrates the necessity of implementing an adaptive threshold representing a regularization function in nonlinear neural nets with a hidden neural layer.

The relationship between the role of hidden neurons and regularization functions can also be appreciated by examining the regularization role played by hidden neurons. Hidden neurons are used to generate internal representations in neural networks and to extend the computational (or mapping) power of simple two-layer associative networks [8]. In simple two-layer associative networks, input patterns at the input layer are directly transformed (or mapped), through the synaptic connections between neurons, into output patterns at the output layer. No internal representations by hidden neurons are involved in such a network. Because of this direct mapping property, simple networks will transform input patterns of similar structure into output patterns of similar structure; consequently, such network will not be able to yield mapping outputs that are quite different when the inputs

input pattern	output pattern
00	0
01	1
10	1
11	0

Table 1: XOR Mapping

are quite similar (or vice versa). A classic example of this situation, that has been discussed by other researchers [8], is the exclusive-or (XOR) problem illustrated in Table 1.

In this example, the inputs (for example, 00 and 11), which are quite different, are to be mapped into the same output (for example, 0). If two neurons in the input layer are used to represent the two input bits and one neuron in the output layer is used to represent one output bit in a simple two-layer network, it is impossible to find a set of weights and thresholds for all the neurons that would perform the desired mapping [13]. Complications in applying a simple two-layer net without hidden neurons to the XOR mapping problem arise in mapping quite different patterns (11 and 00) to identical output (0), as well as in mapping quite similar patterns (01 and 10) into identical output (1). Such pair of mappings are quite contradictory and, by definition, are ill-posed. (For example, in inverse scattering, the mapping (inverse) is known to be ill-posed if the solution of the mapping or reconstruction does not exist or is sensitive to noise in the input data.) In the XOR problem in a two-layer neural net, a network to perform the mapping cannot be found; thus it is an ill-posed problem since no solution for the problem exists.

On the other hand, a layer of hidden neurons inserted between the input and output layers of a simple two-layer network will enable the network to perform arbitrary mapping from input to output via the hidden neurons, if an adequate number of hidden neurons are utilized [8], [13]. It can easily be verified that the network with a single hidden neuron shown in Fig. 3 can perform the XOR mapping mentioned above. This network overcomes the difficulty encounted in a 2-layer net by using a hidden neuron to change the quite different input patterns into patterns with *sufficient similarity* as seen by the output-layer neuron: it accomplishes the task by using one hidden neuron for a two-bits to one-bit mapping. The required weights of synaptic connections among the neurons, indicated in Fig. 3 by

the number on the arrows, are ultimately determined through learning (see, for example, [8]-[11]). The numbers in the circles represent the required thresholds of the neurons, which are assumed here to be fixed. All the neurons in the net are assumed to have only two states: on (1) or off (0). The hidden neuron has output 1 (on) only when both input neurons have states 1; otherwise it has output 0 (off). The output neuron will be turned on when it has a net positive input greater than 0.5; the output neuron will be turned off (net input smaller than 0.5) by the hidden neuron output through the synaptic connection weight of -3.0 when both input neurons are on. From the point of view of the output neuron, the inputs to it are quite similar when the input neurons are on (11) or off (00). Thus, the role of the regularization or constraint function played by the hidden neuron is to change the degree of similarity among the input patterns corresponding to the same output pattern. This role can be considered to be the same as that of regularization functions for ill-posed problems.

The regularization role played by hidden neurons can also be appreciated from the error back-propagation (EBP) algorithm, in which hidden neurons are used [8]-[11]. The EBP algorithm for a general problem is also formulated so as to minimize the error energy function,

$$E = ||O - \bar{O}||^2 \tag{21}$$

where $\bar{O}$ is the specified or the desired output and O is the output of the network for a given input. For the given input and the specified output, the error signal given by E is fed-back (or back-propagated) into the network to adjust the interaction weights (weights of synaptic connections) among all neurons, including hidden neurons. This learning procedure is iterated until a set of weights is arrived at for which the specified output, or equivalently, the specified minimum of the energy function, is reached. Comparison of the energy function in (8) with that in (21) shows there is no regularization operation involved in (21). It is well known that inversions by minimizing the error energy function of the form shown in (21) in the presence of noise are ill-posed and that the outputs are usually not stable with respect to the inputs. From our simulation results obtained by networks with hidden neurons, it is found that the performance of the networks is quite robust with respect to inputs. This demonstrates further that the role played by the regularization operator in (8) to constrain the output in ill-posed mapping problems is achieved using the hidden neurons in neural networks. Impossible mappings in a neural network can be made possible by increasing

10

the number of hidden neurons; this can be explained by the fact that regularization is introduced or further enforced by the increase in number of hidden neurons.

5   Reconstruction by Neural Nets Through Learning

The iterative neural net equation (10) can be cast in a closed form of a non-iterative equation and implemented with a non-iterative processor when an adaptive threshold (13) that is a linear function of neural states is used. On the other hand, when an adaptive threshold (16) that is a non-linear function of neural states is used, the iterative neural net equation (17) can not be written in the closed form of a non-iterative equation. There is no known method to directly implement the iterative equation with a non-iterative processor; this results from the difficulty of choosing a different regularization $R(o)$ and a different parameter α in (8) for a different reconstruction problem, since the first term on the right hand side of (8) can be computed with a non-iterative DFT processor. This difficulty can be overcome by a neural net through learning that enables formation of $R(o)$ and α automatically, depending on the image to be reconstructed.

Hidden neurons have been shown to have a regularization effect in last section. Hence a hidden neural layer will be used here for the purpose of regularization. overcoming the ill-posedness of image reconstruction from partial frequency response. A three-layer neural net with feedforward connections for image reconstruction is schematically shown in Fig. 4. The input layer takes the frequency responses from measurements, and complex neurons (i.e., their states are complex and equal to the real and imaginary values of the measured complex frequency response) in the input layer are connected to neurons in both the output layer and the hidden layer. The synaptic connection of neurons in the input layer to neurons in either the output layer or the hidden layer are complex and will be fixed and taken as the Fourier weights for the image reconstruction problems in situations in which the measurement data and the image to be reconstructed have a Fourier transform relation. The number of neurons in all three layers are assumed to be the same, for the moment, and to equal the number of frequency points at which the response is measured. Images to be reconstructed are assumed to be normalized to unity and the output from neurons in the hidden layer will take a nonlinear function of the form $\tanh(\cdot)$. Mathematically, the final

11

output neural state representing the image to be reconstructed is,

$$o(i) = z(i) + \tanh\left[\sum_j r_{ij} z(j)\right] \qquad (22)$$

where r_{ij} is real-valued synaptic link between the ith neuron in the output layer and the jth neuron in the middle (hidden) layer and,

$$z(l) = \Re\left[\sum_{k=1}^{N} W_{lk} F_m(k)\right] \qquad l = i, j \qquad (23)$$

where $\Re[\cdot]$ represents the real part of the bracketed quantity and W_{lk} are the Fourier weights. Once more, a real object function $o(i)$ is assumed for microwave radar imaging [3]; and $z(l)$ is recognized as the real part of the Fourier inversion of the measured frequency data F_m.

Learning in the neural net involves determining the synaptic weights r_{ij} by an error back-propagation algorithm [8]-[11]. With an error back-propagation algorithm, the neural network can be made to learn, under supervision, to perform extrapolations and reconstructions as follows: for a given desired or ideal object function D, when the measured frequency response $F_m(p)$ is fed into the network in Fig. 4 and the output from the network denoted as o, an error function,

$$E = ||D - o||^2 = \frac{1}{2}\sum_i |D(i) - o(i)|^2 \qquad (24)$$

can be defined. Since knowledge of the desired object function D at the output of the net is required (D is also the ideal desired image at the output), the learning is supervised. Using the chain differentiation rule, the change of the error function with respect to the change of weight r_{ij} can be written as,

$$\frac{\partial E}{\partial r_{ij}} = \frac{\partial E}{\partial o(i)} \cdot \frac{\partial o(i)}{\partial r_{ij}} \qquad (25)$$

From equation (24),

$$\frac{\partial E}{\partial o(i)} = -[D(i) - o(i)] = -\delta_i \qquad (26)$$

and from equation (22),

$$\begin{aligned}
\frac{\partial o(i)}{\partial r_{ij}} &= \tanh'\left[\sum_j r_{ij} z(j)\right] z(j) \\
&= z(j)/\cosh^2\left[\sum_j r_{ij} z(j)\right] \qquad (27)
\end{aligned}$$

Combining now (25), (26) and (27), the following equation is obtained,

$$\frac{\partial E}{\partial r_{ij}} = -\delta_i z(j) / \cosh^2\left[\sum_j r_{ij} z(j)\right] \qquad (28)$$

To reduce the error signal in (24), the weight r_{ij} can be changed through gradient descent by an amount,

$$\Delta r_{ij} = \eta\left(-\frac{\partial E}{\partial r_{ij}}\right)$$

$$= \eta \delta_i z(j) / \cosh^2\left[\sum_j r_{ij} z(j)\right] \qquad (29)$$

with η being a constant controlling the learning rate.

The above procedure is for one given object (or pattern) function D. When there are M ideal images of interest, the procedure is carried out M times, once for each image. For each image the error signal is checked and if a specified error criterion (to be specified below) is not satisfied, the procedure is repeated again for every pattern; this is done repeatedly until the error signal criterion is satisfied for each image.

6   Simulation Results and Robustness Tests

Simulations were carried out to verify the learning concept presented above. Several ideal object functions of spatial extent within [0,4] cm are used. The number of neurons for the input, middle, and output layers are assumed to be equal to 21 for each layer. The small number of neurons used and the small extent ([0,4] cm) of the function occupied are all chosen for the purpose of containing the computations involved, but they can be increased or altered at will to any desired value. The frequency response of the object function chosen is synthesized (computed digitally) in the 6-17 GHz range and subjected in simulation to the action of the network in Fig. 4. The network can determine a set of r_{ij} links for a given set of functions to produce correct patterns within the specified error criterion $\max_i |D(i) - o(i)| < 0.097$.

For one of our simulations, done for a set of two object functions, the first object function is,

$$o_1(r) = \begin{cases} 1.0 & r \in [0.2, 1.2](\text{cm}) \\ 0 & r \in [0, 0.2)(\text{cm}) \text{ or } r \in (1.2, 4.0](\text{cm}) \end{cases} \qquad (30)$$

13

The second is,

$$o_2(r) = \begin{cases} 1.0 & r \in [2.2, 3.2](\text{cm}) \\ 0 & r \in [0, 2.2)(\text{cm}) \text{ or } r \in (3.2, 4.0](\text{cm}) \end{cases} \tag{31}$$

These two functions, shown in Figs. 5(a) and (b), respectively, have spatial extents within 0-4 cm. The frequency responses of the two object functions synthesized over the frequency window 6-17 GHz are shown in Figs. 6(a) and (b), respectively. If the DFT inversion method is applied to the frequency data in Fig. 6, a low resolution image with most of its intensity concentrated around the sharp edge of the object functions will be obtained because of the relatively high frequency window. Fig. 7 shows the reconstruction of the first object function from the partial frequency domain data in Fig. 6(a) by the DFT method. This reconstruction shows that there is a relatively broad positive pulse at the position of the rising edge of the original object function and a broad negative pulse at the position of the falling edge of the original object function; the two pulses are of different amplitude even though the given object function has the same rising and falling edges. When the two object functions are alternately presented to the network in Fig. 4 and the synaptic connections are changed according to (29), the learning process gradually converges and a set of synaptic connections is learned by the network, enabling it to provide near-perfect reconstructions of the object functions within the specified error criterion when the frequency response of either object function is presented to the network. The network accomplishes the learning in just five learning cycles, defined as the process of presenting the two patterns to the network once and modifying the weights following each pattern presentation.

Figure 8 shows the outputs of the network for several typical learning cycles and demonstrates how the network gradually learns the two patterns by adjusting its connection weights. Shown in Fig. 8(a) are the outputs of the network for the first pattern (left side) and for the second pattern (right side) after the network has been trained with the first pattern only during the first learning cycle. It is seen from Fig. 8(a) that the output from the network for the first pattern as input is near-perfect and the output for the second pattern as input resembles more the first pattern rather than the second; this is understandable, since the network has as yet learned only the first pattern. Completing the first learning cycle by training the net next with the second pattern, we find the network is able to give a near-perfect reconstruction of the second pattern as input (right side, Fig. 8(b)). When the first pattern is presented, the output is altered, becoming more like a superposition of the first pattern and the second pattern. This occurs because, during the learning

of the second pattern, the network loses some of its previous internal representation of the first pattern. The internal representation of the first pattern is restored, however, in the second learning cycle following the presentation of the first pattern again to the net. The output (left side, Fig. 8(c)) from the network for the first pattern as input again approaches a near-perfect reconstruction and the output (right side, Fig. 8(c)) for the second pattern as input is much better than that obtained during the first learning cycle (right side, Fig. 8(a)). This result is also understandable since, so far, the network has been trained with the first pattern twice (during the first and second learning cycles) and with the second pattern once only (during the first learning cycle). The output for the second pattern (right side, Fig. 8(d)) is improved during the second learning cycle after presenting the second pattern to the network for learning; once again, this degrades the performance of the network in recognizing the first pattern (left side, Fig. 8(d)). By repeatedly and alternately presenting the two patterns to the network for learning, the network gradually adjusts its interconnection weights to improve the reconstructions for both patterns. Shown in Figs. 8(e) and (f) are the outputs of the network during the third learning cycle after the first and second patterns have been presented to the network, respectively; the performance of the network is seen to have improved in comparison with the corresponding cases in the second learning cycle. After the first pattern has been presented to the network for learning during the fourth learning cycle, the outputs for both patterns are much better (Fig. 8(g)), except for the presence of some side lobes for the second pattern as input (right side, Fig. 8(g)). The side lobe level is reduced to the specified tolerable error range of $\max_i |D(i) - o(i)| < 0.097$ during the fifth learning cycle. Fig. 8(h) shows the outputs of the network for both patterns after the network has been presented with the first pattern for learning during the fifth or the final learning cycle.

How to choose the learning rate η is critical to the speed of the learning process. The range of suitable learning rates can be analytically determined for learning algorithms involving a linear function of neural states [14]. For the learning algorithm involving a nonlinear function of neural states given in (29), it is, however, hard to analytically determine the range of the learning rate. By inspecting (29), it is seen that the learning rate η represents the proportion by which the synaptic weight changes in accordance with the output error induced by the current synaptic weights themselves. In our preceding simulations, the learning rate chosen is usually $\eta = 0.99$. As indicated elsewhere, it would not make sense to have the learning rate η greater than 1, since this could "overcorrect" output error [14] — a

phenomenon that has been observed in our simulations. By "overcorrection", we mean that the output error (energy) being minimized exhibits oscillations and sometimes is increased. Overcorrection usually results in a longer convergence time. On the other hand, making the learning rate too small could also slow down the learning process. Another cautionary remark in carrying out the learning process is that the initial synaptic weights should not be equal; otherwise, the network would obtain identical weights for all synaptic connections [8]. The initial synaptic weights in our study were chosen randomly.

More complex-shaped object functions were also used to test the learning and reconstruction capability of the neural net in Fig. 4. A set of two object functions is shown in Fig. 9. The first function has a spatial extent of 0.2-0.8 cm (Fig. 9(a)) similar to that shown in Fig. 5(a). The second function is of a more complicated shape. The first part of this function is a pulse of 0.8 cm in width and the second part is of a triangular shape. After a set of synaptic weights is learned by the network by presenting the two patterns to the net five times, the network is able to give a near-perfect reconstruction when the frequency response of either function is presented to it. The reconstructions of the two object functions by the network are shown in Fig. 10. Comparing Fig. 10(b) and Fig. 9(b) shows that the reconstruction of the triangular portion of the second object function is perfect; since the triangular part of the second function resembles more the undulations of a continuous function, its perfect reconstruction implies the network performs better for continuous functions.

Generalizations and Robustness: The two simulations presented above have shown good results when the network is used for reconstructions of object functions that it has been presented with during the learning process. Generalization, which deals with the performance of a network when inputs are similar to, but not specifically among, the training sets the net has been presented with during the learning process, is an issue of practical importance [14]. Generalization for extrapolations and reconstructions from partial frequency information is studied here from the point of view of the network's performance with noise-contaminated frequency response input data.

Based on the discussion in Section 4, it can be appreciated that hidden neurons play a certain regularization role, and that such regularization makes the solution stable for problems of extrapolations and reconstructions from partial frequency information. Numerical simulations were conducted to verify that the network with hidden neurons in Fig. 4 provides sufficient regularization and is capable of giving stable and robust reconstruc-

tions even in the presence of noise. One of these simulations was done with the test object functions shown in Fig. 5. The frequency responses of the two object functions in Fig. 5 were contaminated with Gaussian noise with the following distribution function,

$$G(N) = \frac{1}{\sqrt{2\pi}\sigma} e^{-N^2/(2\sigma^2)} \tag{32}$$

where N represents the noise amplitude, and σ^2 is the variance of Gaussian noise. Defining the signal-to-noise ratio (SNR) as,

$$\text{SNR} = \frac{\text{average signal energy in the given frequency band}}{\text{noise variance}}$$

$$= \frac{1}{p_2 - p_1} \int_{p_1}^{p_2} |F(p)|^2 dp / \sigma^2 \tag{33}$$

we find that when SNR=5, the noise-contaminated frequency responses for the two object functions are as shown in Fig. 11 for the frequency band 6-17 GHz corresponding to $p \in [2.5, 7.1](\text{cm}^{-1})$. The difference before and after noise contamination can be seen by comparing Fig. 6 and Fig. 11. Even though the frequency responses in Fig. 11 after noise contamination differ appreciably from the noise-free frequency responses in Fig. 6, the network, which learned a set of synaptic connections using the noise-free frequency information, is still able to yield reconstructions of high quality, as shown in Fig. 12. The reconstructions in Fig. 12 from the noise-contaminated frequency information show a weak side-lobe structure compared with the reconstructions in Fig. 8(h), where noise-free frequency information is used as input. When the SNR is further decreased, the side lobe structure in the reconstructions from noise-contaminated frequency information will increase. The reconstruction from noisy frequency response data can be improved by training the network with noise-free, as well as some noise-contaminated frequency data. For studies with the two test patterns considered here, the network was trained with the noise-free frequency data shown in Fig. 6, and also with the noisy frequency responses (SNR=1) shown in Fig. 13. The ideal patterns needed in the supervised learning process for the noise-free and noisy data were specified to be the same as those shown in Fig 5. The noise-free data and the noisy data were presented alternately to the net to adjust the connection weights until the specified error criterion $\max_i |D(i) - o(i)| < 0.007$ for every pattern was reached. When the resulting network is tested using noisy frequency response data (SNR=5) as input after the stated training, the outputs from the network are as shown in Fig. 14. Comparing Fig. 14 with Fig. 12 shows a clear improvement of the side-lobe structure, the result of mixing instances of noisy and noise-free data sets in training the network. In practice, a network,

being trained with examples of data from its environment, is expected to encounter differing levels of SNR. The findings above suggest that this could be beneficial for enhancing the performance of the net.

7 Radar Target Identification by Layered Networks

The preceding discussion shows that robust extrapolation and near-perfect reconstruction can be achieved with layered nonlinear networks. An interesting issue is whether there always exists a network that can do extrapolations and reconstructions for a given finite number of functions or patterns of interest. A theorem concerning multi-layer neural networks, which simply states that a multi-layer network with sufficient number of hidden neurons is able to perform any kind of mapping from input to output [8],[15], makes it possible for the network shown in Fig. 4 to perform extrapolations and reconstructions of any finite number of functions of interest, if enough hidden neurons are used in the network. For a finite number of aerospace targets, a two-dimensional object function describing the geometrical shape of each target can be formed from the one-dimensional functions recon- structed by a learning net, as described in the last section, through extrapolation of partial frequency response data acquired for fixed aspects of the targets over a sufficiently wide range of aspect angles [3]. The two-dimensional image obtained in this fashion can provide sufficiently high resolution through data acquisitions over a wide range of aspect angles and extrapolations of the measured frequency response data for every aspect. Such high resolution images, like those shown in Fig. 1, would enable a human observer to recognize and identify the target. Another more attractive and less involved concept in target iden- tification does not involve forming an image. It provides for target identification from an identifying label of the target generated by a neural net automatically from input informa- tion (i.e., frequency response data) belonging to that target [16]. This approach is necessary in situations where aspect information (frequency response echos for various aspects) of the target can not be obtained over a sufficiently wide range of aspect angles because of prac- tical limitations and a high-resolution image of the target consequently can not be formed [16]. The issue then is that of radar target identification from a single frequency response echo for any practical aspect of the target, or a few such echos, using a layered nonlinear network through self-organization and learning.

The traditional approach in nonimaging radar target recognition has been to extract

from suitably formed radar echos characteristic features or signatures of the targets and to compare these with a library of such signatures [17]. This kind of approach is basically a parametric estimation method and makes certain assumptions about the form of the return signals or echos as expressed by several parameters. The extraction of the assumed parameters used in the approach is usually sensitive to noise [18] and there is no adaptation involved.

The network used for target recognition in our work is shown in Fig. 15. This network is a variation of the network used in Fig. 4 for extrapolations and reconstructions. In the network in Fig. 4, which was shown to be robust in extrapolations and reconstructions from partial information, the number of output neurons was equal to the number of samples representing the function to be reconstructed. In the network shown in Fig. 15, intended to perform robust target recognition from partial information, the number of output neurons is chosen to allow forming enough distinguishable labels to represent all targets of interest. Using labels instead of object functions makes learning easier, since the ideal object functions that are needed to accomplish learning for extrapolations and near-perfect reconstructions, and that are not easy to obtain for aerospace targets in general, are now not required. Since label representations rather than object functions of targets are to be used for identification in this case, no direct connections between output neurons and input neurons in Fig. 15 are used, this simplifying the structure of the network. As before, the connections from input neurons to hidden neurons accomplish Fourier mapping, i.e.,

$$z(j) = \Re[\sum_{k=1}^{N} W_{jk} F_m(k)] \tag{34}$$

where W_{jk} represents the Fourier weight for inverting the known (measured) partial frequency domain information $F_m(k)$. For target recognition from other than frequency domain information, the weights W_{jk} are set up in accordance with the applicable transform, or else they are determined through training. The input to an output neuron in Fig. 15 is given by,

$$u_i = \sum_{j} r_{ij} z(j) \tag{35}$$

where r_{ij} again represents the weight from neuron j in the hidden layer to neuron i in the output layer to be determined by learning. The output neuron state is now given by the

expression,

$$o(i) = U[\tanh(u_i)] = \begin{cases} 1 & \text{for } u_i > 0 \\ 0 & \text{for } u_i < 0 \end{cases} \quad i = 1, 2, \cdots, M \tag{36}$$

where $U[\cdot]$ is the unit step function. The form $U[\tanh(u_i)]$ is used in (36) to show more clearly the nonlinear summation input to the output layer, as well as the evolution of the circuit in Fig. 15 from that of Fig. 4. Different targets are represented by different output states.

Two groups of test targets were used in our study: the first group contains a 100 : 1 scale model of a B-52 aircraft and a 150 : 1 scale model of a Boeing 747 airplane; the second group contains a 75 : 1 scale model of a space shuttle in addition to the two scale models in the first group. Sketches of all three scale models with their actual dimensions are shown in Fig. 16. It can be noted that the shapes of the Boeing 747 and the space shuttle are relatively less complex than that of the B-52 airplane. Two output neurons are used to provide label representations for the three aerospace target models; two output neurons can usually provide labels for 2^2 (= 4) distinct patterns. The state (0,0) of the output neurons in the network shown in Fig. 15 is left idle to indicate the case in which there is no information input to the network.

For practical applications of radar target identification, it would be necessary to examine the performance of the network for all possible aspects of the target that could be encountered by the observer (the radar system), a process that entails massive data collection and storage. Because of the limitations of our experimental facility, frequency response data for the targets are collected for only a limited range of aspect angles extending over a range of 20° in azimuth from a head-on (0°) view of the targets to 20° towards the broad-side view of the targets. The elevation angle of the target was fixed at 15° relative to the horizontal. The results obtained with this limited data set are, however, quite telling and representative of what can be expected with larger libraries of frequency responses covering all target aspects of interest. Frequency domain data are collected for 100 aspect views equally spaced over the 20° range for each target, representing a separation of 0.2° between adjacent views.

The network in Fig. 15, designed for target identification, was first presented with frequency response data from a certain percentage of the 100 aspect views of the targets to allow learning to take place. Each target is assigned a label: (0,1) for the B-52; (1,0) for the Boeing 747; and (1,1) for the space shuttle. A total of 101 frequency points were collected over the band 6.5-17.5 GHz for each aspect view; the number of neurons chosen

20

in the input and hidden layers was also 101. Learning is carried out via the error back-propagation algorithm described in Section 5. which enabled adjusting the connection weight r_{ij} between the output neuron and the hidden neuron. When the frequency response of a target for a specific aspect angle is presented to the network, the network iteratively adjusts the weight r_{ij} by error back-propagation until the desired label for the target is produced by the network. The training data (frequency response for different aspects or views) are presented in turn to the network for each target; all targets of interest are learned by the network in turn. The process of presenting all the training data for all targets once constitutes one learning cycle. The maximum number of iterations required for the network to learn specific targets of the types used in our study was 7 at the start of the learning process , but this number decreased as learning progressed or as the number of learning cycles increased. Once the network has assimilated and learned the correct representations for all targets, the learning process is terminated. The maximum number of learning cycles observed for the network to learn all targets was 8.

Fig. 17 shows the performance of the network for the first group of targets, the B-52 and the Boeing 747 scale models. The curves in Fig. 17 indicate the probability of correct recognition by the network of the two targets with respect to the percentage of the total 100 aspect views collected that were used for training. The training set can be selected deterministically, i.e., in a given order, or randomly from the set of 100 aspect views characterizing each target. The criterion for choosing the training set is to make sure that information about the target is evenly represented. For example, the deterministic selection case of 50 percent of the available aspect views as the training set can be formed by selecting every other aspect view, i.e., all the even- (or odd-) numbered views out of the total 100 available aspect views. For the random selection case, the training set can be formed by selecting aspect views out of the total angular window of 20° with even probability. Our study shows that the performance of the network is virtually unaffected by the method of selection for the training set and at most a 1% discrepancy in results for the two methods of selection is observed. In order to test the performance of the network after it has been trained. all 100 aspect views are used. While a certain percentage of the test set would have been used in training the network. the remainder of the test set would not have been seen by the network before. When 10% of the total available views, or equivalently, when views with roughly 2° angular separation are used for training, the network achieves only 54% correct recognition for the B-52 and 72% for the Boeing 747. even though the incremental

21

spacing between viewing angle for the given set of data is small (0.2°). The performance of the network improves nonlinearly as the percentage of views used for training is increased. Because the shape of the Boeing 747 is less complex than that of the B-52, the network is able to capture its underlying structure in its internal representation (the r_{ij} weights) much faster, allowing for better recognition. The network reaches 90% correct recognition, when the percentage of views used for training increases to 40% for the B-52 and 20% for the Boeing 747, or when the minimum angular spacing between adjacent views in the training set is approximately 0.5° for the B-52 and 1° for the Boeing 747. When the percentage of views used for training for both targets increases to 60%, the network can recognize more than 98% of the testing aspect views presented to it correctly.

For the network shown in Fig. 15, with the connection weights from the input layer neurons to the hidden layer neurons fixed as Fourier weights, the input to the hidden layer can be interpreted as the real part of the Fourier inverse of the measured frequency response data F_m for one aspect view. This input (range-profile) to the hidden layer bears information such as the rough extent, shape, fine structure, etc., of the target as seen from that aspect angle [3]. During training, the network extracts common features or certain correlations from the training data to form a representation for the target by adjusting its weight r_{ij}. When the network is tested with test views, the portion of the test views which have not been presented to the network during training can be considered as noisy versions or "correlates" of the training set. This ability of the net to generalize, i.e., to recognize noisy or correlated data, is an attractive feature of neuromorphic signal processing. The range-profile data in various aspect views of a complex aerospace target can differ noticeably from one aspect angle to another. In fact, since the data in various aspect views for complex shaped aerospace targets change markedly from one aspect angle to another, the resemblance or correlation of adjacent views for some aspect angles are so weak, even for the angular spacing of 0.2° used in our data acquisition, that the network fails to recognize the targets perfectly (with a 100% score) even when almost all the views are used for training; this is evident in Fig. 17 by the fact that correct recognition for both targets did not reach 100% until 100% of the available aspect view data were used for training. The results plotted in Fig. 17 show that the average probability of misrecognition from a single-aspect view when 60% or more views have been used for training is 1%.

Perfect Recognitions: The probability of misrecognition can be made negligible and even reduced to zero in two ways. One way which we describe here is to use more than

one aspect view for a given target in interrogating the network, with the outcome decided by a majority-decision rule. The multi-aspect views for recognizing aerospace targets in a practical target identification system could be readily collected and presented to the network as targets fly by the system. The training procedure for recognition from multi-aspect views remains the same as that used for recognition from a single-aspect view.

Fig. 18 shows the performance of the same network of Fig. 15 in recognizing the first group of targets from three, rather than one, aspect views after the network has been trained with the available training set of aspect views. The three aspect views are randomly selected from the test set (100 views) and are sequentially fed into the network; the outputs from the network provide the three labels from which a majority vote on the recognition outcome can be determined. There were 33 groups of three aspect views randomly formed from the total 100 aspect views thus ensuring that almost every aspect view is included in the test. Fig. 18, which displays the correct recognition percentages with respect to these 33 groups, shows that the overall performance of the network improves by a factor of about 10% when using three views rather than a single view for interrogation. The correct recognition performance increases much faster as the percentage of the views used for training increases. The network now reaches 100% correct recognitions when 25% of the views for the Boeing 747 and 35% of the views for the B-52 are used for training. The network was also tested with the second group of targets which was formed, as mentioned earlier, by adding a space shuttle scale model to the first group of targets. The network was trained similarly using a certain percentage of the total available aspect views from all three targets. Fig. 19 shows that correct recognition performance of the network for the space shuttle is similar to that for the Boeing 747. From a practical standpoint, it makes more sense to evaluate the performance of the net by using multiple aspect views as test signals combined with a majority vote when the three aspect views are successive or adjacent to each other rather than being distributed over a wide range of aspect angles. This is representative of situations where the net is probed with three successive frequency responses collected from a target as the target changes its aspect relative to the measurement system because of relative motion. In our study, the performance of the network, when the three aspect views are successive or adjacent to each other, was found to be similar to the cases shown in Fig. 19 in which the three aspect views are randomly selected. Recognition using multi-aspect views may be supported by biological vision systems in which multiple perception fields are formed [19].

The second approach for reducing the misrecognition probability, which we only mention here, is to use multisensory information for both training and interrogation. Polarization-sensitive sensors can, for example, be used to measure the frequency response of the target for orthogonal polarization. Data generated in this fashion can be used for both training and interrogating the network to enhance the probability of correct classification.

Dynamic Range and Noise Considerations: One issue that should be mentioned with respect to neural networks concerns the dynamic range of input signals to the network. In applying neural networks to practical problems, it is usual to use binary digital inputs [7] or normalized inputs [21]. The range of inputs to the network shown in Fig. 15 is not constrained (i.e., it is neither binarized nor normalized); it is the raw frequency response of the target measured for a given aspect corrected for range-phase and measurement system response [3]. The network can be trained and tested with signals of arbitrary amplitude. No normalization is needed for preprocessing. For example, this network, which was trained with a set of aspect views with a maximum amplitude of 0.5 (arbitrary units) for the B-52 airplane, would yield the same result when interrogated with test sets of aspect views of maximum amplitudes of either 1 or 10^6 (arbitrary units). This practically significant behavior, which we attribute to the highly nonlinear nature of the network (see equations (35) and (36)), indicates that there is little constraint on the dynamic range of the test signals applied to the trained net.

A second issue concerns the network's performance with noisy data. Data in our study, which were collected in an experimental imaging facility, had a SNR of about 15-20 dB. The network was also tested with signals having a smaller SNR by adding to the test data artificial Gaussian noise in accordance with the distribution shown in (32). This situation was taken to be a crude representation of cases where the test data are collected under non-ideal situations, such as when vibrations and wind buffeting against an aircraft produce noisy frequency response measurements. The training data used were still the original frequency response data collected in our anechoic chamber measurement facility with no additional noise added. Fig. 19 shows that the network is able to perform 100% correct recognition of the three test targets when the network was trained with 40% of the available aspect views and tested with the test set of experimental data without additional noise added. During the training process, the output was mapped from the input as shown in (36). When noise was added to the test set to test the network trained with 40% of the aspect views of experimental data, the performance of the network was as given in Table

SNR	1	2	3	4	5	6	7	8	9	10
$\theta = 0$	74	78	85	88	91	93	95	97	100	100
$\theta = 0.1$	94	100	100	100	100	100	100	100	100	100

Table 2: Percent correct recognition of Boeing 747 for two different values of the threshold θ.

2 by the row beginning with $\theta = 0$ for the Boeing 747 plane. The performance of the network for the other two target models was found to be generally similar and is therefore not shown. It is seen from Table 2 that the performance of the network deteriorates as SNR decreases, but the network is still able to furnish 74% correct recognition even with SNR=1 (i.e. SNR=0 dB). The performance of the network in the presence of this severe noise case can be improved by changing the zero threshold in (36) to a finite threshold during the training process, and by maintaining the zero threshold during the test or interrogation stage. In this case, the output neuron state in (36) during the training process was replaced by,

$$o(i) = \begin{cases} 1 & \text{for } \tanh(u_i) > \theta \\ 0 & \text{for } \tanh(u_i) < -\theta \end{cases} \tag{37}$$

where θ represents the threshold. The output neuron state during the test process is still given by (36) or by $\theta = 0$ in (37). The performance of the network in recognizing the Boeing 747 scale model for $\theta = 0.1$ in (37) is shown in the last row in Table 2; the network was trained with 40% of the available aspect views with no additional noise added. The improvement in performance resulting from the finite threshold can be readily noted; in the low SNR range an improvement of roughly 20 percentage points is achieved. As the threshold θ increases, the performance of the network with respect to noisy data improves. But in situations where the noise is severe, such as SNR=1, it is hard to achieve perfect recognitions, since thresholding becomes less effective.

Effect of Spectral Windows: All results presented above are for frequency response data collected over 6.5-17.5 GHz band for 101 points. A question of practical importance is whether fewer data points or a narrower spectral window can be used to facilitate the data acquisition process without sacrificing target identification ability by the trained net. We used several approaches to assess the effects of spectral bandwidth and the number of

data points over the band on the performance of the network in identifying the given target models. One way was to keep the spectral band fixed at 6.5-17.5 GHz and decrease the number of data points over the band; this is equivalent to changing the sampling interval of the frequency response data. In so doing, the number of neurons in the input layer, which represents the number of data points in each measured frequency response, is decreased along with the number of hidden neurons which is equal to the number of neurons in the input layer. Another approach was to keep the sampling interval unchanged and to choose a portion of the 6.5-17.5 GHz band as the new spectral band, which again decreases the number of neurons in input layer. In this case, the location of the selected spectral band was found to have little effect on the performance of the network. In all of the above cases, the following behaviors were observed: (a) When the number of data points and the number of neurons in the input layer representing the input data points to the net is decreased, either by changing the sampling interval or by choosing a smaller spectral band, the number of learning cycles required by the net increases; this may be explained by the fact that for every target, the amount of information in the data sets presented to the net during training is reduced as the number of input data points is decreased; thus, it takes relatively longer for the net to learn the underlying structure in the data presented to it and to form internal representations of the targets. (b) When the number of input data points to the net is too small, the net cannot learn or form the internal represe: _tions. The learning process does not converge. The minimum number of data points for which the learning process diverges is 17, the integer closest to 101/6 and the factor by which the sampling interval of the frequency data over the band 6.5-17.5 GHz was increased. (c) When the number of input data points to the net is decreased, the performance of the net generally deteriorates; the average percentage of deterioration is 5%, with no clear pattern of deterioration. For example, when the frequency band was reduced to 10.5-15.9 GHz, over which there were 50 data points, and 40% of the available 100 aspect views (frequency responses) over this band were used for training the net, the net's performance in recognizing Boeing 747 is 94%. This can be compared with the results shown in Fig. 19 in which the net was able to achieve 100% correct identification of the Boeing 747 when it was trained with 40% of the available views of 101 data points over the 6.5-17.5 GHz band and tested with aspect views over this frequency band. The performance of the net with narrow spectral band data can be improved by increasing the percentage of available aspect views used for training. Wh n the input frequency data to the first layer of the net consisted of 50 points over the

10.5-15.9 GHz band, and the percentage of the available aspect views used for training the net was increased to 50%, the performance of the net in identifying the Boeing 747 model was found to improve to 99%.

The divergence mentioned in the preceding observation (b) occurs when the number of input data points to the net, and hence the number of input layer neurons (and thus the number of hidden neurons, which equals the number of neurons in the input layer), is too small. Theoretical considerations of the mapping power of multi-layer networks [8],[15] suggest that any mapping can be accomplished through a network of the type shown in Fig. 15 provided that an adequate number of hidden neurons is used (see cautionary arguments noted in epilogue, [13]). We therefore tested whether the network can converge and learn to form internal representations of the targets when the number of input data points was small by increasing the number of hidden neurons in the net. As mentioned earlier, when the number of input (frequency response data) points over the 6.5-17.5 GHz band to the net is reduced to 17, the learning process by the net could not converge; in this case, the number of the hidden neurons was also 17. However, by increasing the number of hidden neurons to 21, the net is able to converge and learn the internal representations for the given aerospace target models. It should be pointed out that, since the Fourier transform mapping between the hidden and input layers in the net of Fig. 15 is carried out according to the discrete summation given in (34), the number of hidden neurons does not have to be equal to the number of input layer neurons (see also equation (7)); this result supports the theory in [8],[15]. By increasing the number of hidden neurons further, the number of learning cycles required by the net to converge during the training process is reduced. Once there are enough hidden neurons and the net is able to converge to learn the internal representations for the given aerospace target models, no clear improvement in performance is found, in terms of correctly identifying the given target models when the number of hidden neurons is increased further [21].

8 Classification, Identification and Cognition

The terms "target identification" and "target recognition" are frequently used interchangeably in the literature, and we have done the same here. Actually there is an important difference between the two terms. The network we have described in the preceding section is not cognitive. Once it has learned a set of targets, it can correctly identify which out of

the set is responsible for the sensory signal (e.g., the complex frequency response) presented at its input by producing a correct identification label at its output. The net is robust, in that noisy versions of its training set data are also correctly classified by triggering the correct identification label. This robustness also provides for a generalization capability, in that the network is able to classify correctly a data set belonging to the learned object that was not specifically among the training set. This capability to generalize means that the net does not have to be trained on all data sets needed to represent the object as dictated by angular sampling considerations (e.g., the scattering pattern of a target of extent L must be sampled approximately every $\bar{\lambda}/L$ [radians] when $\bar{\lambda}$ is the mean wavelength of observation). Without proper precautions, these robustness and generalization features also mean that every input presented to the network will produce a response by triggering a label, even when the input belongs to a novel object, i.e., one that was not learned by the network. The network is therefore not cognitive in that it has no mechanism for determining whether a presented signal belongs to a familiar (previously learned) object or to a novel object. Cognitive capability is essential for proper interpretation and use of a classifier network's response, as well as for possible triggering of other useful mechanisms like learning a novel input and adding it to the repertoire of the net.

There are several ways to impart cognition to a classification network. One is to train the network on every object it could possibly encounter in its environment in the course of normal operation. This approach may not, however, be practical, as it could require a major increase in the size of the network. especially when the number of possible targets is very large. A second way to impart cognition is to add at the system sensory level detectors that analyze the received signals to see whether they belong to the class of targets of interest. Usually, inference rules and decision trees are needed to make such distinctions, and more than one sensing modality is often indicated (e.g., measurement of altitude, speed, bearing, size (radar cross section). polarization, etc.). A third way for making a network cognitive is to incorporate cognitive capabilities in designing the net from the outset [22].

9   Discussion

Extrapolation and reconstruction by neural networks through learning were discussed in the first part of this paper. This approach provides a novel way for near-perfect extrapolation and reconstruction from partial frequency response information. The approach leads

by logical extension to the problem of target identification using label representations at the output layer in place of the exact object functions reconstructed in the extrapolation problem. The focus in using neural networks for extrapolation and recognition is on the structure of networks and on the learning that takes place in them, and not on any particular computation carried out by a particular neuron. The number of neurons in the hidden layer of such networks need not be equal to that in the input layer, as in most of the nets presented here, and can be increased at will. The synaptic connections from the input layer to both the hidden and the output layers need not be fixed, as was the case in this study, but can learn to handle any reconstruction problem in which the available data and the object functions do not necessarily have a Fourier transform relation or when the relation is not certain or known. In our work, the measured frequency response data and the object function (the real part of the Fourier inverse of the frequency response, i.e., the real part of the complex range profile of the target) form a Fourier transform pair. For practical application of the target identification concept presented in this paper, one envisions that a library of frequency responses of scale models of targets of interest can be generated by measurements under controlled conditions in an anechoic chamber radar scattering measurement facility for all target aspects relevant to practical encounter scenarios between a radar system and the target. Data generated in this fashion would be "taught" to a layered net by training as we have described. To use such "trained nets" to identify actual radar targets (that correspond to the scale models used) from data generated by broad-band radar systems in the field, attention to scaling issues would be given by invoking the principle of electromagnetic similitude [20]. In this fashion, one hopes to avoid the tedious and costly task of forming libraries in the field using actual radar systems and cooperative target "fly-bys".

The number of neurons in the input layer of our learning networks is determined by the number of available frequency samples. The relation between the number of functions that can be learned by the network and the number of neurons in the hidden layer is still an open question; however, the theoretically established claim for the mapping power of multi-layer neuron networks [8], [15] taken together with the findings of this work, provide strong evidence in support of the use of layered networks for target recognition. Nonlinear mappings in layered networks enable the formation of the desired reconstruction mapping region [15] to give robust reconstructions from partial and noisy frequency information. The application of these concepts to the problem of noncooperative radar target identification provides convincing evidence of the capability of neuromorphic processing in providing

results not attainable by traditional signal processing techniques.

References

[1] A.N. Tikhonov and V.Y. Arsenin, *Solutions of ill-posed problems*, New York: Wiley, 1977.

[2] J. Hadamard, *Lectures on the Cauchy problem in linear partial differential equations*, Yale University Press, New Haven, 1923.

[3] N.H. Farhat and B. Bai, "Echo inversion and target shape estimation by neuromorphic processing," *Neural Networks*, vol. 2, pp. 117-125. 1989.

[4] T.P. Burg, "Maximum entropy spectral analysis," presented at the 37th meeting of the society of Exploration Geophysicists, October 1967.

[5] A. Papoulis, "A new algorithm in spectral analysis and band-limited extrapolation," *IEEE Trans. on Circuits and Systems*, vol. CAS-22, pp. 735-742, Sept. 1975.

[6] R.W. Gerchberg, "Super-resolution through error energy reduction," *Optica Acta*, vol. 21, pp. 709-720, 1974.

[7] J.J. Hopfield, "Neural networks and physical systems with emergent collective computational abilities," *Proc. of Natl. Acad. Sci. USA*, vol. 79, pp. 2554-2558, April 1982.

[8] D. Rummelhart, G. Hinton, R. Williams, "Learning internal representations by error propagation," *Parallel Distributed Processing*, vol. 1, MIT press, Cambridge, 1988.

[9] P. Werbos, and J. Titus, "Beyond regression: new tolls for prediction and analysis in the behavioral sciences," Harvard University dissertation, 1974.

[10] D.B. Parker, "Learning logic," *MIT Technical Report*, TR-47, Center for Computational Research in Economics and Management Science.

[11] Y. Le Cun, "A learning procedure for an asymmetric threshold network," *Proceedings of Cognitiva*, vol. 85, pp. 599-604, 1985.

[12] N.H. Farhat, *et al.*, "Projection theorems and their application in multi-dimensional signal processing," in *Advances in Optical Information Processing*, G.M. Morris (Ed.), SPIE, vol. 388, pp. 140-151, 1980.

[13] M. Minsky and S. Papert, *Perceptrons,* MIT press, Cambridge, 1969.

[14] B. Widrow, *et al.*, "Layered neural nets for pattern recognition," *IEEE Trans. on ASSP.* vol. 36, pp. 1109-1118, July 1988.

[15] R.P. Lippmann, "An introduction to computing with neural nets," *IEEE ASSP Magazine*, pp. 4-22, April 1987.

[16] N.H. Farhat, "Microwave diversity imaging and automated target identification based on models of neural networks," *Proc. IEEE* vol. 77, pp. 670-681, May 1989. See also: N.H. Farhat, S. Miyahara, and K.S. Lee, "Optical analogs of two-dimensional neural networks and their application in recognition of radar targets," in *Neural networks for computing*, J.S. Denker, Ed. American Institute of Physics, AIP Conf. Proc. 151, New York, 1988.

[17] C.W. Chuang and D.L. Moffatt, "Natural resonances of radar targets via Prony's method and target discrimination," *IEEE Trans. Aero. and Electro. Systems*, vol. AES-12, pp. 583-589, Sept. 1976.

[18] M.L. Van Blaricum and R. Mittra, "Problems and solutions associated with Prony's method for processing transient data," *IEEE Trans. Anten. Propa.* vol. AP-26, pp. 174-182, Jan. 1974.

[19] D. Hubel and T. Wiesel, "Receptive fields, binocular interaction and functional architecture in the cat's visual cortex," *J. Physiol.* vol. 160, pp. 106-154, 1962.

[20] J.D. Stratton, *Electromagnetic Theory*, McGraw Hill, New York, 1941, pp. 488-490.

[21] R. P. Gorman and T.J. Sejnowski, "Learned classification of sonar targets using a massively parallel network," *IEEE Trans. ASSP.* vol. 30, pp. 1135-1140, July 1988.

31

[22] S. Shinomoto, "A cognitive and associative memory," *Biol. Cybern.* vol. 57, pp. 197-206, 1987.
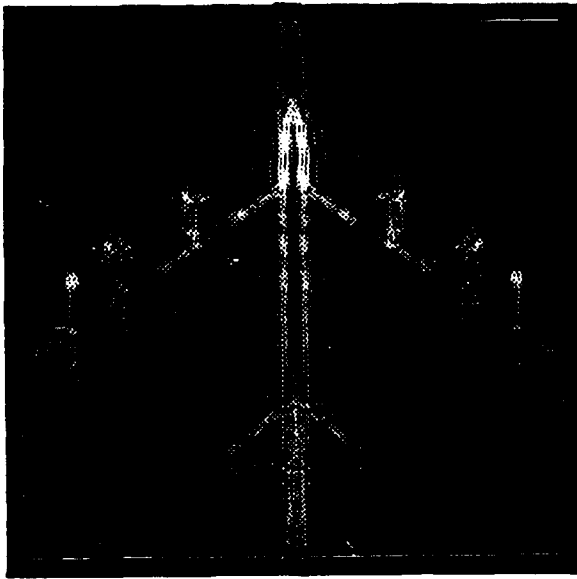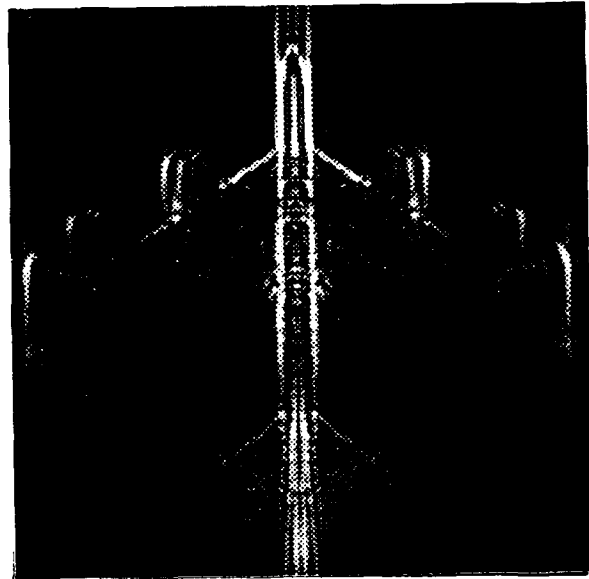
(a)　　　　　　　　　　　　　　(b)
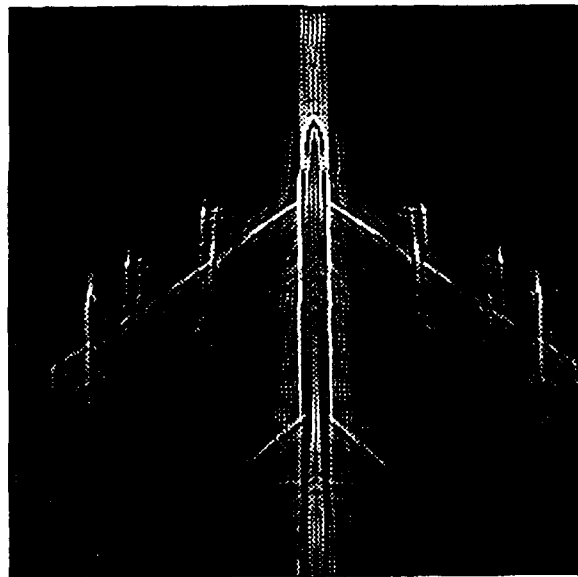
(c)

Figure 1: Microwave images reconstructed by DFT (a) for spectral bandwidth 6-17 GHz and (b) for spectral bandwidth 2-26.5 GHz; (c) image reconstructed by nonlinear neural net for the 6-17 GHz spectral bandwidth data.

33
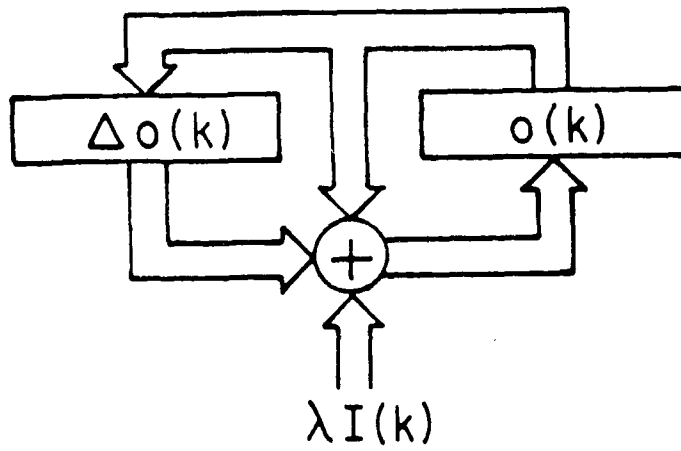
(a)
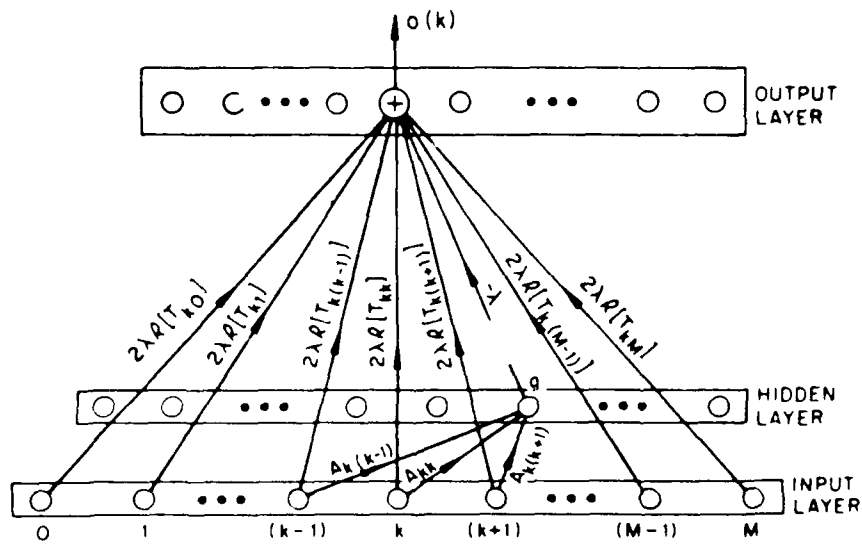
(b)

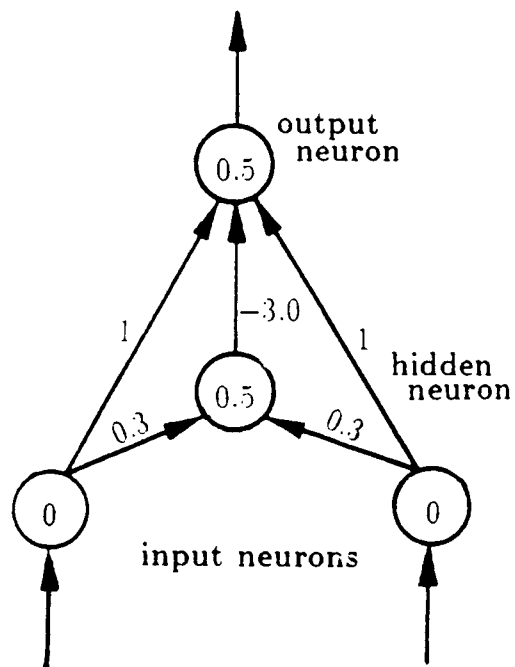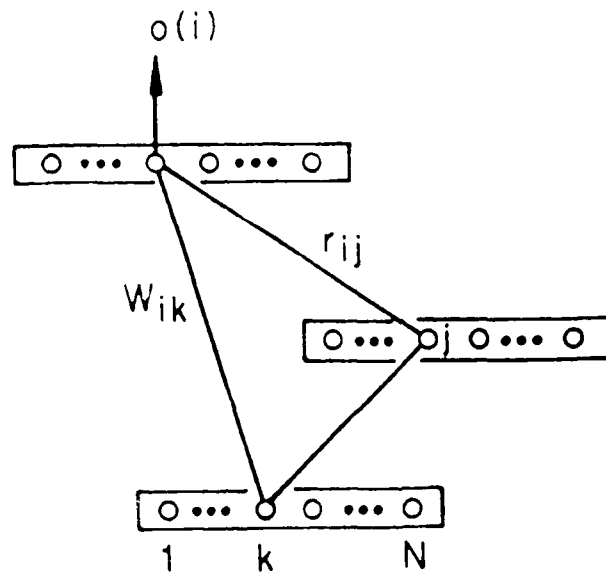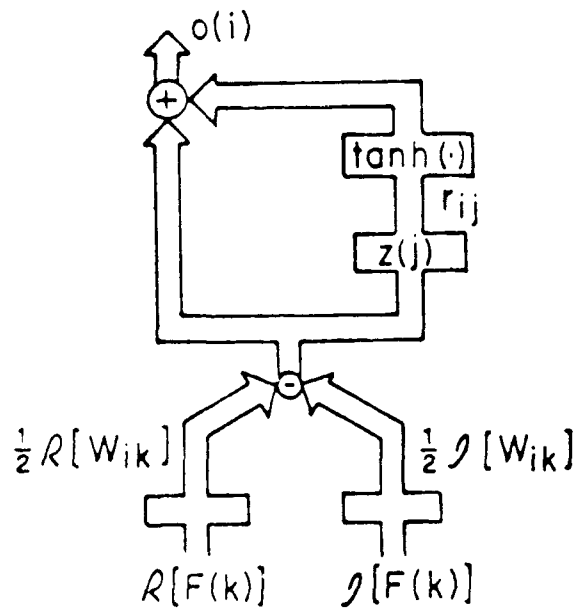Figure 2: (a) Realization of the neural net processor; (b) realization of nonlinear regularization in the neural net processor.

Figure 3: Network for XOR mapping.

Figure 4: A three-layered neural net for reconstructions through learning: (a) neuron distribution and connectivities; (b) equivalent flow chart.
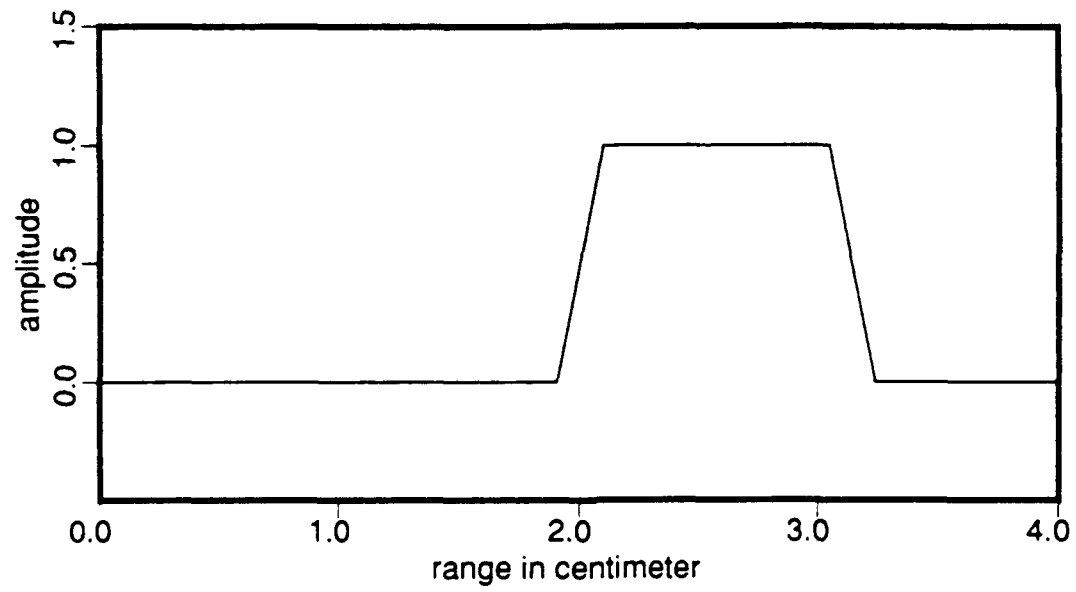
Figure 5: Two test object patterns $o(r)$ used in simulations: (a) first pattern; (b) second pattern.
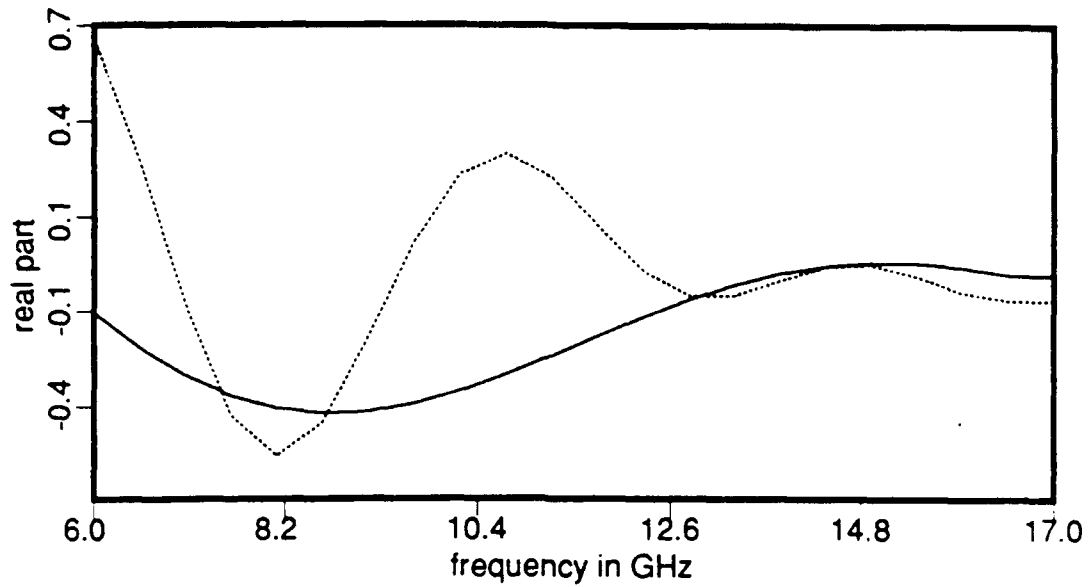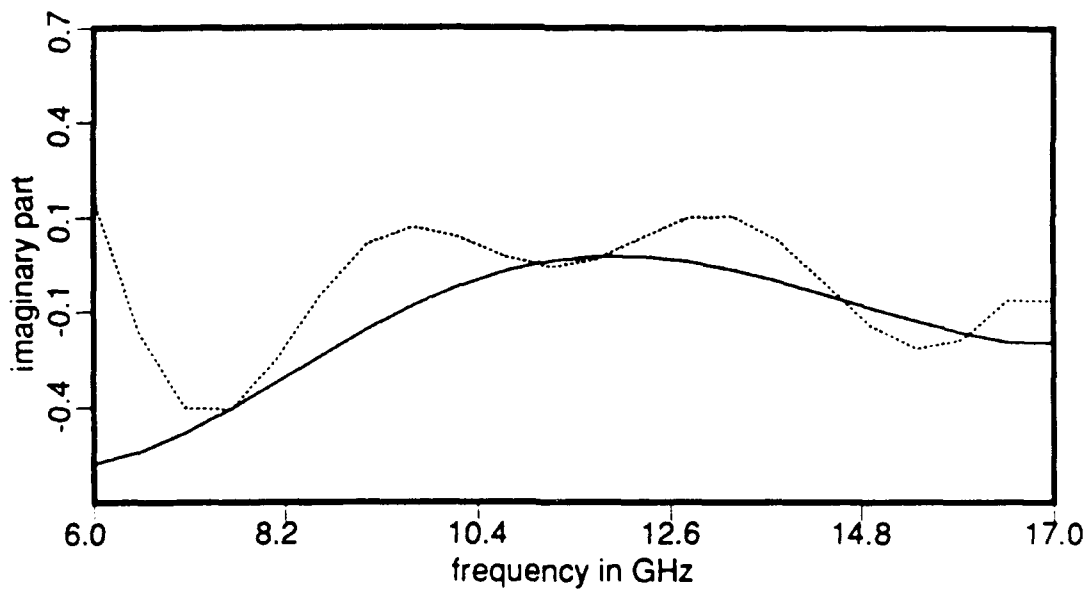
Figure 6: Frequency responses for the first object (solid line) and the second object (dotted lined): (a) real part; (b) imaginary part.
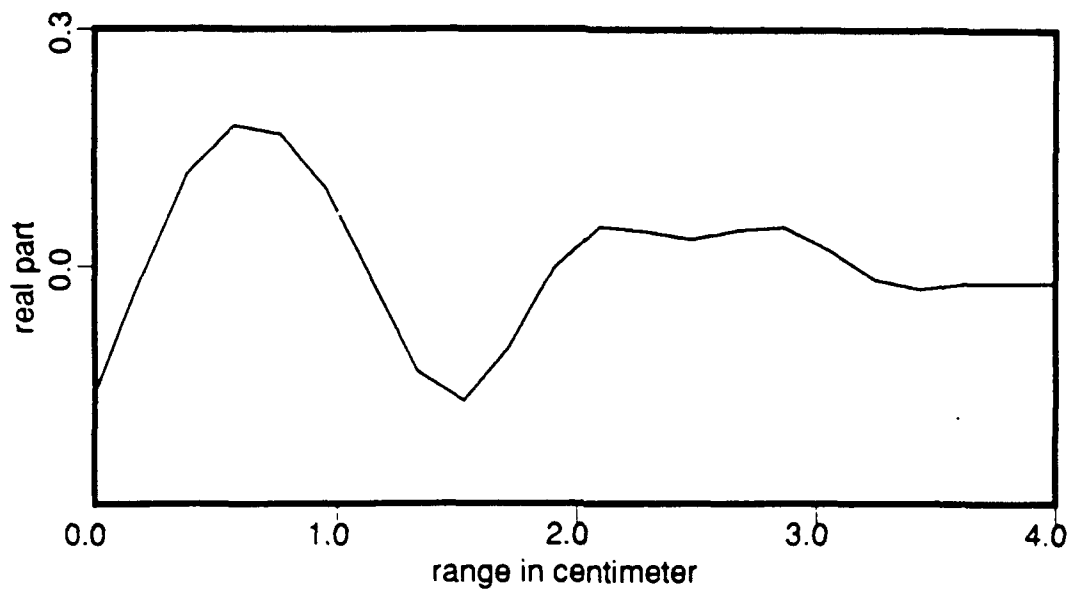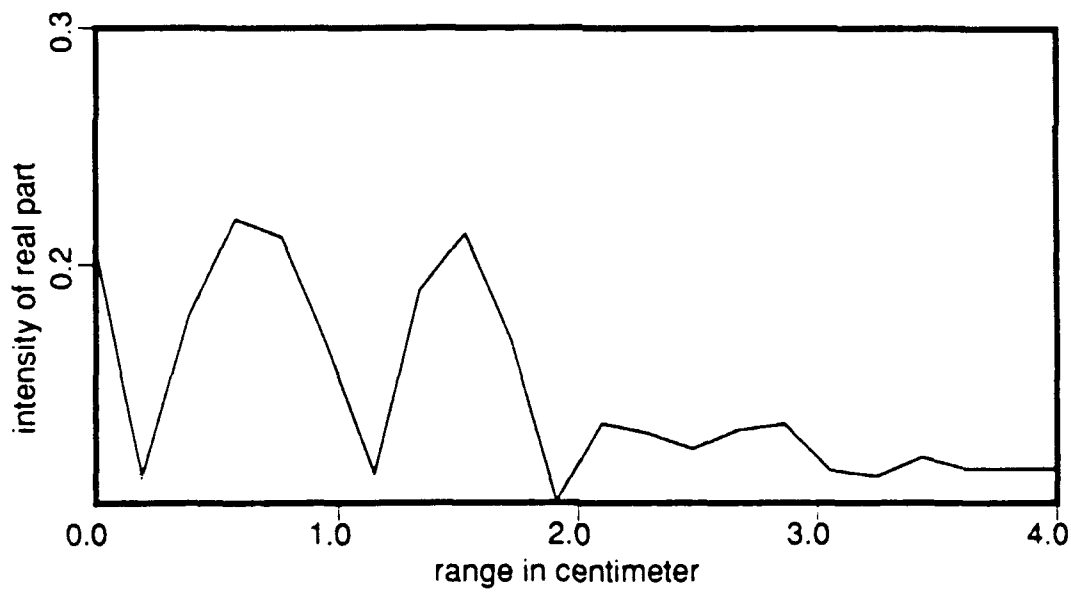
Figure 7: Reconstruction of the first object pattern by DFT: (a) real part; (b) intensity.

(a) 1st pattern is used for training the net in the 1st learning cycle.

(b) 2nd pattern is used for training the net in the 1st learning cycle.

(c) 1st pattern is used for training the net in the 2nd learning cycle.

(d) 2nd pattern is used for training the net in the 2nd learning cycle.

(e) 1st pattern is used for training the net in the 3rd learning cycle.

(f) 2nd pattern is used for training the net in the 3rd learning cycle.

(g) 1st pattern is used for training the net in the 4th learning cycle.

(h) 1st pattern is used for training the net in the 5th learning cycle.

Figure 8: Sequence shows how the network gradually learns the synaptic connections to provide eventually the correct output for two patterns from partial associated frequency responses presented at its input.

40
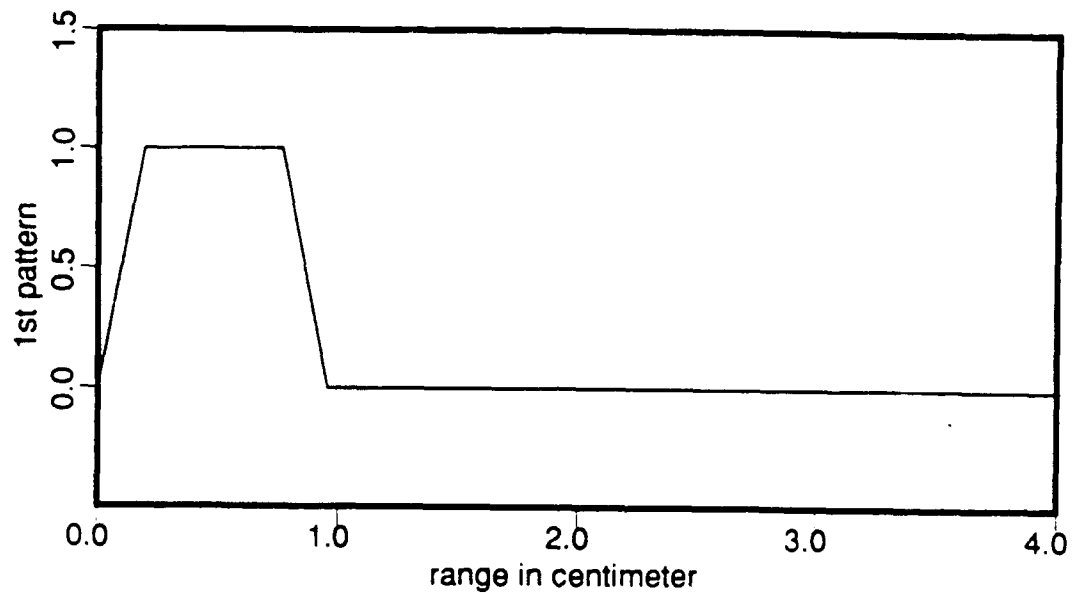
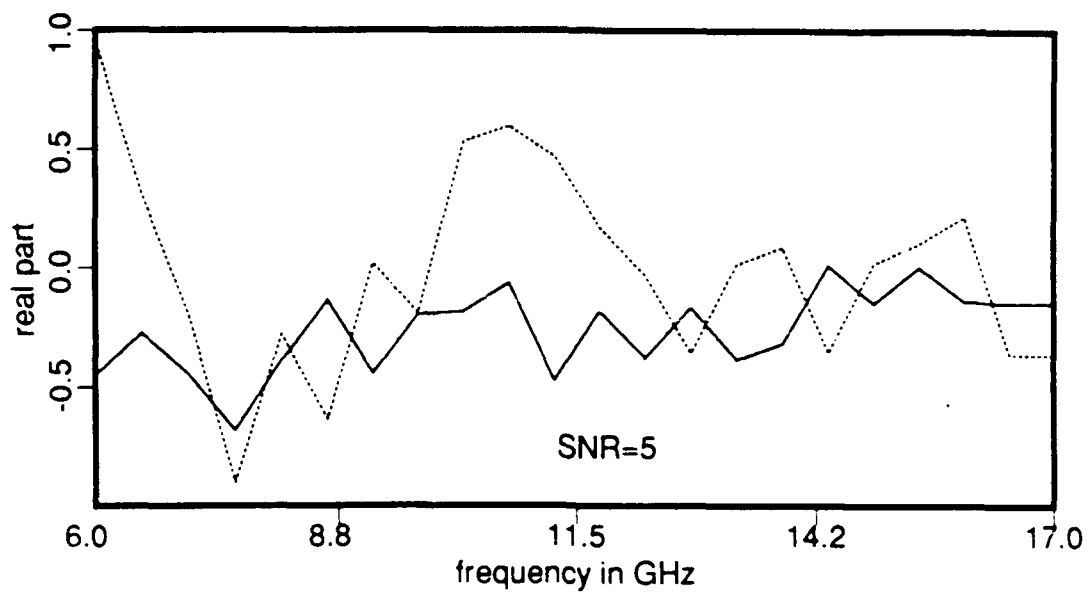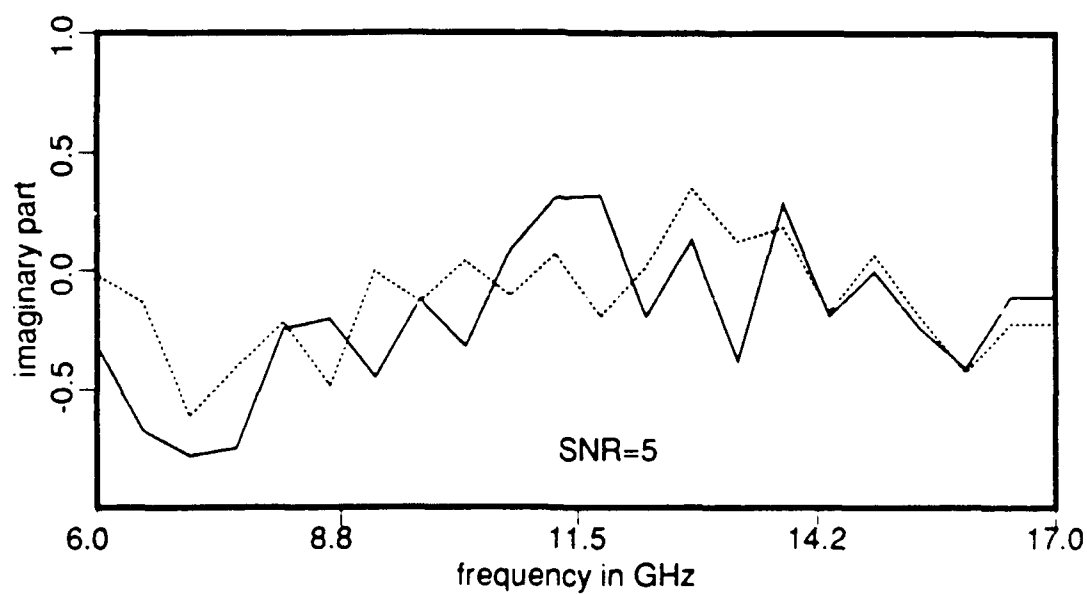Figure 9: Object patterns with more complex shapes used in simulation: (a) first pattern: (b) second pattern.
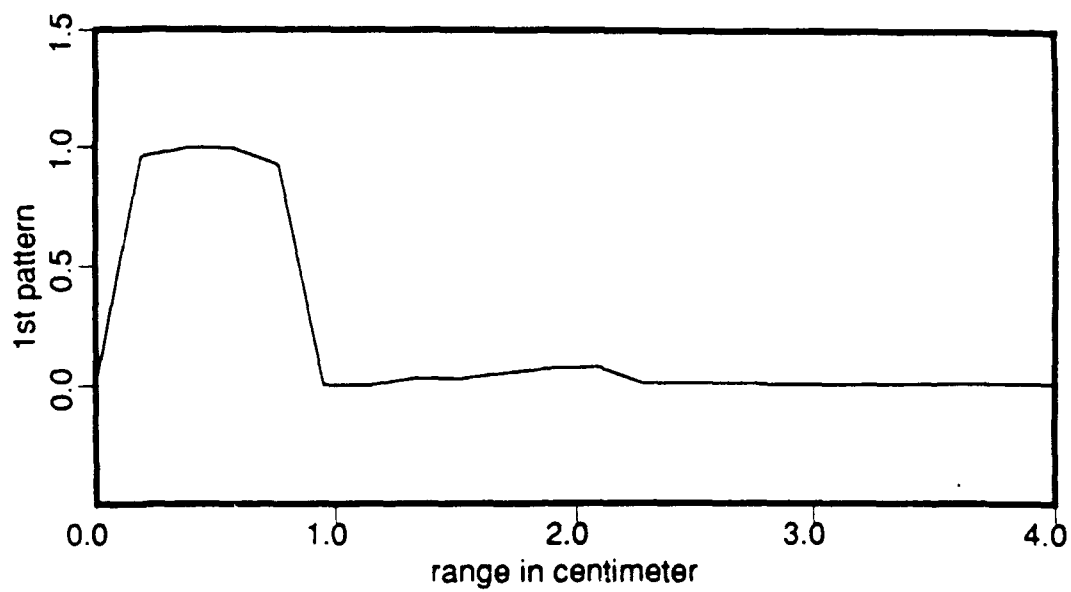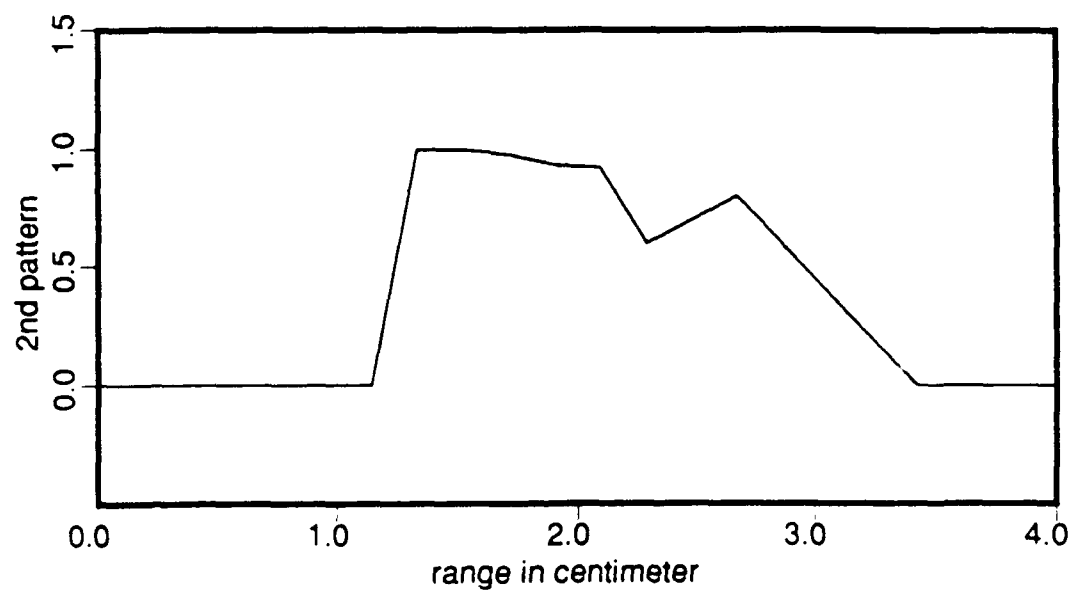
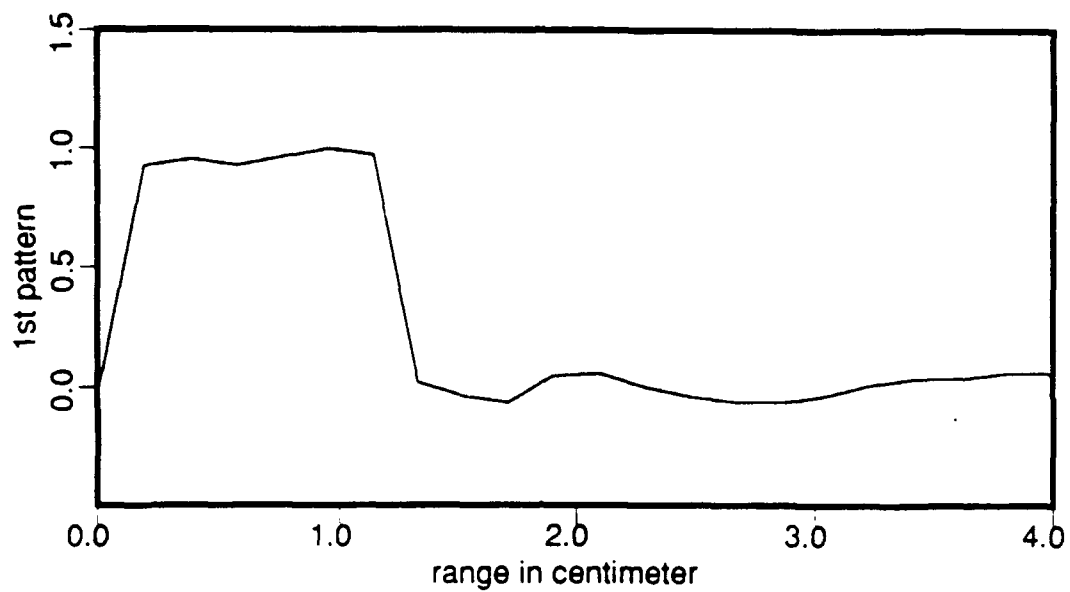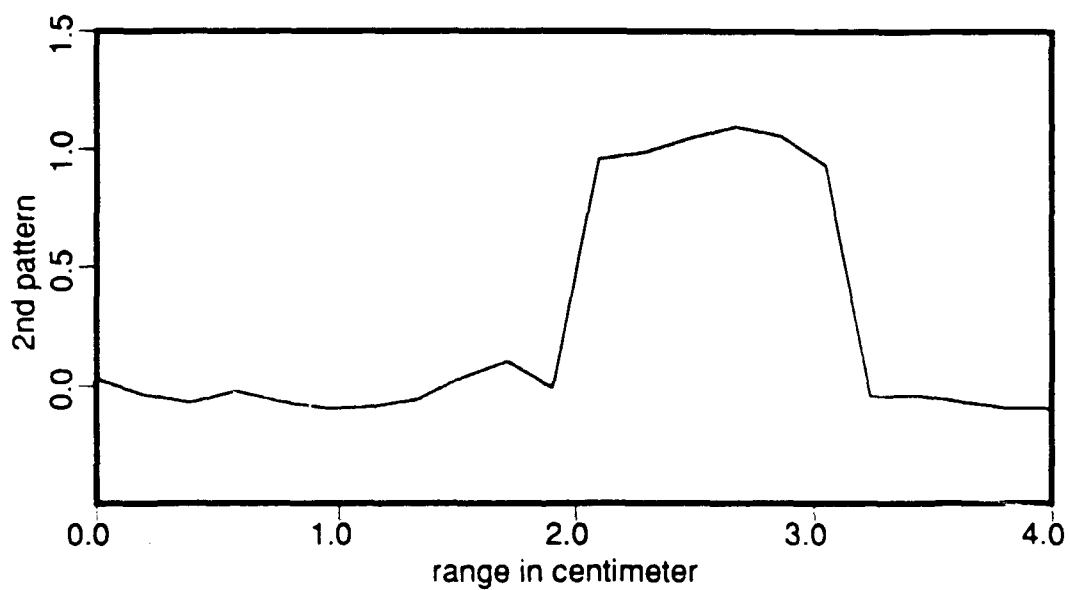Figure 10: Reconstructions of the complex-shaped patterns of Fig. 9: (a) first pattern: (b) second pattern.

42

Figure 11: Noise-contaminated frequency responses (SNR = 5) of the first pattern (solid line) and the second pattern (dotted line) of Fig. 5: (a) real part; (b) imaginary part.

Figure 12: Reconstructions from noise-contaminated frequency responses of Fig. 11: (a) first pattern; (b) second pattern.
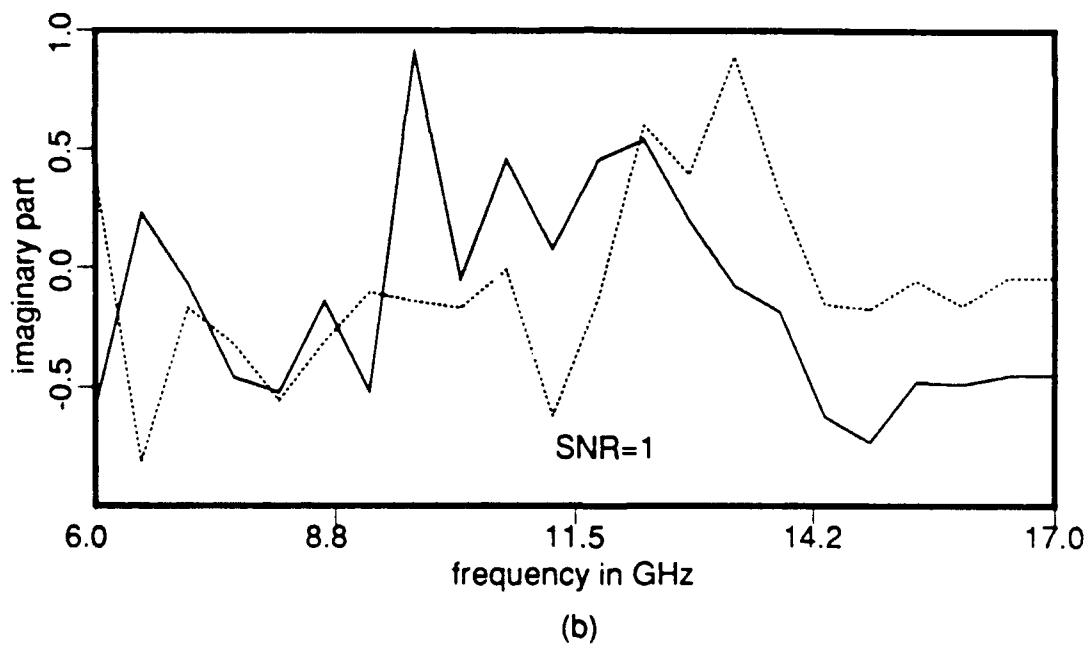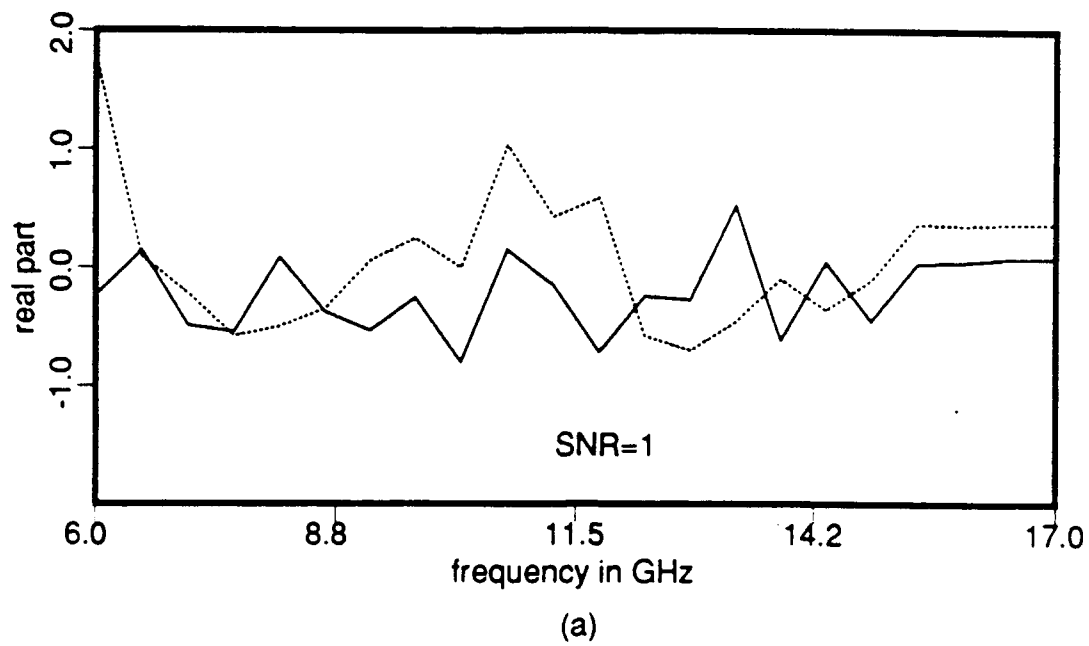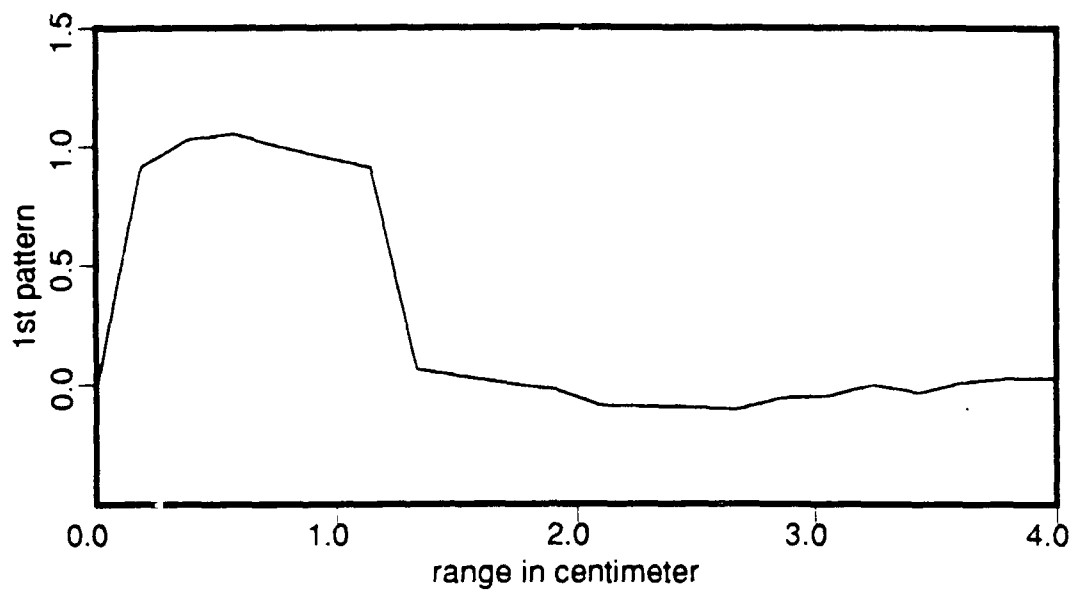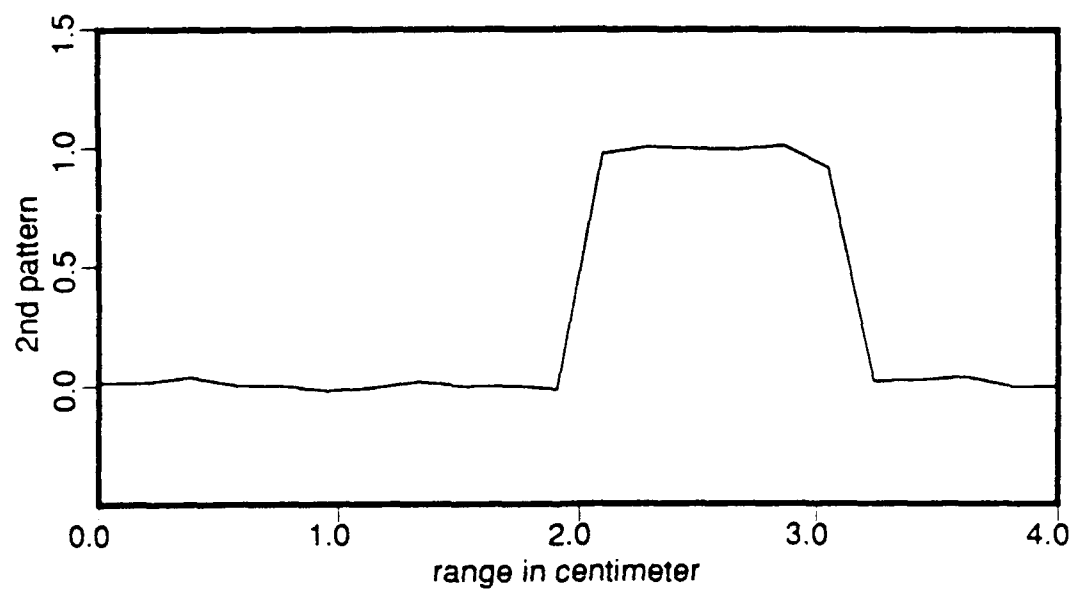
Figure 13: Noise-contaminated frequency responses (SNR=1) of the first pattern (solid line) and the second pattern (dotted line) of Fig. 5: (a) real part; (b) imaginary part.

(a)

(b)

Figure 14: Reconstruction from the noisy data (SNR=5) of Fig. 11 after the network has been trained with instances of the noisy data (SNR=1) of Fig. 13 and the noise free data of Fig. 6: (a) first pattern; (b) second pattern.
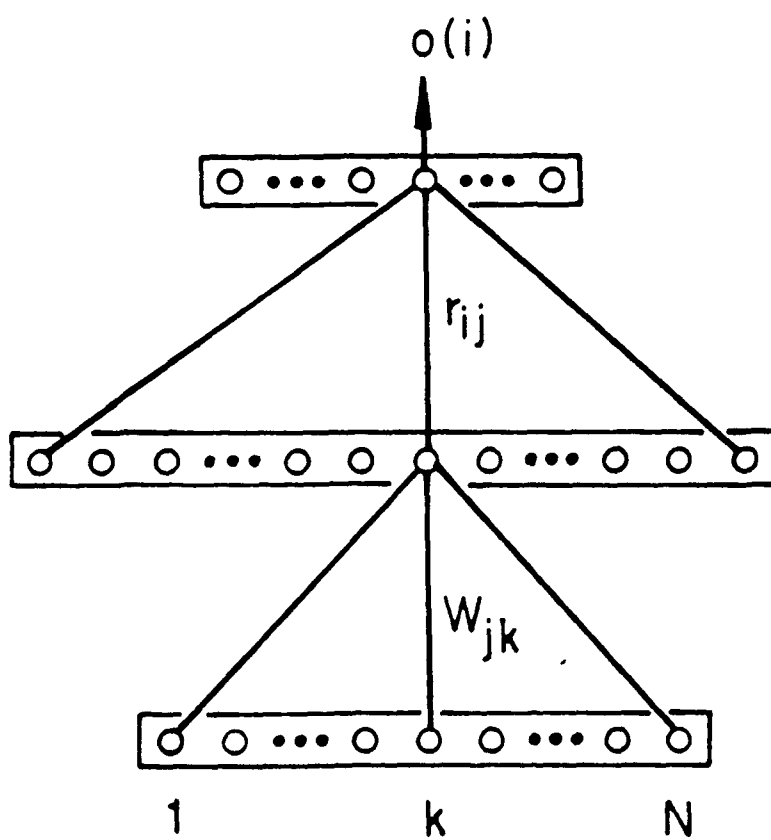
Figure 15: Neural network for target recognitions.
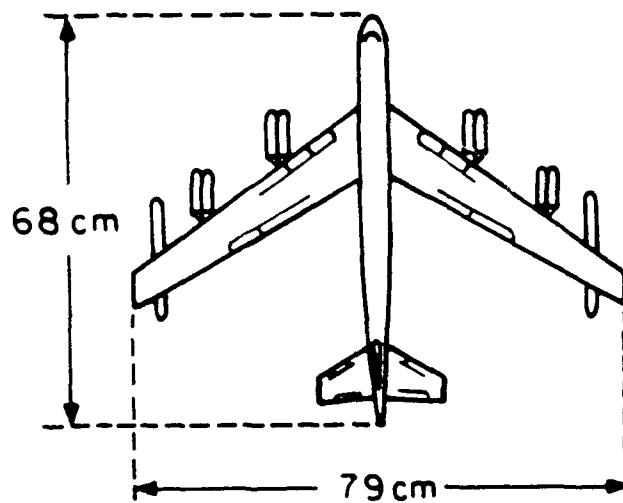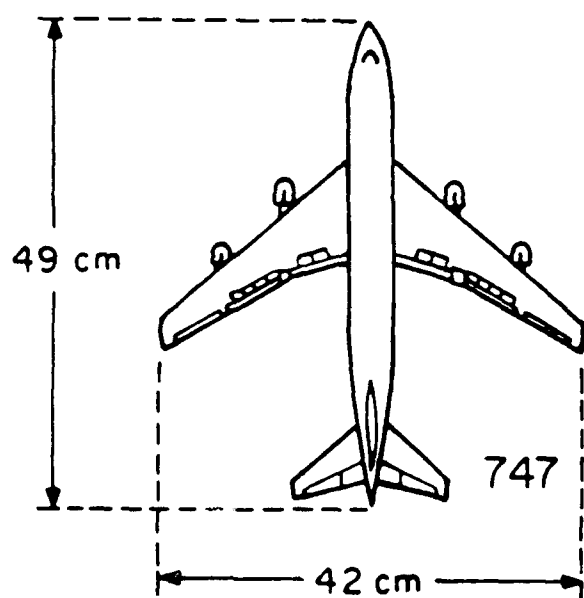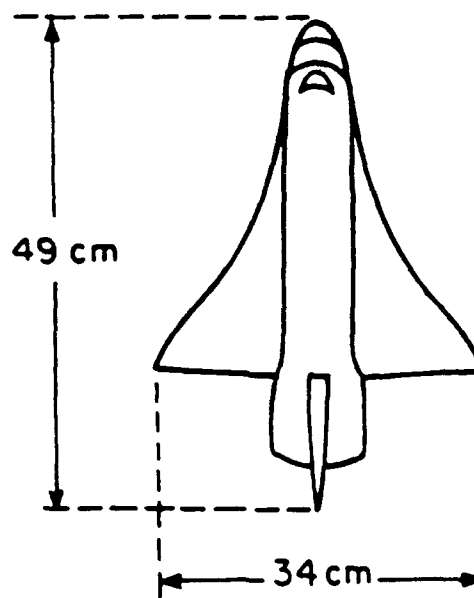
Figure 16: Three aerospace targets used: (a) a B-52 airplane; (b) a Boeing 747 airplane; (c) a space shuttle.
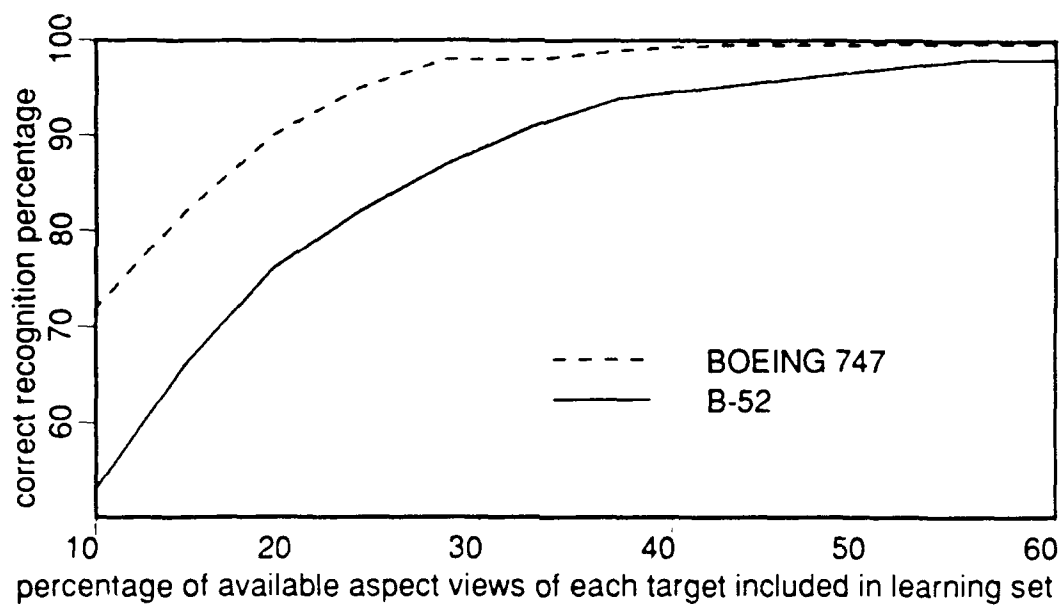
Figure 17: Correct recognition from single echo or "look" *vs.* size of training set for the B-52 (solid line) and for the Boeing 747 (dashed line).

49
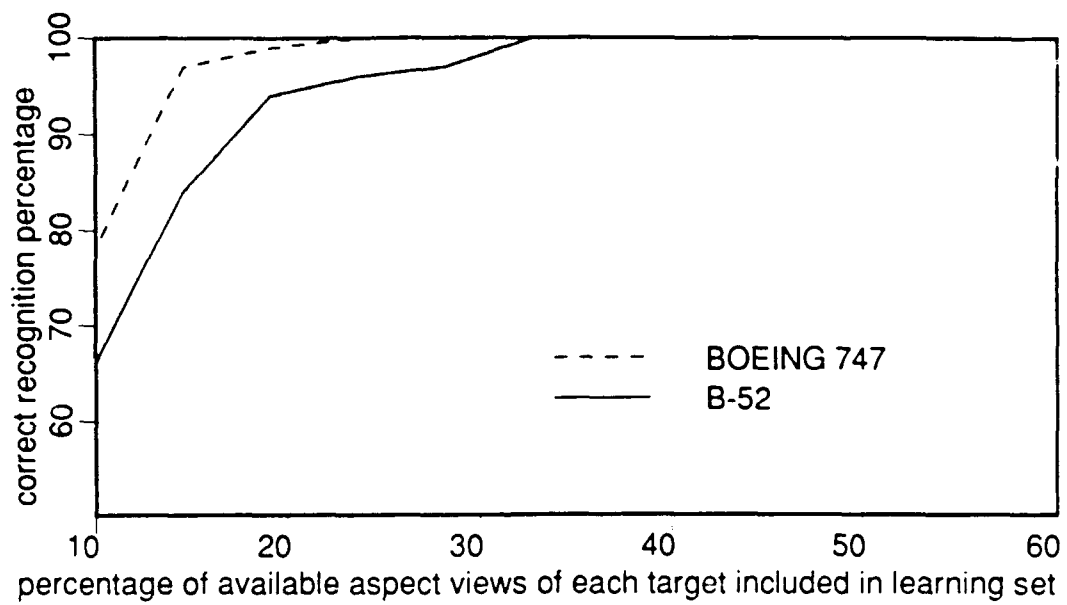
Figure 18: Correct recognitions *vs.* the size of training set when "a two out of three" majority vote criterion is used for correct classification, for the B-52 (solid line) and for the Boeing 747 (dashed line).
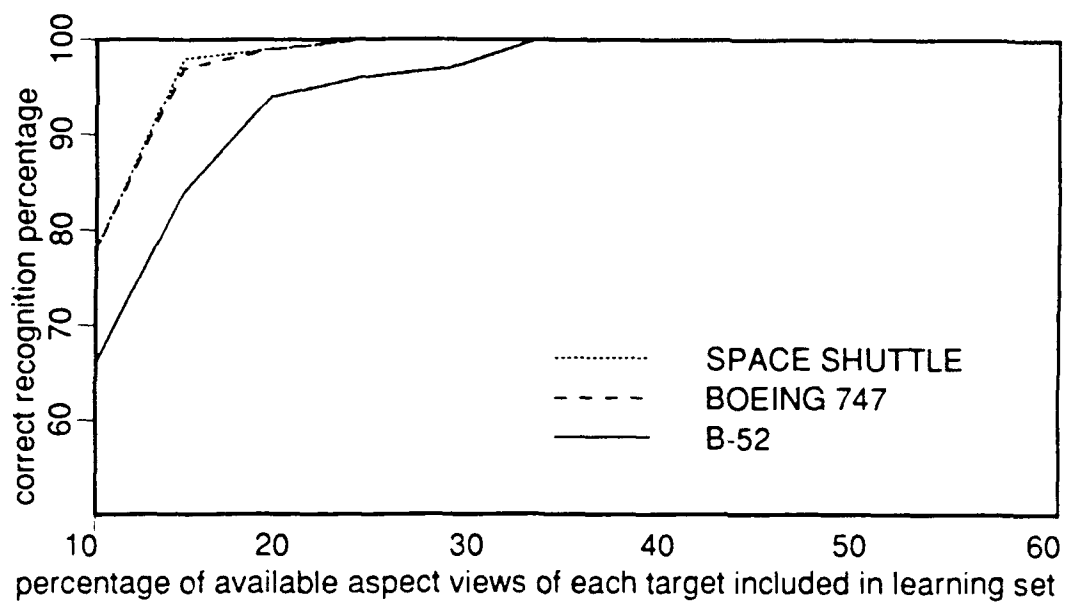
Figure 19: Correct recognitions *vs.* the size of training set when "a two out of three" majority vote criterion is used for correct classification for the B-52 (solid line), Boeing 747 (dashed line), and Space shuttle (dotted line).

AP-S
INTERNATIONAL SYMPOSIUM
1989

1989 INTERNATIONAL SYMPOSIUM DIGEST
ANTENNAS AND PROPAGATION
VOLUME II

INSTITUTE OF ELECTRICAL
AND ELECTRONICS ENGINEERS

SAN JOSE, CA
JUNE 26-30, 1989

PHASE SPACE ENGINEERING FOR NEURODYNAMIC TARGET IDENTIFICATION

N.H.Farhat* and H.Babri
University of Pennsylvania
The Moore School of Electrical Engineering
Electro-Optics and Microwave-Optics Laboratory
Philadelphia, PA 19104

Summary

Past research at the Electo-Optics and Microwave-Optics Laboratory [1]-[4] has led to inception and development of microwave diversity imaging where angular, spectral, and polarization degrees of freedom are combined to form images of complex shaped objects with near optical resolution. An example of attainable image quality is shown in Figure 1. This is a projection image of the scattering centers on a test object (a 100:1 scale model of a B-52). Co-polarized and cross-polarized data sets, each consisting of 128 azimuthal looks at the target extending from head on to broad-side (90 degree angular aperture) and an elevation angle of 30 degrees with each look covering a (6-17) GHz spectral window were utilized in obtaining the image shown. Also a novel target derived reference technique [5] for correcting the frequency response data for undesirable range-phase (or range-phase time rate (Doppler) when the target is moving) together with an image symmetrization [4] method were painstakingly developed and perfected before the image quality shown in Figure 1 could be obtained. In later discussion we will be referring to range-profiles of a target. The range profile at a given target aspect is taken to be the real part of the Fourier transform of the corrected frequency response measured for that aspect. For a fixed spectral window and signal to noise ratio, the range profile is independent of range and varies only with aspect.

Application of concepts and methodologies developed and demonstrated in the above research in practice would entail: either (a) the use of large, albeit sparse, recording imaging apertures to furnish the angular diversity needed or (b) the use of a single radar system that can track and interrogate a target, in the presence of relative motion, from different aspect angles in time to furnish the required angular diversity in an inverse synthetic aperture radar (ISAR) or spot light imaging mode. The first approach is prohibitively costly specially when the target is remote and the angular aperture needed to achieve useful resolution is large. The second approach is non-real-time in nature as it requires observing the target over extended time intervals, and this may not be acceptable in numerous applications, in order to synthesize the required angular aperture. One is therefore constrained in practice to limited angular apertures or limited observation times and is therefore faced with the longstanding problem of image formation from limited and often sketchy (partial and noisy) information, i.e., one is faced with the classical problem of super-

resolution which has evaded a general solution for a long time. In other words, the problem is to recognize the target from a few looks

Among its many fascinating capabilities such as robustness and fault tolerance, the brain is also able to recognize objects from partial information. We can recognize a partially obscured or shadowed face of an acquaintance or a mutilated photograph of someone we know with ease. The brain has a knack for supplementing missing information, based on previously formed and stored associations.

Here we propose and describe a new concept in automated radar target identification from a single "look" (coherent broad-band echo) based on neural net models. We view a neural net as a multidimensional nonlinear dynamical system capable of exhibiting powerful collective computational and signal processing functions that are fully and therefore best described by their phase-space behavior in terms of terminal, or periodic, or strange attractors and associated basins of attraction. The work
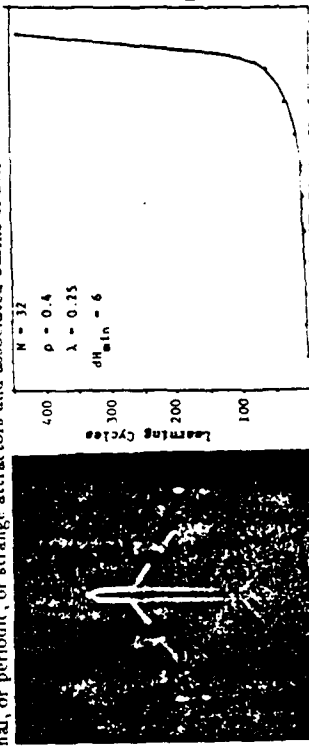
Fig.1: Microwave diversity image of a complex shaped object

$N = 32$
$\rho = 0.4$
$\lambda = 0.25$
$dH_{min} = 6$

Number of vectors stored in sequence, M

Fig. 2: Learning cycles needed for correct recall of a sequence of correlated vectors, N in the sequence, versus number of vectors, M in the sequence.

described is a direct extension of earlier work on neuromorphic target identification [6],[7]. We maintain that a central issue in understanding and applying neural nets today is finding ways for imparting to a net distinct phase-space behaviour that gives rise to desired functions. This phase-space engineering approach represents a totally new paradigm in signal processing that originates from known universal features of biological information processing in the nervous system. We will present initial results illustrating one possible method for applying the phase space engineering concept to the longstanding problem of recognizing airborne targets from a single look. In this approach phase space trajectories are formed from data contained in a library of range-profiles of the target within a prescribed "solid-angle of encounter" defined by all target aspects that can possibly be encountered by the radar system in typical practical situations. Initiating such a net from a state corresponding to any one of these profiles would trigger motion in its phase-space along the stored trajectory towards a terminal "label" state or terminal attractor that identifies the target uniquely.

To demonstrate this we choose a fully connected neural net of N bipolar binary neurons with state vector $s_i[1,-1], i=1,2,\ldots,N$, (representing binarized representations of range-profiles), and connectivity matrix W with elements w_{ij}. The net updates its state vector synchronously according to $s_i = sgn(u_i)$, where $sgn()$ is the signum function and $u_i = \sum_j w_{ij} s_j$ is the action potential of the i-th neuron. Starting from an initial connectivity matrix $w_{ij}^{(0)} = 0$ the required connectivity matrix is formed by

$$w_{ij}^{(k)} = w_{ij}^{(k-1)} + \lambda(s_i^{(m)} s_j^{(m+1)} - s_i^{(m)} o_j^{(m)}) \qquad (1)$$

where $w_{ij}^{(k)}$ is the connectivity matrix at the end of the k th learning cycle, $s_i^{(m)}$ is the m th state vector in a sequence of M vectors, $o_i^{(m)}$ is the state vector arrived at after one iteration from an initial state $s_i^{(m)}$, λ is a positive real parameter controlling the learning process. In the above notation $s_i^{(M+1)}$ is taken to be a label vector identifying the sequence. A learning cycle consists of repeated application of the above formula until the change $\Delta w_{ij} = w_{ij}^{(k)} - w_{ij}^{(k-1)}$ becomes sufficiently small such that subsequent testing of the formed net by initiating it from any member vector of the stored sequence results in its sequencing through all following members and terminating at the label vector. The number of learning cycles needed to learn M vectors using the above procedure is shown in Figure 2 for a neural net of $N = 32$ neurons (similar behavior was observed for $N = 64$ and 128). The stored sequence consisted of vectors with parameter ρ fixed at 0.4 (roughly similar behavior was observed for $0.1 < \rho < 0.9$). The Hamming distance between any pair of vectors in the sequence ranged from 6 to 9 ($6 < dH < 9$), thus the vectors in the sequence were well correlated. The value of the learning rate parameter λ was 0.25. It is seen that the training procedure or learning algorithm converges rapidly as long as $M \leq N$. As M increases beyond N the learning time, measured in number of learning cycles is seen to increase exponentially. It is worth noting however that a sequence with $M \gtrsim N$ can still be stored provided that a longer learning period can be tolerated. The sequential storage and recall capabilities exhibited here exceed by far the storage capabilities of Hopfield like nets [8] where entities are stored as limit points in phase space rather than in trajectories or orbits as is the case here. To evaluate the performance of the net, with u_i, obtained by the above training procedure, it was initiated from randomly selected phase-space points and its subsequent motion in phase space from iteration to iteration observed. We find such random probing to be a useful tool in phase space engineering work whereby qualitative information is obtained about the strength and nature of the basins of attraction of a terminal attractor and on whether it possesses spurious basins of attraction or not. Ninety such probing vectors whose Hamming distance from any of the vectors stored in the phase space trajectory exceeded a given minimum distance dH_{min} were used. For $dH_{min} = 1$ or 2 not a single probing vector triggered the net in its trajectory. The scheme presented appears therefore to discriminate well against initial states that do not belong to the stored object information. Simulations were also carried out to verify that several distinct terminal attractors with unique basins of attraction

can be formed in the same network. We have been able to store 3 such attractors with filamentary basins of attraction formed from anywhere from a total of 20 to 40 vectors with ease. The ideas presented here demonstrate the viability of the neuro-dynamical principles of object recognition from a single look. They have important implication for distortion invariant radar target recognition and have potential for obviating the need for costly radar imaging systems of the type required for remote target identification from formed images. An extensive research effort aimed at reducing the concepts presented here to practice is currently underway in our laboratory. Aspects of this program will be briefly discussed.

References

[1] N.H. Farhat, "Principles of Broad-Band Coherent Imaging," *J. Opt. Soc. Am.*, vol.67, pp.1015-1020, Aug. 1977.

[2] N.H. Farhat and C.K. Chan, "Three-Dimensional Imaging by Wave-Vector Diversity," *Proc. 1978 Int. Symp. on Acoustical Imaging*, A.Metherell (ed.), Plenum Press, New York, (1980), pp.499-515.

[3] C.K. Chan and N.H. Farhat, "Frequency Swept Imaging of Three-Dimensional Perfectly Conducting Objects," *IEEE Trans. on Ant. and Prop.*, Special Issue on Inverse Scattering, vol.AP-29, March 1981, pp.312-319

[4] N.H. Farhat, et al.,"Prospects for three-dimensional projective and tomographic imaging radar network," *Radio Science*, vol.19, no.5, pp.1347-1355, 1985.

[5] N.H. Farhat, et al., "A Target Derived Reference for Frequency Diversity Imaging," Poster paper presented at the *North American Radio Science / IEEE Meeting*, Quebec, Canada, 1980.

[6] Super Resolution, Patent disclosure filed by University Patents Inc., Westport, Ct. on behalf of the University of Pennsylvania, April 1987.

[7] N.H. Farhat, "Microwave Diversity Imaging and Automated Target Identification," to appear in *Proc. IEEE*, Special Issue on Radar Cross Section of Complex Shaped Objects, R.Stone (Ed.). (1988).

[8] J.J. Hopfield, "Neural Networks and Physical Systems with Emergent Collective Computational Abilities," *Proc. Natl. Acad. Sci., USA.*, vol.79, pp.2554-2560, (1982).

Optoelectronic Neural Networks and Learning Machines

Nabil H. Farhat

Foreword

Circuits and Devices Magazine is featuring three sequential articles on the current status of artificial neural network implementation technology. The current offering, on optronic implementation of artificial neural networks, is the second entry in this trilogy. It is sandwiched between the previous overview on analog implementation and the upcoming survey of digital artificial neural networks.

Nabil H. Farhat, who penned this overview, is a co-author of the 1985 article in Optics Letters and follow-up paper in Applied Optics that broke ground for modern optical implementation of artificial neural networks.

Robert J. Marks II

Abstract

Optics offers advantages in realizing the parallelism, massive interconnectivity, and plasticity required in the design and construction of large-scale optoelectronic (photonic) neurocomputers that solve optimization problems at potentially very high speeds by learning to perform mappings and associations. To elucidate these advantages, a brief neural net primer based on phase-space and energy landscape considerations is first presented. This provides the basis for subsequent discussion of optoelectronic architectures and implementations with self-organization and learning ability that are configured around an optical crossbar interconnect. Stochastic learning in the context of a Boltzmann machine is then described to illustrate the flexibility of optoelectronics in performing tasks that may be difficult for electronics alone. Stochastic nets are studied to gain insight into the possible role of noise in biological neural nets. We close by describing two approaches to realizing large-scale optoelectronic neurocomputers: integrated optoelectronic neural chips with interchip optical interconnects that enables their clustering into large neural networks, and nets with two-dimensional rather than one-dimensional arrangement of neurons and four-dimensional connectivity matrices for increased packing density and compatibility with two-dimensional data. We foresee integrated optoelectronics or photonics playing an increasing role in the construction of a new generation of versatile programmable analog computers that perform computations collectively for use in neuromorphic (brain-like) processing and fast simulation and study of complex nonlinear dynamical systems.

Introduction

Neural net models and their analogs offer a brain-like approach to information processing and representation that is distributed, nonlinear and iterative. Therefore they are best described in terms of phase-space behavior where one can draw upon a rich background of theoretical results developed in the field of nonlinear dynamical systems. The ultimate purpose of biological neural nets (BNNs) is to sustain and enhance survivability of the organism they reside in, doing so in an imprecise and usually very complex environment where sensory impressions are at best sketchy and difficult to make sense of had they been treated and analyzed by conventional means. Embedding artificial neural nets (ANNs) in man-made systems endows them therefore with enhanced survivability through fault-tolerance, robustness and speed. Furthermore, survivability implies adaptability through self-organization, knowledge accumulation and learning. It also implies lethality.

All of these are concepts found at play in a wide range of disciplines such as economics, social science, and even military science which can perhaps explain the widespread interest in neural nets exhibited today from both intellectual and technological viewpoints. It is widely believed that artificial neurocomputing and knowledge processing systems could eventually have significant impact on information processing, pattern recognition, and control. However, to realize the potential advantages of neuromorphic processing, one must contend with the issue of how to carry out collective neural computation algorithms at speeds far beyond those possible with digital computing. Obviously parallelism and concurrency are essential ingredients and one must contend with basic implementation issues of how to achieve such massive connectivity and parallelism and how to achieve artificial plasticity, i.e., adaptive modification of the strength of interconnections (synaptic weights) between neurons that is needed for memory and self-programming (self-organization and learning). The answers to these questions seem to be coming from two directions of research. One is connection machines in which a large number of digital central processing units are interconnected to perform parallel computations in VLSI hardware; the other is analog hardware where a large number of simple processing units (neurons) are connected through modifiable weights such that their phase-space dynamic behavior has useful signal processing functions associated with it.

Analog optoelectronic hardware implementation of neural nets (see Farhat et al. in list of further reading), since first introduced in 1985, has been the focus of attention for several reasons. Primary among these is that the optoelectronic or photonic approach combines the best of two worlds: the massive interconnectivity and parallelism of optics and the flexibility, high gain, and decision making capability (nonlinearity) offered by electronics. Ultimately, it seems more attractive to form analog neural hardware by completely optical means where switching of signals from optical to electronic carriers and vice versa is avoided. However, in the absence of suitable fully optical decision making devices (e.g., sensitive optical bistability devices), the capabilities

of the optoelectronic approach remain quite attractive and could in fact remain competitive with other approaches when one considers the flexibility of architectures possible with it.[*] In this paper we concentrate therefore on the optoelectronic approach and give selected examples of possible architectures, methodologies and capabilities aimed at providing an appreciation of its potential in building a new generation of programmable analog computers suitable for the study of non-linear dynamical systems and the implementation of mappings, associative memory, learning, and optimization functions at potentially very high speed.

We begin with a brief neural net primer that emphasizes phase-space description, then focus attention on the role of optoelectronics in achieving massive interconnectivity and plasticity. Architectures, methodologies, and suitable technologies for realizing optoelectronic neural nets based on optical crossbar (matrix vector multiplier) configurations for associative memory function are then discussed. Next, partitioning an optoelectronic analog of a neural net into distinct layers with a prescribed interconnectivity pattern as a prerequisite for self-organization and learning is discussed. Here the emphasis will be on stochastic learning by simulated annealing in a Boltzmann machine. Stochastic learning is of interest because of its relevance to the role of noise in biological neural nets and because it provides an example of a task that demonstrates the versatility of optics. We close by describing several approaches to realizing the large-scale networks that would be required in analog solution of practical problems.

Neural Nets – A Brief Overview

In this section, a brief qualitative description of neural net properties is given. The emphasis is on energy landscape and phase-space representations and behavior. The descriptive approach adopted is judged best as background for appreciating the material in subsequent sections without having to get involved in elaborate mathematical exposition. All neural net properties described here are well known and can easily be found in the literature. The viewpoint of relating all neural net properties to energy landscape and phase-space behavior is also important and useful in their classification.

A neural net of N neurons has (N^2-N) interconnections or $(N^2-N)/2$ symmetric interconnections, assuming that a neuron does not communicate with itself. The state of a neuron in the net, i.e., its firing rate, can be taken to be binary (0, 1) (on-off, firing or not firing) or smoothly varying according to a nonlinear continuous monotonic function often taken as a sigmoidal function bounded from above

and below. Thus the state of the i-th neuron in the net can be described mathematically by

$$s_i = f\{u_i\} \qquad i = 1, 2, 3 \ldots N \qquad (1)$$

where $f\{.\}$ is a sigmoidal function and

$$u_i = \sum_j^N W_{ij}s_j - \theta_i + I_i \qquad (2)$$

is the activation potential of the i-th neuron, W_{ij} is the strength or weight of the synaptic interconnection between the j-th neuron and the i-th neuron, and $W_{ii} = 0$(i.e., neurons do not talk to themselves). θ_i and I_i are, respectively, the threshold level and external or control input to the i-th neuron, thus $W_{ij}S_j$ represents the input to neuron i from neuron j and the first term on the right side of (2) represents the sum of all such inputs to the i-th neuron. For excitatory interconnections or synapses, W_{ij} is positive, and it is negative for inhibitory ones. For a binary neural net, that is, one in which the nurons are binary, i.e., $s_i[0,1]$, the smoothly varying function $f\{.\}$ is replaced by $U\{.\}$, where U is the unit step function. When W_{ij} is symmetric, i.e., $W_{ij} = W_{ji}$, one can define (see J. J. Hopfield's article in list of further reading) a Hamiltonian or energy function E for the net by

$$E = -\frac{1}{2}\sum_i u_i s_i$$

$$= -\frac{1}{2}\sum_i \sum_j W_{ij}s_i s_j - \frac{1}{2}\sum_i (\theta_i - I_i)s_i \qquad (3)$$

The energy is thus determined by the connectivity matrix W_{ij}, the threshold level θ_i and the external input I_i. For symmetric W_{ij} the net is stable; that is, for any threshold level θ_i and given "strobed" (momentarily applied) input I_i, the energy of the net will be a decreasing function of the neurons state s_i of the net or a constant. This means that the net always heads to a steady state of local or global energy minimum. The descent to an energy minimum takes place by the iterative discrete dynamical process described by Eqs. (1) and (2) regardless of whether the state update of the neurons is synchronous or asynchronous. The minimum can be local or global, as the "energy landscape" of a net (a visualization of E for every state s_i) is not monotonic but will possess many uneven hills and troughs and is therefore characterized by many local minima of various depths and one global (deepest) minimum. The energy landscape can therefore be modified in accordance with Eq. (3) by changing the interconnection weights W_{ij}, and or the threshold levels θ_i, and/or the external input I_i. This ability to "sculpt" the energy landscape of the net provides for almost all the rich and fascinating behavior of neural nets and for the ongoing efforts of harnessing these properties to perform sophisticated spatio-temporal mappings, computations, and control functions. Recipes exist that show how to compute the W_{ij} matrix to make the local energy minima correspond to specific desired states of the network. As the energy minima are stable states, the net tends to settle in one of them, depending on the initializing state, when strobed by a given input. For example, a binary net of $N = 3$ neurons will have a total of $2^N = 8$ states. These are listed in Table 1. They represent all possible combinations s_1, s_2 and s_3 of the three neurons that describe the state vector $s = [s_1,s_2,s_3]$ of the net. For a net of N neurons the state vector is N-dimensional. For $N = 3$ the state vector can be represented as a point (tip of a position vector) in 3-D

---

[*]It is worth mentioning here that recent results obtained in our work show that networks of logistic neurons, whose response resembles that of the derivative of a sigmoidal function, exhibit rich and interesting dynamics, including spurious state-tree associative recall, and allow the use of unipolar synaptic weights. The networks can be realized in a large number of neurons when implemented with optically addressed reflector-type liquid crystal spatial light modulators. However, the flexibility of such an approach versus that of the photonic approach is yet to be determined.

[**]From here on it will be taken as understood that whenever the subscripts (i or j) appear, they run from 1 up to N where N is the number of neurons in the net.
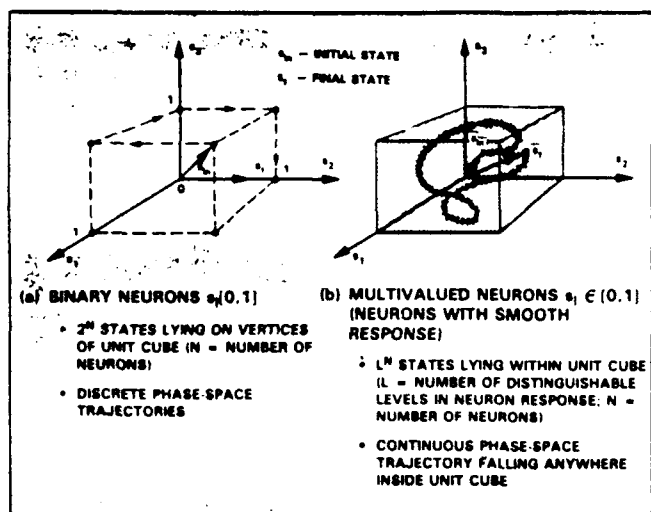
Fig. 1 Phase-space or state space representation and trajectories for a neural net of $N = 3$ neurons. (a) for binary neurons, (b) for neurons with normalized smooth (sigmoidal) response.

space. The eight state vectors listed in Table I fall then on the vertices of a unit cube as illustrated in Fig. 1(a). As the net changes its state, the tip of the state vector jumps from vertex to vertex describing a discrete trajectory as depicted by the broken trajectory starting from the tip of the initializing state vector s_i and ending at the tip of the final state vector s_f. For any symmetric connectivity matrix assumed for the three-neuron net example, each of the eight states in Table I yields a value of the energy E. A listing of these values for each state represents the energy landscape of the net.

For a nonbinary neural net whose neurons have normalized sigmoidal response $s_i \epsilon[0,1]$, i.e., s_i varies smoothly between zero and one, the phase-space trajectory is continuous and is always contained within the unit cube as illustrated in Fig. 1(b). The neural net is governed then by a set of continuous differential equations rather than the discrete update relations of Eqs. (1) and (2). Thus one can talk of nets with either discrete or continuous dynamics. The above phase-space representation is extendable to a neural net of N neurons where one considers discrete trajectories between the vertices of a unit hypercube in N-dimensional space or a smooth trajectory confined within the unit hypercube for discrete and continuous neural nets, respectively.

The stable states of the net, described before as minima of the energy landscape, correspond to points in the phase-space towards which the state of the net tends to evolve in

Table I.   Possible States of a Binary Neural Net of 3 Neurons

S_1	S_2	S_3
0	0	0
0	0	1
0	1	0
1	0	0
0	0	1
1	0	1
1	1	0
1	1	1

time when the net is iterated from an arbitrary initial state. Such stable points are called "attractors" or "limit points" of the net, to borrow from terms used in the description of nonlinear dynamical systems. Attractors in phase-space are characterized by basins of attraction of given size and shape. Initializing the net from a state falling within the basin of attraction of a given attractor and thus regarded as an incomplete or noisy version of the attractor, leads to a trajectory that converges to that attractor. This is a many to one mapping or an associative search operation that leads to an associative memory attribute of neural nets.

Local minima in an energy landscape or attractors in phase-space can be fixed by forming W in accordance with the Hebbian learning rule (see both Hebb and Hopfield in list of further reading), i.e., by taking the sum of the outer products of the bipolar versions of the state vector we wish to store in the net

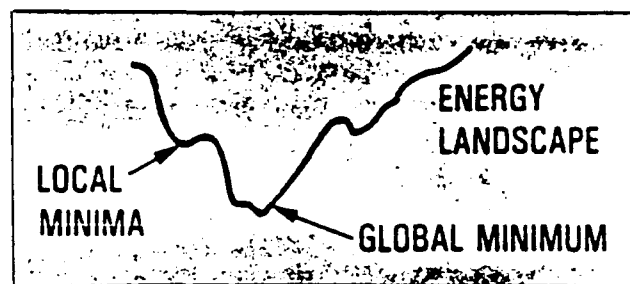$$W_{ij} = \sum_{m=1}^{M} v_i^{(m)} v_j^{(m)} \qquad (4)$$

where

Fig. 2   Conceptual representation of energy landscape.

$$v_i^{(m)} = 2s_i^{(m)} - 1 \qquad i = 1,2\ldots N \qquad m = 1,2\ldots M \qquad (5)$$

are M bipolar binary N-vectors we wish to store in the net. Provided that $s_i^{(m)}$ are uncorrelated and

$$M \le \frac{N}{4\ell nN} \qquad (6)$$

the M stored state $s^{(m)}$ will become attractors in phase-space of the net or equivalently their associated energies will be local minima in the energy landscape of the net as illustrated conceptually in Fig. 2. As M increases beyond the value given by (6), the memory is overloaded, spurious local minima are created in addition to the desired ones and the probability of correct recall from partial or noisy information deteriorates, compromising operation of the net as an associative memory (see R.J. McEliece et al. in list of further reading).

The net can also be formed in such a way as to lead to a hetero-associative storage and recall function by setting the interconnection weights in accordance with

$$V_{ij} = \sum_m v_i^{(m)} g_j^{(m)} \qquad (7)$$

where $\bar{v}^{(m)}$ and $\bar{g}^{(m)}$ are associated N-vectors. Networks of this variety can be used as feedforward networks only and this precludes the rich dynamics encountered in feedback or recurrent networks from being observed. Nevertheless, they are useful for simple mapping and representation.

Energy landscape considerations are useful in devising formulas for the storage of sequences of associations or a cyclic sequence of associations as would be required for conducting sequential or cyclic searches of memories.

Learning in biological neural nets is thought to occur by self-organization where the synaptic weights are modified electrochemically as a result of environmental (sensory and other (e.g., contextual)) inputs. All such learning requires plasticity, the process of gradual synaptic modification. Adaptive learning algorithms can be deterministic or stochastic: supervised or unsupervised. An optoelectronic (Boltzmann machine) and its learning performance will be described in the section on large scale networks as an illustration of the unique capabilities of optoelectronic hardware.

Neural Nets Classification and Useful Functions

The energy function and energy landscape description of the behavior of neural networks presented in the preceding sections allows their classification into three groups. For one group the local minima in the energy landscape are what counts in the network's operation. In the second group the local minima are not utilized and only the global minimum is meaningful. In the third group the operations involved do not require energy considerations. They are merely used for mapping and reduction of dimensionality. The first group includes Hopfield-type nets for all types of associative memory applications that include auto-associative, hetero-associative, sequential and cyclic data storage and recall. This category also includes all self-organizing and learning networks regardless of whether the learning in them is supervised, unsupervised, deterministic, or stochastic as the ultimate result of the fact that learning, whether hard or soft, can be interpreted as shaping the energy landscape of the net so as to "dig" in it valleys corresponding to learned states of the network. All nets in this category are capable of generalization. An input that was not learned specifically but is within a prescribed Hamming distance* to one of the entities learned would elicit, in the absence of any contradictory information, an output that is close to the outputs evoked when the learned entity is applied to the net. Because of the multilayered and partially interconnected nature of self-organizing networks, one can define input and output groups of neurons that can be of unequal number (See section on large scale networks). This is in contrast to Hopfield-type nets which are fully interconnected and therefore the number of input and output neurons is the same (the same neurons define the initial and final states of the net). The ability to define input and output groups of neurons in multilayered nets enables additional capabilities that include learning, coding, mapping, and reduction of dimensionality.

The second group of neural nets includes nets that perform calculations that require finding the global energy minimum of the net. The need for this type of calculation

---

*The Hamming distance between two binary N-vectors is the number of elements in which they differ.

**A chaotic attractor is manifested by a phase-space trajectory that is completely unpredictable and is highly sensitive to initial conditions. It could ultimately turn out to play a role in cognition.
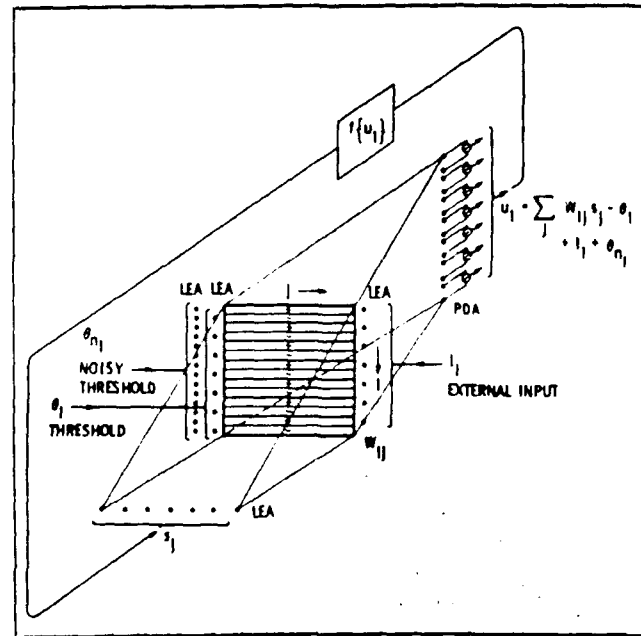
Fig. 3 Optoelectronic analog circuit of a fully interconnected neural net.

often occurs in combinatorial optimization problems and in the solution of inverse problems encountered, for example, in vision, remote sensing, and control.

The third group of neural nets is multilayered with localized nonglobal connections similar to those in cellular automata where each neuron communicates within its layer with a pattern of neurons in its neighborhood and with a pattern of neurons in the next adjacent layer. Multilayered nets with such localized connections can be used for mapping and feature extraction. Neural nets can also be categorized by whether they are single layered or multilayered, self-organizing or nonself-organizing, solely feedforward or involve feedback, stochastic or deterministic. However, the most general categorization appears to be in terms of the way the energy landscape is utilized, or in terms of the kind of attractors formed and utilized in its phase-space (limit points, limit cycles, or chaotic**).

Implementations

The earliest optoelectronic neurocomputer was of the fully interconnected variety where all neurons could talk to each other. It made use of incoherent light to avoid interference effects and speckle noise and also relax the stringent alignment required in coherent light systems. An optical crossbar interconnect (see Fig. 3) was employed to carry out the vector matrix multiplication operation required in the summation term in Eq. 2. (see Farhat et al. (1985) in list of further reading). In this arrangement the state vector of the net is represented by the linear light emitting array (LEA) or equivalently by a linear array of light modulating elements of a spatial light modulator (SLM), the connectivity matrix W_{ij} is implemented in a photographic transparency mask (or a 2-D SLM when a modifiable connectivity mask is needed for adaptive learning), and the activation potential u_i is measured with a photodiode array (PDA). Light from the LEA is smeared vertically onto the W_{ij} mask with
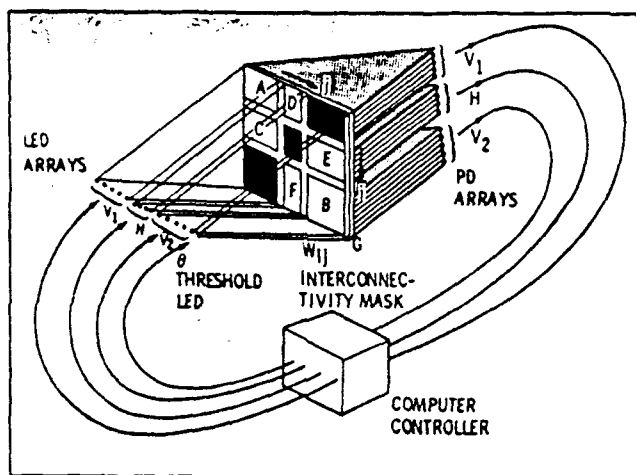
(a)
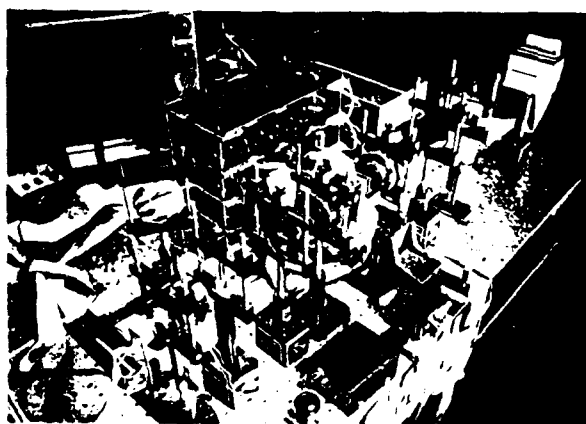
(b)

Fig. 4 Boltzmann learning machine. (a) optoelectronic circuit diagram of a net partitioned into three layers by blocking segments of the interconnectivity mask. (b) hardware implementation showing the state vector LED array at the top right, the MOSLM at the center (between lenses) and an intensified PDA (PDA abutted to an image intensifier fiber output window for added gain) in the lower left. The integrated circuit board rack contains the MOSLM driver and computer interface and the TV receiver in the background provides the "snow pattern" that is imaged through a slit onto the intensifier input window for optical injection of noise in the network.

the aid of an anamorphic lens system (cylindrical and spherical lenses in tandem not shown in the figure for simplicity). Light passing through rows of W_{ij} is focused onto the PDA elements by another anamorphic lens system. To realize bipolar transmission values in incoherent light, positive elements and negative elements of any row of W_{ij} are assigned to two separate subrows of the mask and light passing through each subrow is focused onto adjacent pairs of photosites of the PDA whose outputs are subtracted. In Fig. 3, both the neuron threshold θ, and external input I_i are injected optically with the aid of a pair of LEAs whose light is focused on the PDA. Note that positive valued I_i is assumed here and therefore its LEA elements are shown positioned to focus onto positive photosites of the PDA only.

This architecture was successfully employed in the first implementation of a 32 neuron net (see Farhat et al. (1985)

in list of further reading). Fig. 3 also shows a third LEA for injection of spatio-temporal noise into the net as would be required, for example, in the implementation of a noisy threshold scheme for the Boltzmann learning machine to be discussed later. The net of Fig. 3 behaved as an associative memory very much as expected and was found to exhibit correct recovery of three neurons stored from partial information and showed robustness with element failure (two of its 32 neurons were accidentally disabled, 2 PDA elements broke, and no noticeable degradation in performance was observed).

In the arrangement of Fig. 3, the neurons are fully interconnected. To implement learning in a neural net, one needs to impart structure to the net, i.e., be able to partition the net into distinct input, output, and hidden groups or layers of neurons with a prescribed pattern of communication or interconnections between them which is not possible in a fully interconnected or single layer network. A simple but effective way of partitioning a fully interconnected optoelectronic net into several layers to form a partially interconnected net is shown in Fig. 4(a). This is done simply by blocking certain portions of the W_{ij} matrix.

In the example shown, the blocked submatrices serve to prevent neurons from the input group V_1 and the output group V_2 from talking to each other directly. They can do so only via the hidden or buffer group of neurons H. Furthermore, neurons within H can not talk to each other. This partition scheme enables arbitrary division of neurons among layers and can be rapidly set when a programmable nonvolatile SLM under computer control is used to implement the connectivity weights. Neurons in the input and output groups are called visible neurons because they interface with the environment.

The architecture of Fig. 4 can be used in supervised learning where, beginning from an arbitrary W_{ij}, the net is presented with an input vector from the training set of vectors it is required to learn through V_1 and its convergent output state is observed on V_2 and compared with the desired output (association) to produce an error signal which is used in turn according to a prescribed formula to update the weights matrix. This process of error-driven adaptive weights modification is repeated a sufficient number of times for each vector and all vectors of the training set until inputs evoke the correct desired output or association at the output. At that time the net can be declared as having captured the underlying structure of the environment (the vectors presented to it) by forming an internal representation of the rules governing the mappings of inputs into the required output associations.

Many error-driven learning algorithms have been proposed and studied. The most widely used, the error back-projection algorithm (see Werbos, Parker, and Rumelhart et al. in list of further reading), is suited for use in feed forward multilayered nets that are void of feedback between the neurons. The architecture of Fig. 4(a) has been successfully employed in the initial demonstration of supervised stochastic learning by simulated annealing. Our interest in stochastic learning stemmed from a desire to better understand the possible role of noise in BNNs and to find means for accelerating the simulated annealing process through the use of optics and optoelectronic hardware. For any input-output association clamped on V_1 and V_2 and beginning from an arbitrary W_{ij} that could be random, the net is annealed through the hidden neurons by subjecting them to optically injected noise in the form of a

noise component added to the threshold values of the neurons as depicted by θ_n in Fig. 3.

The source of controlled noise used in this implementation was realized by imaging a slice of the familiar "snow pattern" displayed on an empty channel of a television receiver, whose brightness could be varied under computer control, onto the PD array of Fig. 4(a). This produces controlled perturbation or "shaking" of the energy landscape of the net which prevents its getting trapped into a state of local energy minimum during iteration and guarantees its reaching and staying in the state of the global energy minimum or one close to it. This requires that the injected noise intensity be reduced gradually, reaching zero when the state of global energy minimum is reached to ensure that the net will stay in that state. Gradual reduction of noise intensity during this process is equivalent to reducing the "temperature" of the net and is analogous to the annealing of a crystal melt to arrive at a good crystalline structure. It has accordingly been called simulated annealing by early workers in the field.

Finding the global minimum of a "cost" or energy function is a basic operation encountered in the solution of optimization problems and is found not only in stochastic learning. Mapping optimization problems into stochastic nets of this type, combined with fast annealing to find the state of global "cost function" minimum, could be a powerful tool for their solution. The net behaves then as a stochastic dynamical analog computer. In the case considered here, however, optimization through simulated annealing is utilized to obtain and list the convergent states at the end of annealing bursts when the training set of vectors (the desired associations) are clamped to V_1 and V_2. This yields a table or listing of convergent state vectors from which a probability P_{ij} of finding the i-th neuron and the j-th neuron on at the same time is computed. This completes the first phase of learning. The second phase of learning involves clamping the V_1 neurons only and annealing the net through H and V_2, obtaining thereby another list of convergent state vectors at the end of annealing bursts and calculating another probability P'_{ij} of finding the i-th and j-th neurons on at the same time. The connectivity matrix, implemented in a programmable magneto-optic SLM (MOSLM), is modified then by $\Delta W_{ij} = \epsilon(P_{ij} - P'_{ij})$ computed by the computer controller where ϵ is a constant controlling the learning rate. This completes one learning cycle or episode. The above process is repeated again and again until the W_{ij} stabilizes and captures hopefully the underlying structure of the training set. Many learning cycles are required and the learning process can be time-consuming unless the annealing process is sufficiently fast.

We have found that the noisy thresholding scheme leads the net to anneal and find the global energy minimum or one close to it in about 35 time constants of the neurons used. For microsecond neurons this could be 10^4-10^5 times faster than numerical simulation of stochastic learning by simulated annealing which requires random selection of neurons one at a time, switching their states, and accepting the change of state in such a way that changes leading to an energy decrease are accepted and those leading to energy increases are allowed with a certain controlled probability.

The computer controller in Fig. 4 performs several functions. It clamps the input/output neurons to the desired states during the two phases of learning, controls the annealing profile during annealing bursts, monitors the con-

vergent state vectors of the net, and computes and executes the weights modification. For reasons related to the thermodynamical and statistical mechanical interpretation of its operation, the architecture in Fig. 4(a) is called a Boltzmann learning machine. A pictorial view of an optoelectronic (photonic) hardware implementation of a fully operational Boltzmann learning machine is shown in Fig. 4(b). This machine was built around a MOSLM as the adaptive weights mask.

The interconnection matrix update during learning requires small analog modifications ΔW_{ij} in W_{ij}. Pixel transmittance in the MOSLM is binary, however. Therefore a scheme for learning with binary weights was developed and used in which W_{ij} is made 1 if $(P_{ij} - P'_{ij}) > M$ regardless of its preceeding value, where M is a constant, and made -1 if $(P_{ij} - P'_{ij}) < -M$ regardless of its preceeding value, and is left unchanged if $-M \geq (P_{ij} - P'_{ij}) \leq M$. This introduces inertia to weights modification and was found to allow a net of $N = 24$ neuron partitioned into 8-8-8 groups to learn two autoassociations with 95 percent score (probability of correct recall) when the value of M was chosen randomly between (0-.5) for each learning cycle. This score dropped to 70 percent in learning three autoassociations. However, increasing the number of hidden neurons from 8 to 16 was found to yield perfect learning (100 percent score).

Scores were collected after 100 learning cycles by computing probabilities of correct recall of the training set. Fast annealing by the noisy thresholding scheme was found to scale well with size of the net, establishing the viability of constructing larger optoelectronic learning machines. In the following section two schemes for realizing large-scale nets are briefly described. One obvious approach discussed is the clustering of neural modules or chips. This approach requires that neurons in different modules be able to communicate with each other in parallel, if fast simulated annealing by noisy thresholding is to be carried out. This requirement appears to limit the number of neurons per module to the number of interconnects that can be made from it to other modules. This is a thorny issue in VLSI implementation of cascadeable neural chips (see Alspector and Allen in list of further reading). It provides a strong argument in favor of optoelectronic neural modules that have no such limitation because communication between modules is carried out by optical means and not by wire.

Large Scale Networks

To date most optoelectronic implementations of neural networks have been prototype units limited to few tens or hundreds of neurons. Use of neurocomputers in practical applications involving fast learning or solution of optimization problems requires larger nets. An important issue, therefore, is how to construct larger nets with the programmability and flexibility exhibited by the Boltzmann learning machine prototype described. In this section we present two possible approaches to forming large-scale nets as examples demonstrating the viability of the photonic approach. One is based on the concept of a clusterable integrated optoelectronic neural chip or module that can be optically interconnected to form a larger net, and the second is an architecture in which 2-D arrangement of neurons is utilized, instead of the 1-D arrangement described
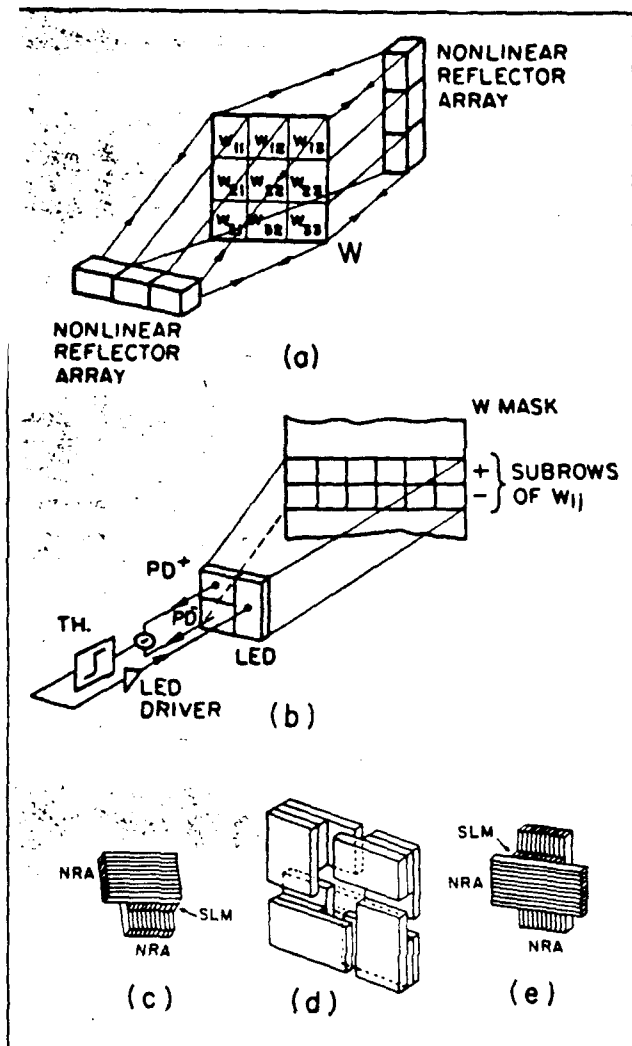
Fig. 5 Optoelectronic neural net employing internal feedback and two orthogonal nonlinear reflector arrays (NRAs) consisting of channels of nonlinear light amplifiers (photodetectors, thresholding amplifiers, LEDs and LED drivers). a) architecture, (b) detail of mask and single element of nonlinear reflector array, (c) and (d) optoelectronic neural chip concept and cluster of four chips, (e) neural chip for forming clusters of more than four chips.

in earlier sections, in order to increase packing density and to provide compatibility with 2-D sensory data formats.

Clusterable Photonic Neural Chips

The concept of a clusterable photonic neural chip, which is being patented by the University of Pennsylvania, is arrived at by noting that when the connectivity matrix is symmetrical, the architectures we described earlier (see Figs. 3 or 4(a)) can be modified to include internal optical feedback and nonlinear "reflection" (optoelectronic detection, amplification, thresholding and light emission or modulation) on both sides of the connectivity mask W or nonvolatile SLM (e.g., a MOSLM) as depicted in Fig. 5 (see Farhat (1987) in list of further reading). The nonlinear reflector arrays are basically retro-reflecting optoelectronic or photonic light amplifier arrays that receive and retransmit light on the same side facing the MOSLM.

Two further modifications are needed to arrive at the

concept of clusterable integrated optoelectronics or photonic neural chips. One is replacement of the LEDs of the nonlinear reflector arrays by suitable spatial light modulators of the fast ferroelectric liquid crystal variety for example, and extending the elements of the nonlinear reflector arrays to form stripes that extend beyond the dimensions of the connectivity SLM, and sandwiching the latter between two such striped nonlinear reflector arrays oriented orthogonally to each other as depicted in Fig. 5(c). This produces a photonic neural chip that operates in an ambient light environment. Analog integrated circuit (IC) technology would then be used to fabricate channels of nonlinear (thresholding) amplifiers and SLM drivers, one channel for each PD element. The minute IC chip thus fabricated is mounted as an integral part on each PDA SLM assembly of the nonlinear reflector arrays. Individual channels of the IC chip are bonded to the PDA and SLM elements. Two such analog IC chips are needed per neural chip. The size of the neural chip is determined by the number of pixels in the SLM used.

An example of four such neural chips connected optoelectronically to form a larger net by clustering is shown in Fig. 5(d). This is achieved by simply aligning the ends of the stripe PD elements in one chip with the ends of the stripe SLM elements in the other. It is clear that the hybrid photonic approach to forming the neural chip would ultimately and preferably be replaced by an entirely integrated photonic approach and that neural chips with the slightly different form shown in Fig. 5(e) can be utilized to form clusters of more than four. Large-scale neural nets produced by clustering integrated photonic neural chips have the advantage of enabling any partitioning arrangement, allowing neurons in the partitioned net to communicate with each other in the desired fashion enabling fast annealing by noisy thresholding to be carried out, and of being able to accept both optically injected signals (through the PDAs) or electronically injected signals (through the SLMs) in the nonlinear reflector arrays, facilitating communication with the environment. Such nets are therefore capable of both deterministic or stochastic learning. Computer controlled electronic partitioning and loading and updating of the connectivity weights in the connectivity SLM (which can be of the magneto-optic variety or the nonvolatile ferroelectric liquid crystal (FeLCSLM) variety) is assumed. This approach to realizing large-scale fully programmable neural nets is currently being developed in our laboratory, and illustrates the potential role integrated photonics could play in the design and construction of a new generation of analog computers intended for use in neurocomputing and rapid simulation and study of nonlinear dynamical systems.

Neural Nets with Two-Dimensional Deployment of Neurons

Neural net architectures in which neurons are arranged in a two-dimensional (2-D) format to increase packing density and to facilitate handling 2-D formatted data have received early attention (see Farhat and Psaltis (1987) in list of further reading). These arrangements involve a 2-D N × N state "vector" or matrix s_{ij} representing the state of neurons, and a four-dimensional (4-D) connectivity "matrix" or tensor T_{ijkl} representing the weights of synapses between neurons. A scheme for partitioning the 4-D connectivity tensor into an N × N array of submatrices, each

NONLINER FEEDBACK

AMP

THRESH.

PD ARRAY

SYNAPTIC MASK
(T$_{ij kl}$ MATRIX
OVERLAYS PD ARRAY)

LED ARRAY.
FEATURE
COMPOSOR

LENSLET
ARRAY

(a)

NONLINER FEEDBACK

AMP

THRESH.

CCD
CAMERA

INPUT –
LEARNING AND
INITIALIZATION

DISPLAY
MONITOR

LENSLET
ARRAY

SYNAPTIC MASK
(PARTITIONED
T$_{ij kl}$ MATRIX)
BACKED BY ARRAY
OF LIGHT INTEGRATING
ELEMENTS.

(b)

OPTICAL
FEEDBACK

LENSLET
ARRAY

PROJECTION
LENS

ANALYZER

BEAM
SPLITTER

MSLM

POLARIZED
LASER BEAM

TRANSMISSION
PROJECTION
SCREEN

SYNAPTIC MASK
(PARTITIONED T$_{ij kl}$ MATRIX)
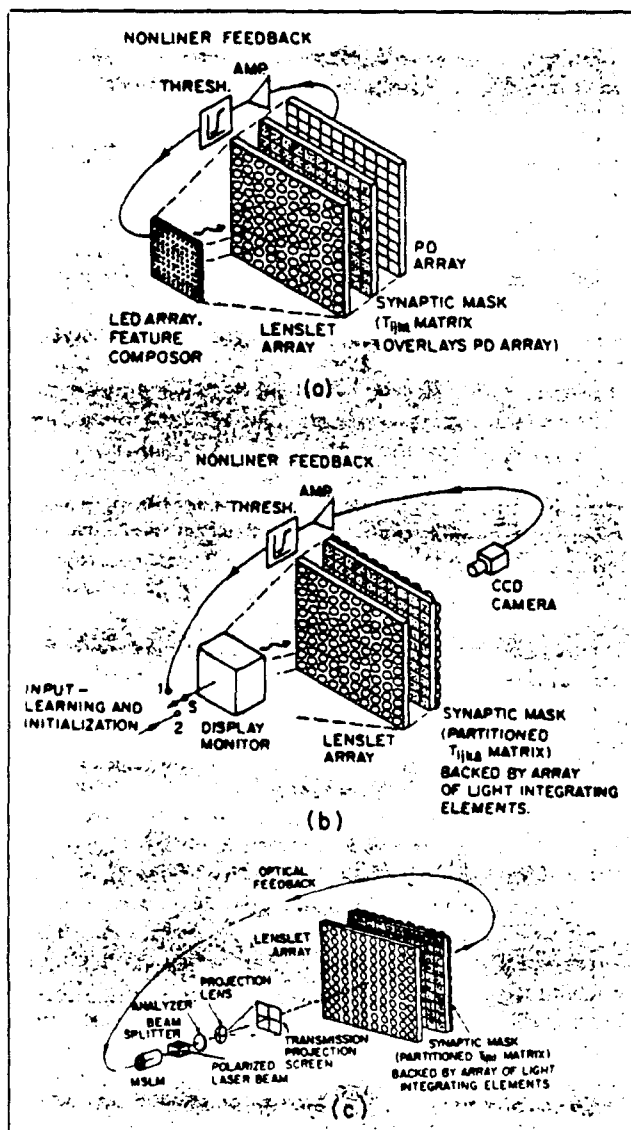BACKED BY ARRAY OF LIGHT
INTEGRATING ELEMENTS

(c)

Fig. 6 Three optoelectronic network architectures in which the neurons are arranged in two-dimensional format employing (a) parallel nonlinear electronic amplification and feedback, (b) serial nonlinear electronic amplification and feedback, (c) parallel nonlinear electron optical amplification and feedback.

of which has $N \times N$ elements, to enable storing it in a flat 2-D photomask or SLM for use in optoelectronic implementation has been developed (see Farhat and Psaltis 1987 in list of further reading). Several arrangements are possible using this partitioning scheme (see Fig. 6).

In Fig. 6(a), neuron states are represented with a 2-D LED array (or equivalently with a 2-D SLM). A two-dimensional lenslet array is used to spatially multiplex and project the state vector display onto each of the submatrices of the partitioned connectivity mask. The product of the state matrix with each of the weights stored in each submatrix is formed with the help of a spatially integrating square photodetector of suitable size positioned behind each submatrix. The (i-j)th photodetector output represents the activation potentials u_{ij} of the (i-j)th neurons. These activation potentials are nonlinearly amplified and fed back in parallel to drive the corresponding elements of the LED state array of those of the state SLM. In this fashion, weighted interconnections between all neurons are established by means of

the lenslet array instead of the optical crossbar arrangement used to establish connectivity between neurons when they are deployed on a line.

Both plastic molded and glass micro-lenslet arrays can be fabricated today in 2-D formats. Glass micro-lenslet arrays with density of 9 to 25 lenslets/mm² can be made in large areas using basically photolithographic techniques. Resolution of up to ~50 ℓp/mm can also be achieved. Therefore, a micro lenslet array of (100×100)mm², for example, containing easily 10^5 lenslets could be used to form a net of 10^5 neurons provided that the required nonlinear light amplifiers (photodetector/thresholding amplifier LED or SLM driver array) become available. This is another instance where integrated optoelectronics technology can play a central role. We have built a 8×8 neuron version of the arrangement in Fig. 6(a) employing a square LED array, a square plastic lenslet array, and a square PDA, each of which has 8×8 elements in which the state update was computed serially by a computer which sampled the activation potentials provided by the PDA and furnished the drive signals to the LED array. The connectivity weights in this arrangement were stored in a photographic mask which was formed with the help of the system itself in the following manner: Starting from a set of unipolar binary matrices b_{ij} to be stored in the net, the required 4-D connectivity tensor was obtained by computing the sum of the outer products of the bipolar binary versions $v_{ij} = 2b_{ij} - 1$. The resulting connectivity tensor was partitioned and unipolar binary quantized versions of its submatrices were displayed in order by the computer on the LED display and stored at their appropriate locations in a photographic plate placed in the image plane of the lenslet array by blocking all elements of the lenslet array except the one where a particular submatrix was to be stored. This process was automated with the aid of a computer controlled positioner scanning a pinhole mask in front of the lenslet array so that the photographic plate is exposed to each submatrix of the connectivity tensor displayed sequentially by the computer. The photographic plate was then developed and positioned back in place. Although time-consuming, this method of loading the connectivity matrix in the net has the advantage of compensating for all distortions and aberrations of the system.

The procedure for loading the memory in the system can be speeded up considerably by using an array of minute electronically controlled optical shutters (switches) to replace the function of the mechanically scanned pinhole. The shutter array is placed just in front or behind the lenslet array such that each element of the lenslet array has a corresponding shutter element in register with it. An electronically addressed ferroelectric liquid crystal spatial light modulator (FeLCSLM) (see Spatial Light Modulators and Applications in list of further reading) is a suitable candidate for this task because of its fast switching speed (a few microseconds). Development of FeLCSLMs is being pursued worldwide because of their speed, high contrast, and bistability which enables nonvolatile switching of pixel transmission between two states. These features make FeLCSLMs also attractive for use as programmable connectivity masks in learning networks such as the Boltzmann machine in place of the MOSLM presently in use.

Because the connectivity matrix was unipolar, an adaptive threshold equal to the mean or energy of the iterated state vector was found to be required in computing the update state to make the network function as an associative

memory that performed in accordance with theoretical predictions of storage capacity and for successful associative search when sketchy (noisy and/or partial) inputs are presented. Recent evidence in our work is showing that ligistic neurons, mentioned in a footnote earlier, allow using unipolar connectivity weights in a network without having to resort to adaptive thresholding. This behavior may be caused by the possibility that logistic neurons, with their "humped" nonsigmoidal response, combine at once features of excitatory and inhibitory neurons which, from all presently available evidence, is biologically not plausible. Biological plausibility, it can be argued, is desirable for guiding hardware implementations of neural nets but is not absolutely necessary as long as departures from it facilitate and simplify implementations without sacrificing function and flexibility.

Several variations of the above basic 2-D architecture were studied. One, shown in Fig. 6(b) employs an array of light integrating elements (lenslet array plus diffusers, for example) and a CCD camera plus serial nonlinear amplification and driving to display the updated state matrix on a display monitor. In Fig. 6(c) a microchannel spatial light modulator (MCSLM) is employed as an electron-optical array of thresholding amplifiers and to simultaneously display the updated state vector in coherent laser light as input to the system. The spatial coherence of the state vector display in this case also enables replacing the lenslet array with a fine 2-D grating to spatially multiplex the displayed image onto the connectivity photomask. Our studies show that the 2-D architectures described are well suited for implementing large networks with semi-global or local rather than global interconnects between neurons, with each neuron capable of communicating with a few thousand neurons in its vicinity depending on lenslet resolution and geometry. Adaptive learning in these architectures is also possible provided a suitable erasable storage medium is found to replace the photographic mask. For example in yet another conceivable variant of the above architectures, the lenslet array can be used to spatially demultiplex the connectivity submatrices presented in a suitable 2-D erasable display, i.e. project them in perfect register, onto a single SLM device containing the state vector data. This enables forming the activation potential array u directly and facilitates carrying out the required neron response operations (nonlinear gain) optically and in parallel through appropriate choice of the state vector SLM and the architecture. Variations employing internal feedback, as in 1-D neural nets, can also be conceived.

Discussion

Optoelectronics (or photonics) offers clear advantages for the design and construction of a new generation of analog computers (neurocomputers) capable of performing computational tasks collectively and dynamically at very high speed and as such, are suited for use in the solution of complex problems encountered in cognition, optimization, and control that have defied efficient handling with traditional digital computation even when very powerful digital computers are used. The architectures and proof of concept prototypes described are aimed at demonstrating that the optoelectronic approach can combine the best attributes of optics and electronics together with programmable nonvolatile spatial light modulators and displays to form versatile neural nets with important capabilities that include associative storage and recall, self organization and adaptive learning (self-programming), and fast solution of optimization problems. Large-scale versions of these neurocomputers are needed for tackling real world problems. Ultimately these can be realized using integrated optoelectronic (integrated photonic) technology rather than the hybrid optoelectronic approach presented here. Thus, new impetus is added for the development of integrated optoelectronics besides that coming from the needs of high speed optical communication. One can expect variations of integrated optoelectronic repeater chips utilizing GaAs on silicon technology being developed with optical communication in mind (see J. Shibata and T. Kajiwara in list of further reading). These, when fabricated in dense array form, will find widespread use in the construction of large-scale analog neurocomputers. This class of neurocomputers will probably also find use in the study and fast simulation of nonlinear dynamical systems and chaos and its role in a variety of systems.

Biological neural nets were evolved in nature for one ultimate purpose: that of maintaining and enhancing survivability of the organism they reside in. Embedding artificial neural nets in man-made systems, and in particular autonomous systems, can serve to enhance their survivability and therefore reliability. Survivability is also a central issue in a variety of systems with complex behavior encountered in biology, economics, social studies, and military science. One can therefore expect neuromorphic processing and neurocomputers to play an important role in the modeling and study of such complex systems especially if integrated optoelectronic techniques can be made to extend the flexibility and speed demonstrated in the prototype nets described to large scale networks. One should also expect that software development for emulating neural functions on serial and parallel digital machines will not continue to be confined, as at present, to the realm of straightforward simulation, but spurred by the mounting interest in neural processing, will move into the algorithmic domain where fast efficient algoriths are likely to be developed, especially for parallel machines, becoming to neural processing what the FFT (fast Fourier transform) was to the discrete Fourier transform. Thus we expect that advances in neuromorphic analog and digital signal processing will proceed in parallel and that applications would draw on both equally.

Acknowledgement

List of Further Reading

J. Alspector and R. B. Allen, "A Neuromorphic VLSI Learning System," in *Advanced Research in VLSI*, Paul Losleben, Ed., (MIT Press, Cambridge, MA, 1987).

N. Farhat, "Optoelectronic Analogs of Self-Programming Neural Nets..." *Applied Optics*, 26, 5093, 1987.

N. Farhat and D. Psaltis, "Optical Impelmentation of Associative Memory" in *Optical Signal Processing*, J. L. Horner, Ed., Academic Press, 1987, pp. 129–162.

N. Farhat, D. Psaltis, A. Prata and E. G. Paek, "Optical Implementation of the Hopfield Model," *Applied Optics*, 24, 1469, 1985.

N. Farhat and Z. Y. Shae, "An Optical Learning Machine," *Proc. 1989 Hawaii International Conference on System Science*, Vol. 1, IEEE Computer Society Press, IEEE Cat. No. 89TH0242-8,432 (1989).

S. Grossberg, *Studies of Mind and Brain*, Reidel, Boston, 1982.

D. O. Hebb, *The Orga. .ion of Behavior*, J. Wiley, New York. 1949.

G. E. Hinton, and T. J. Sejnowski, "Learning and Relearning in Boltzmann Machines," in *Parallel Distributed Processing*, D. E. Rumelhart and J. L. McClelland (Eds.), Vol. I, Bradford-MIT Press, Cambridge, MA, 1986.

J. J. Hopfield, "Neural Networks and Physical Systems with Emergent Collective Computational Abilities," *Proc. Natl. Acad. Sci. 79*, 2554, 1982; "Neurons with Graded Response Have Collective Computational Properties Like Those of Two-State Neurons," *Proc. Natl. Acad. Sci. 81*, 3088, 1984.

R. J. McEleice, E. C. Posner, E. R. Rodemich and S. S. Venkatesh, "The Capacity of the Hopfield Associative memory," *IEEE Transactions on Information Theory*, Vol. IT-33, 461–482, 1987.

K. Nakano, "Associatron — a Model of Associative Memory," *IEEE Trans. Syst. Man Cybern.* SMC-2, 380, 1972.

D. B. Parker, "Learning Logic," MIT Tech. Report TR-47, 1985.

D. E. Rumelhart, G. E. Hinton, and R. J. Williams, "Learning Internal Representation by Error Propagation," in *Parallel Distributed Processing*, D. E. Rumelhart and J. L. McClelland (Eds.), Vol. I, Bradford-MIT Press, Cambridge, MA, 1986.

J. Shibata and T. Kajiwara, *IEEE Spectrum*, 26, 34, 1989.

"Spatial Light Modulators and Applications," *Optical Society of America Technical Digest Series*, Vol. 8, 1988.

P. Werbos, "Beyond Regression: New Tools for Prediction and Analysis in the Behavioral Sciences," *Harvard University Dissertation*, 1974.

R.J. Marks II is the current chairman pro term of the *IEEE Neural Networks Committee*. He was co-founder and first chairman of the *IEEE Circuits and Systems Technical Committee on Neural Systems and Applications*. He is a Professor of Electrical Engineering at the University of Washington, Seattle. He was asked by the LEOS editor of *Circuits and Devices Magazine* to be the guest editor of this series of three articles on neural networks.

Nabil H. Farhat received the B.Sc. degree in 1957 from the Technion-Israel Institute of Technology, Haifa, the M.Sc. degree in 1959 from the University of Tennessee, Knoxville, and the Ph.D. degree in 1963 from the University of Pennsylvania, Philadelphia – all in Electrical Engineering.

In 1964 he joined the faculty of the Moore School of Electrical Engineering, University of Pennsylvania, where he is now Professor in Electrical Engineering and heads the Electro-Optics and Microwave-Optics Laboratory. His research encompasses image understanding, microwave imaging and holography, optical information processing and modeling of neural network and self-organizing systems for neurodynamical pattern and target identification in all of which he has published extensively. His teaching covers EM theory, electron and light optics, neurodynamics, optics, and optical computing.

While being an Associate Professor, Dr. Farhat held the Ennis Chair in Electrical Engineering. He has held visiting professorships at Universities in the U.S. and abroad. In 1985 he was named Distinguished Visiting Scientist at the Jet Propulsion Laboratory in Pasadena and has served in that capacity since then for several summer periods. He is a recipient of the University of Pennsylvania Christian R. and Mary F. Lindback Foundation award for distinguished teaching, is a Fellow of the Institute of Electrical and Electronics Engineers, and the Optical Society of America, and member of several other professional and honorary societies. He also served on the National Board of Directors of Eta Kappa Nu and was an RCA consultant from 1969 to 1980. Dr. Farhat was Editor of *Advances in Holography* and Associate Editor of *Acoustical Imaging and Holography*. He is presently action editor for two neural network journals: *Neural Networks* and *Neural Computation*.